

Andreev Interferometry of Flux Qubits Driven  
By Radio Frequency Field

Christopher Checkley  
Royal Holloway College  
University of London

Dissertation submitted for the degree of Doctor of Philosophy

March 1, 2010

I declare that the work submitted in this thesis is all my own

Signed

Christopher Checkley

## Abstract

In this thesis we present the continuing work done examining a system in which an Andreev interferometer is used to probe the state of a flux qubit. In particular, we show that the back action of the interferometer on the qubit is low enough that an energy gap can still be observed in the qubit, and present the first experimental evidence of resonant excitation of a flux qubit detected using an Andreev interferometer.

We begin by discussing the theory of flux qubits and Andreev interferometers individually. We then go on to examine what happens when with these two types of structures are combined, with particular attention being paid to the consequences for the coherence time of the qubit.

We then discuss the practical elements of the experiment, notably the development of a tri-layer resist system that can be used to create high quality mesoscopic structures.

We present the experimental results, which show the evidence for resonant excitation of a qubit detected using an Andreev interferometer. The quality of these resonances suggests that the system has a coherence time of less than 1ns.

To conclude we examine some ways in which we believe the system can be improved in order to allow more detailed spectroscopic and time resolved measurements.

## Acknowledgements

I would like to offer my sincere thanks to everyone who helped me complete my PhD.

I would like to thank my supervisor Victor Petrashov for all his advice and support, without which I would never have been able to complete this project.

I would like to thank Dr. James Nicholls, Dr. Rais Shaikhaidarov, Mr. Massimo Venti and Dr. Kevin Marshall for lending me their extensive expertise.

I would also like to thank PhD student Andrea Iagallo for all his hard work on the project.

I would like my parents for all their support.

Finally I would like to thank Jana Crippen for the many hours she has spent correcting my spelling and grammar, and for her constant support in general.



# Contents

<b>1</b>	<b>Introduction</b>	<b>4</b>
1.1	Background . . . . .	6
1.1.1	History . . . . .	6
1.1.2	Implementation . . . . .	7
1.2	Persistent Current Qubits . . . . .	8
1.3	A Unique Qubit Readout . . . . .	10
1.4	Work Completed For This Project . . . . .	10
<b>2</b>	<b>Superconductivity and Josephson Junctions</b>	<b>12</b>
2.1	Introduction . . . . .	12
2.2	Flux quantization . . . . .	13
2.3	Fundamental Josephson Equations . . . . .	14
2.4	The RCSJ Model of a Josephson Junction . . . . .	15
2.5	Josephson Energy and Charging Energy . . . . .	17
2.6	Quantum Behaviour of Josephson Junctions . . . . .	18
<b>3</b>	<b>Flux Qubits - A Mesoscopic Two State System</b>	<b>22</b>
3.1	Flux Qubits . . . . .	22
3.1.1	A Simple Flux Qubit - The RF Squid . . . . .	23
3.1.2	Macroscopic Quantum Effects . . . . .	27
3.1.3	The Three Junction Flux Qubit . . . . .	29
3.2	Describing Qubit Behaviour . . . . .	29
3.2.1	The Bloch Sphere . . . . .	30
3.2.2	Rabi Oscillations . . . . .	31
3.2.3	Detuned Resonances . . . . .	36
3.2.4	Decoherence . . . . .	36
3.3	Summary . . . . .	38
<b>4</b>	<b>The Proximity Effect and Andreev Interferometers</b>	<b>39</b>
4.1	S/N Interface . . . . .	39
4.2	SNS Junctions . . . . .	40

4.3	Tuning the Supercurrent in a SNS Junction . . . . .	43
4.4	Andreev Reflection . . . . .	44
4.5	Summary . . . . .	57
<b>5</b>	<b>Readout Methods for Flux Qubits</b>	<b>58</b>
5.1	Modelling the Behaviour of a Qubit and Interferometer . . . . .	58
5.2	Other Readout Methods . . . . .	63
5.2.1	DC Squid Readout Method . . . . .	63
5.2.2	Tank Circuit Readout Method . . . . .	65
5.2.3	Non-Linear Oscillator Readout Method . . . . .	68
5.2.4	Comparison of Other Readouts to Andreev Interferometer . . . . .	68
<b>6</b>	<b>Decoherence</b>	<b>72</b>
6.1	Dephasing and Relaxation . . . . .	72
6.2	Sources of Circuit Noise in Qubit/Interferometer System . . . . .	74
6.2.1	Relaxation and Dephasing Due to Andreev Interferometer . . . . .	74
6.2.2	Relaxation and Dephasing Due to Microwave Antenna . . . . .	78
6.2.3	Relaxation and Dephasing Due to Solenoid . . . . .	79
6.2.4	Estimates of Relaxation and Dephasing Times for Our System . . . . .	79
6.3	Modelling Spectroscopy . . . . .	81
<b>7</b>	<b>Fabrication</b>	<b>91</b>
7.1	Introduction . . . . .	91
7.2	Fabrication Techniques . . . . .	92
7.3	Layers . . . . .	95
7.3.1	Contact Layer . . . . .	95
7.3.2	Andreev Layer . . . . .	95
7.3.3	Spacer Layer . . . . .	98
7.3.4	Qubit Layer . . . . .	98
<b>8</b>	<b>Measurement Setup</b>	<b>104</b>
8.1	Low Frequency Measurements . . . . .	106
8.2	Microwave Frequencies . . . . .	106
8.3	Magnetic Field . . . . .	112
8.4	Secondary Sample . . . . .	112



<b>9</b>	<b>Results and Discussion</b>	<b>113</b>
9.1	Overview . . . . .	113
9.2	Measurements on Qubit in the Ground State . . . . .	116
9.3	Temperature Measurements . . . . .	116
9.3.1	The Effect of Temperature on Oscillation Amplitude . . . . .	116
9.3.2	Temperature Dependent Changes in the Shape of Resistance Curves Close to the Degeneracy Point . . . . .	118
9.4	Behaviour of System When Driven by a Continuous RF Field . . . . .	124
9.4.1	Dependence on RF Field Amplitude . . . . .	125
9.4.2	Dependence on RF Field Frequency . . . . .	125
9.5	Andreev Interferometer's response to a strong RF field . . . . .	132
9.6	Summary and Conclusions . . . . .	135
9.7	Future Work . . . . .	135
9.7.1	Method 1 . . . . .	136
9.7.2	Method 2 . . . . .	136

# Chapter 1

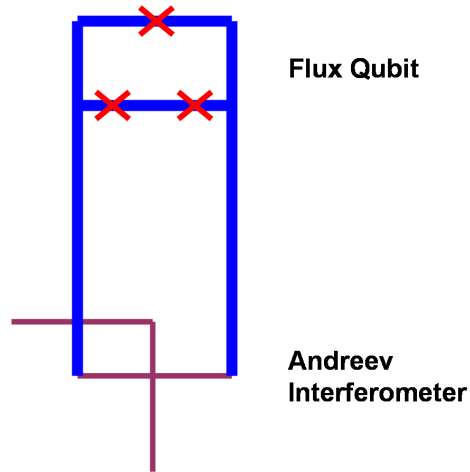
## Introduction

The aim of this project was to probe the state of a mesoscopic quantum system known as a flux qubit using a device called an Andreev interferometer.

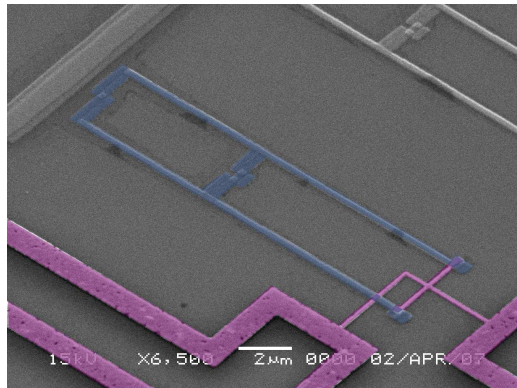
Flux qubits are mesoscopic loops of superconducting material that behave as an artificial two state system. Such a system is of great interest for two reasons, one practical and one more fundamental. The practical reason is that such a system can be used as a qubit, the building block of one of the ‘Holy Grails’ of science, the quantum computer. The more fundamental reason is that a flux qubit is a mesoscopic analogue of an atom. By probing the flux qubit and seeing how it behaves we can gain a better understanding of quantum mechanics and; therefore, the fundamental nature of matter itself.

There are several groups around the world investigating the properties of flux qubits. What makes this project unique is the way in which the state of the qubit is determined, or ‘read out’. Other groups use devices such as SQUIDs or tank circuits to probe the state of the qubit[1][2]. In this project another mesoscopic device, the Andreev interferometer, is used to achieve similar results. While it is believed that this method has several advantages over the other methods mentioned, it also presents its own unique set of problems which must be overcome. Previous work by Dr. Kevin Marshall[3] and Dr. Kok Gnee Chua[4] have demonstrated the viability of this proposal and in this project we present the first evidence for spectroscopy of a flux qubit using Andreev interference.

The structure of this dissertation is as follows: This chapter sets out the main details of the project; gives some historical background; and explains the motivation behind the work, particularly the advantages flux qubits have over other qubit implementations and the novel use of an Andreev interferometer. Chapters 2 to 4 outline the theory describing the behaviour of both flux qubits and Andreev interferometers. In chapter 5 the behaviour of a combined interferometer and qubit system is examined. Chapters 6



(a)



(b)

Figure 1.1: The mesoscopic structure examined in this structure is a combined flux qubit and Andreev interferometer. (a) Shows a diagram of the structure and (b) shows a SEM image of the finished device. The qubit is made from a loop of aluminium (shown in blue) interrupted by Josephson junctions (shown in red). The Andreev interferometer is made of a silver cross (shown in purple). The horizontal part of the cross is connected to two superconducting wires which lead to the qubit.

and 7 are concerned with the practical details of the experiments, particularly the development of a novel tri-layer resist system which has allowed for the creation of high quality mesoscopic structures. Chapter 8 presents and discusses the results of the experiments that have been completed, while Chapter 9 concludes and looks at the future prospects of this project.

## 1.1 Background

A qubit is a quantum bit, the building block of a quantum computer. A quantum computer is a device which makes use of the unusual nature of physics at quantum level in order to carry out calculations. Flux qubits are one of the most promising implementations of such a system, making use of the peculiar nature of superconducting materials in order to create a system that behaves in a quantum way but is also easy to manipulate. Andreev interferometry is a novel readout method for a flux qubit that promises many advantages over other techniques[5].

### 1.1.1 History

The concept of a quantum computer arose out of the difficulty in simulating quantum systems using a classical computer. In 1982, Richard Feynman observed that certain quantum mechanical effects could not be simulated efficiently on a classical computer[6]. He proposed that the only way to produce an effective model of a quantum system was to use another system that itself behaved in a quantum way. This then led to speculation that if a machine that made use of quantum effects could provide a more effective way of producing models of physical systems, perhaps there were other tasks at which it would have an advantage over a classical computer. Unfortunately, building such a quantum computer proved difficult, and although it was suspected there were tasks that such a computer would be especially suited for, no one was able to provide a specific example. This suddenly changed in 1994 when Peter Shor showed that factorizing large numbers was a task quantum computers could do exponentially quicker than classical computers[7]. The extreme difficulty of factorizing large numbers is a keystone on which modern cryptography is built and this revelation led to a renewed flurry of activity in quantum computing, with computer theorists searching for other algorithms that quantum computers could run, and experimental physicists researching systems that could be used to implement a quantum computer.

### 1.1.2 Implementation

Like classical computers a quantum computer is comprised of a large number of bits, in this case called quantum bits or qubits, which act as switches with two states, 0 and 1. Unlike classical computers in which each bit must be in a definite state, each qubit can be in a superposition of both the 0 and 1 states simultaneously. This means that while a classical computer with  $n$  bits can be in only one of  $2^n$  different combinations, a computer of  $n$  qubits can be in  $2^n$  states simultaneously and can carry out operations on them in parallel. Reading out the answer from the computer means observing the state of the qubits and therefore collapsing the superposition. However, algorithms can and have been written which allow for this and still permit the correct answer to be collected from the system. This parallel processing of many different states allows a quantum computer to do some tasks exponentially quicker than a classical computer.

The delay in creating a fully functioning quantum computer has been caused by the difficulty in finding a quantum system that works as an effective qubit. David DiVincenzo devised a list of five criteria a system must meet if it is to be used as a quantum computer[8]-

1. **A scalable physical system with well characterized qubits.**
2. **The ability to initialize the state of the qubits to a simple fiducial state.**
3. **Long relevant decoherence times, much longer than the gate operation time.**
4. **A universal set of quantum gates.**
5. **A qubit-specific measurement capability.**

Candidates for qubits can be broken down into two categories. The first are those based on atomic systems. These include qubits based on nuclear magnetic resonance work[9][10], ion traps[11][12] and cavity QED approaches[13][14]. These systems were initially seen as promising candidates because they have few degrees of freedom and can be easily decoupled from their environment, and so far the most advanced work towards a quantum computer has been done on these types of systems. However, the properties that make it easy to decouple them from their environment also make them difficult to fabricate. It is estimated that to create an operational quantum computer upwards of 10,000 qubits will be needed and it is thought that this is extremely impractical with these types of systems[15].

The second kind of qubits are solid state structures that have been artificially fabricated so that under certain conditions they exhibit quantum properties. These structures are generally micrometer sized and can be constructed on a silicon substrate using lithography techniques well established by the microchip industry. They are made from either superconducting or semiconducting materials. Because they are micrometer sized, and yet still display quantum phenomenon over large length scales, they are referred to as *mesoscopic structures*.

## 1.2 Persistent Current Qubits

In this project we have worked with *superconducting persistent current qubits*, otherwise known as *flux qubits*. They are constructed from loops of superconducting metal interrupted by weak links which are called Josephson junctions. Flux through the loop causes a persistent current to flow. The state of the qubit is defined by the direction of this persistent current. As the applied flux approaches half a flux quanta,  $\Phi_E = \Phi_0/2$ , energy level repulsion occurs[16] and as it changes from  $\Phi_E < \Phi_0$  to  $\Phi_A > \Phi_0$  the persistent current changes direction. This phenomenon then occurs at each half integer multiple of a flux quanta.

At applied flux around  $\Phi_E = 0.5n\Phi_0$ , where  $n$  is an integer, the excited state of the system becomes accessible. Two methods can be used to access this excited state. Applying a pulse of EM radiation with energy equal to the gap energy between the states will cause the system to undergo Rabi oscillations. Controlling the length and duration of this pulse allows the system to be put into a superposition of the two states. A similar effect can be achieved by rapidly changing the magnetic field.

As mentioned above, the major advantage that mesoscopic systems such as flux qubits have over atomic systems is that their fabrication makes them scalable, so creating the large number needed for a quantum should not be a significant problem, and they can be easily connected to the environment, making it easier to address and read out the qubits. These advantages come at a price, however and because flux qubits are more connected to their environment they are also more susceptible to environment noise, which causes decoherence. The major challenge when working with these qubits; therefore, becomes meeting the fourth of DiVincenzo's criteria, achieving coherence times long enough to make qubit operations possible. There are two major sources of noise that need to be considered. The first is thermal noise, which must be lower than the energy gap between the two energy states of the qubit to avoid thermal activation. This was achieved by placing the sample in a

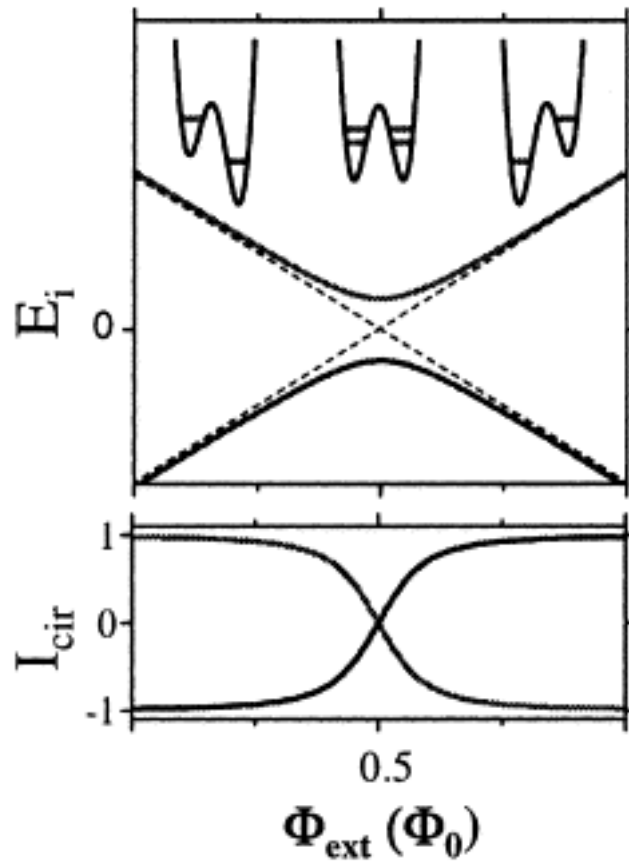


Figure 1.2: The energy levels for the ground state (dark line) and the first excited state of the qubit versus applied flux. The double well potentials are shown schematically above. The lower graph shows the circulating current in the qubit for both states as a function of applied flux. The units of flux are given in terms of the flux quantum. Image taken from[16].

dilution refrigerator and cooling it to temperatures of less than 20mK. The second is electron noise from the measurement equipment attached to the equipment and environment. In this project the aim has been to reduce this through careful design of the measurement system and through the addition of filtering and shielding around the qubit.

### 1.3 A Unique Qubit Readout

Persistent current qubits are being investigated by several other experimental groups around the world, and the qubit used in this project has been designed to be comparable to theirs. However, what makes this work unique is the readout system. While other groups have relied on SQUIDS[17], or tank circuits[18], to read out the state of the qubit, an *Andreev interferometer* has been used.

An Andreev interferometer is a piece of normal metal connected to two superconducting mirrors (in this case two wires which are connected to the qubit). The phenomenon of Andreev reflection from the superconductor/normal metal interface causes the resistance of the wire to be changed as a function of the difference in phase between the two superconductors. Because the wires are connected directly to the qubit, the phase difference across them is linked to the phase across the qubit, and by measuring the resistance of the wire the state of the qubit can be inferred.

Previous works have successfully carried out spectroscopy on persistent current qubits[17]. However, they have relied on SQUIDS and tank circuits to probe the state of the qubit by measuring the change in flux. This method strongly perturbed the qubit and measurement systems and suffers from a low resolution. With an Andreev interferometer probing the phase of the qubit directly, it is possible to carry out continuous measurements with relatively little back action of the qubit.

### 1.4 Work Completed For This Project

- Developed new high resolution process creating flux qubits, with a tri-layer germanium mask allowing for well defined Josephson junctions.
- Calculated relaxation and dephasing times for a flux qubit connected to an Andreev interferometer.
- Created a measurement setup that helps to maximize coherence times of a qubit.



- Observed the first resonant excitation of a flux qubit using an Andreev interferometer.

# Chapter 2

## Superconductivity and Josephson Junctions

### 2.1 Introduction

This chapter introduces the phenomenon of superconductivity and discusses two important effects arising from this, flux quantization and the Josephson effect, both of which are exploited in order to create flux qubits. A more detailed review of the behaviour of Josephson junctions can be found in [19] and [20].

Superconductivity is a property observed in certain materials at low temperature. It is characterized by the disappearance of electrical resistance in the material and by the exclusion of magnetic fields from within the bulk of the material, which is known as the Meissner effect.

A microscopic theory of superconductivity has been given by Bardeen, Cooper and Schrieffer[21]. They showed that in a superconducting material at low temperatures, it becomes energetically favourable for electrons to form pairs with equal and opposite spin and momentum. These electron pairs, also called Cooper pairs, are held together by an attractive force transmitted by phonons in the lattice. Because this force is attractive, the energy of the Cooper pairs is lowered and they form an energy state below that of the unpaired electrons at the Fermi energy. The Cooper pairs have a total spin of zero and so are no longer bound by the Pauli exclusion principle. They can all occupy the same energy state and can be described by a single coherent wave function

$$|\Psi(\mathbf{r}, \mathbf{t})| \exp(i\phi(\mathbf{r}, \mathbf{t})) \tag{2.1}$$

Superconductors, therefore are systems containing tens of thousands of

electron pairs that can be described by a single macroscopic wave function. This means that they display quantum interference behaviour similar to that observed with atoms at a microscopic scale, on a macroscopic scale. This leads to phenomenon which are important to this project, flux quantization and the Josephson effect, which are discussed in more detail below.

## 2.2 Flux quantization

Flux quantization is the phenomenon by which the flux threading a loop of superconductor is quantized in units of

$$\Phi_0 = \frac{h}{2e} \quad (2.2)$$

This arises from the condition that at any point the wave function must be single valued[19]. Consider a loop of superconducting metal. The phase difference between points X and Y in a piece of superconductor is equal to

$$(\Delta\phi)_{XY} = \phi_x - \phi_y = 2\pi \int_X^Y \frac{\hat{\mathbf{x}}}{\lambda} \cdot d\mathbf{l} \quad (2.3)$$

where  $\lambda$  is the wavelength,  $\hat{\mathbf{x}}$  is a unit vector in the direction of wave propagation and  $\mathbf{l}$  is an element of a line joining X and Y. For simplicity's sake the wave has been assumed to be one dimensional in this case.

The wavelength of the electron pairs is related to the momentum by

$$\lambda = h/P \quad (2.4)$$

and the momentum of the pair is made up of contributions from the current flow and magnetic field such that

$$\mathbf{P} = 2m\mathbf{v} + 2e\mathbf{A} \quad (2.5)$$

where  $\text{curl}\mathbf{A} = \mathbf{B}$ .  $v$  is the velocity of the pairs and is related to the supercurrent density  $j_s$  by

$$j_s = (1/2)n_s \cdot 2e \cdot v \quad (2.6)$$

where  $1/2n_s$  is the density of Cooper pairs.

The phase difference described in 2.3 can, therefore be written as

$$(\Delta\phi)_{XY} = \frac{4\pi m}{hn_s e} \int_X^Y \mathbf{J}_S \cdot d\mathbf{l} + \frac{4\pi e}{h} \int_X^Y \mathbf{A} \cdot d\mathbf{l} \quad (2.7)$$

If we now consider a line that joins points X, Y and Z to form a closed path XYZX then the change in phase around this loop is equal to

$$(\Delta\phi)_{XY} = \frac{4\pi m}{\hbar n_s e} \oint \mathbf{J}_S \cdot d\mathbf{l} + \frac{4\pi e}{\hbar} \oint \mathbf{A} \cdot d\mathbf{l} \quad (2.8)$$

Applying Stokes theorem this then becomes

$$(\Delta\phi)_{XY} = \frac{4\pi m}{\hbar n_s e} \oint \mathbf{J}_S \cdot d\mathbf{l} + \frac{4\pi e}{\hbar} \int \int_S \mathbf{B} \cdot d\mathbf{S} \quad (2.9)$$

where  $\mathbf{S}$  is the area bounded by the loop. Since this wavefunction must be single valued, at any point the total change in flux must be equal to  $2\pi n$  where  $n$  is integer. From this we obtain

$$\frac{m}{n_s e^2} \oint \mathbf{J}_S \cdot d\mathbf{l} + \int \int_S \mathbf{B} \cdot d\mathbf{S} = n \frac{\hbar}{2e} \quad (2.10)$$

The left hand side of this equation is known as the fluxoid and is made up of the line integral of the current density around the loop and the magnetic flux threading the loop. 2.10 shows that the fluxoid must be a multiple of the flux quantum  $\Phi_0$ . In most cases the first term in the fluxoid equation is very small and so it is proper to say that the flux contained can only exist in multiples of  $\Phi_0$ .

## 2.3 Fundamental Josephson Equations

A Josephson junction is a weak link in a superconducting wire. This weak link can take the form of a layer of oxide (referred to as a SIS junction), a piece of normal metal (referred to as a SNS junction), a constriction in the wire or a point contact.

The SIS Josephson junction is the type most commonly used in constructing qubits. Because of their quantum nature the Cooper pairs can tunnel through the insulating layer and a supercurrent can flow through the junction. The magnitude of this current is dependent on the phase difference between the two superconductors. Two fundamental equations describe the behaviour of the Josephson junction. The first is

$$I_S = I_c \sin \phi \quad (2.11)$$

where  $\phi = \phi_1 - \phi_2$ , the phase difference across the junction and  $I_c$  is known as the critical current of the junction. This shows that the current flowing

through a Josephson junction is an oscillating function of the phase difference between the two superconductors.

The second fundamental Josephson equation is

$$\dot{\phi} = \frac{2e}{\hbar}V = \frac{2\pi}{\Phi_0}V \quad (2.12)$$

This is known as the Josephson voltage-phase relationship and shows that a changing phase across the junction results in a constant voltage.

Re-arranging 2.3 gives

$$\phi = \phi_n = \arcsin I_S/I_c + 2\pi n \quad (2.13)$$

where  $-I_c \leq I_S \leq I_c$  and  $n$  is an integer. Applying this to 2.12 shows that when a steady current which is less than the junction's critical current is passed through the junction there is no voltage drop. In this case the junction is said to be in the *S state* where S stands for either superconducting or stationary.

If the current passed through the junction is greater than  $I_c$  then the junction switches to the resistive or R state. In this state the junction has a resistance  $R_n$ , there is a voltage drop across the junction, and the total current is made up of both superconducting and normal components

$$I = I_S + I_n \quad (2.14)$$

From 2.12 a non zero voltage,  $\bar{V}$ , across junction leads to phase growing with time

$$\phi = \omega_J t + const \quad (2.15)$$

Using 2.3 this leads to a supercurrent oscillating with frequency

$$\omega_J = \frac{2e}{\hbar}\bar{V} = \frac{2\pi}{\Phi_0}\bar{V} \quad (2.16)$$

## 2.4 The RCSJ Model of a Josephson Junction

The classical behaviour of a Josephson junction can be represented by what is often called the Resistively Capacitive Shunted (RCSJ) Model. This model, shown in Figure 2.1 consists of a non-linear superconducting component shunted by a capacitor and resistor. The resistor represents the resistance of the junction when it is in its normal state,  $R_n$ , and the capacitance of the

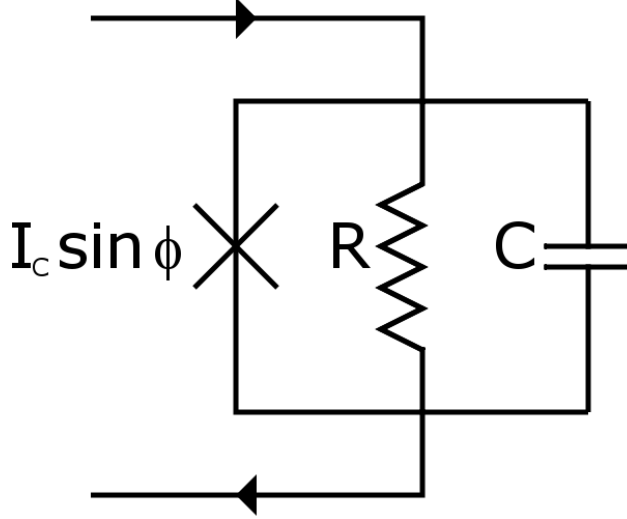


Figure 2.1: The RCSJ model of a Josephson junction. Junction is modeled as a phase driven supercurrent shunted by a resistance  $R$  and capacitance  $C$ .

junction,  $C$ , which can be calculated from its geometry. The total current through the junction is then

$$I = I_c \sin \phi + \frac{V}{R} + C \frac{dV}{dt} \quad (2.17)$$

Substituting from 2.12 then gives

$$I = I_c \sin \phi \frac{1}{R} \frac{\Phi_0}{2\pi} \frac{d\phi}{dt} + C \frac{\Phi_0}{2\pi} \frac{d^2 \phi}{dt^2} \quad (2.18)$$

The superconducting element of the circuit has a non-linear inductance. Consider a junction undergoing an arbitrary process  $\phi(t)$  and small variation  $\tilde{\phi}$ . Inserting this into 2.3 and 2.12 and expanding  $\sin(\phi(t) + \tilde{\phi})$  with a Taylor expansion in  $\tilde{\phi}$  gives

$$\tilde{I}_S = \frac{1}{L_S} \int \tilde{V} dt \quad (2.19)$$

$$L_S^{-1} = L_c^{-1} \cos \phi \quad (2.20)$$

$$L_C \equiv \frac{\hbar}{2eI_c} \quad (2.21)$$

This shows that the junction has a non-linear inductance dependant on the phase across the junction which can take on negative values.

## 2.5 Josephson Energy and Charging Energy

There are two attributes used to characterize Josephson junctions, the Josephson energy and the charging energy.

The Josephson energy is related to the energy stored in a Josephson junction when a supercurrent is passed through it. When it is in the S state, the voltage drop across the junction is zero and so no energy is dissipated from the junction. The work done on the junction by an external system can be written as

$$W_S = \int_{t_1}^{t_2} I_S V dt \quad (2.22)$$

Applying equations 2.3 and 2.12 gives us the work done in terms of the Josephson phase.

$$W_S = \frac{\hbar I_c}{2e} \int_{\phi_1}^{\phi_2} \sin \phi = \frac{\hbar I_c}{2e} (\cos \phi_1 - \cos \phi_2) \quad (2.23)$$

The work done can be thought of as the difference between 2 potential energies

$$W_S = U_S \phi_2 - U_S \phi_1 \quad (2.24)$$

We can, therefore, define a junction potential energy

$$U_S(\phi) = E_j(1 - \cos \phi) + const \quad (2.25)$$

where  $E_j$  is the Josephson energy.

$$E_j \equiv \frac{\hbar I_c}{2e} \quad (2.26)$$

The charging energy of a Josephson junction is the energy needed for one electron to tunnel across the junction. It is equal to

$$E_C \equiv (2e)^2/2C \quad (2.27)$$

The ratio of Josephson energy to charging energy is an important parameter for the construction of qubits. The two values associated with each

energy, the phase  $\phi$  and charge  $Q$ , are conjugate so that when one is well defined there is a large uncertainty in the other. For  $E_j \gg E_c$   $\phi$  is well defined and there are large quantum fluctuations in  $Q$  and so the phase is used to measure the quantum state of the system. Such systems are known as phase or flux qubits. When  $E_j \ll E_c$  the reverse is true and  $Q$  can be measured to determine the state. These systems are known as charge qubits.

The value of  $E_j/E_c$  is determined by the geometric properties of the junction and the size of the oxide barrier and can be engineered during the fabrication process.

Figure 2.2 shows the IV curve of a typical Josephson junction. The important parameters of the junction can be calculated from this curve. The slope of the linear sections of the curve is equal to  $R_n$ , the resistance of the junction in its normal state. The transition between the linear and zero voltage sections of the curve gives the critical current of the junction,  $I_c$ , which can be used to calculate  $E_j$ . Finally, by measuring the separation between the two linear sections of the curves intersection with the x-axis, the charging energy  $E_C$  can be calculated.

## 2.6 Quantum Behaviour of Josephson Junctions

The construction of qubits relies on the fact that Josephson junctions exhibit quantum behaviour. The simplest way to describe some of this quantum behavior is to model the Josephson junction as a particle moving in a potential energy,  $U$ . To find  $U$ , we can use a process analogous to that of finding the Gibbs energy in a thermodynamic system. In any system acting under a force,  $F$ , the total energy can be calculated by

$$G = E - Fx \quad (2.28)$$

where  $E$  is the intrinsic energy of the system and  $x$  is a generalized coordinate corresponding to the Force  $F$ , and is chosen in such a way that the product  $F\dot{x} = P$ , where  $P$  is the instantaneous power flowing into the system. The force in the system under discussion here is current,  $F = I$ , and so

$$P = IV \quad (2.29)$$

Using 2.12 this means that

$$x = \int V dt = \frac{\hbar\phi}{2e} + C \quad (2.30)$$



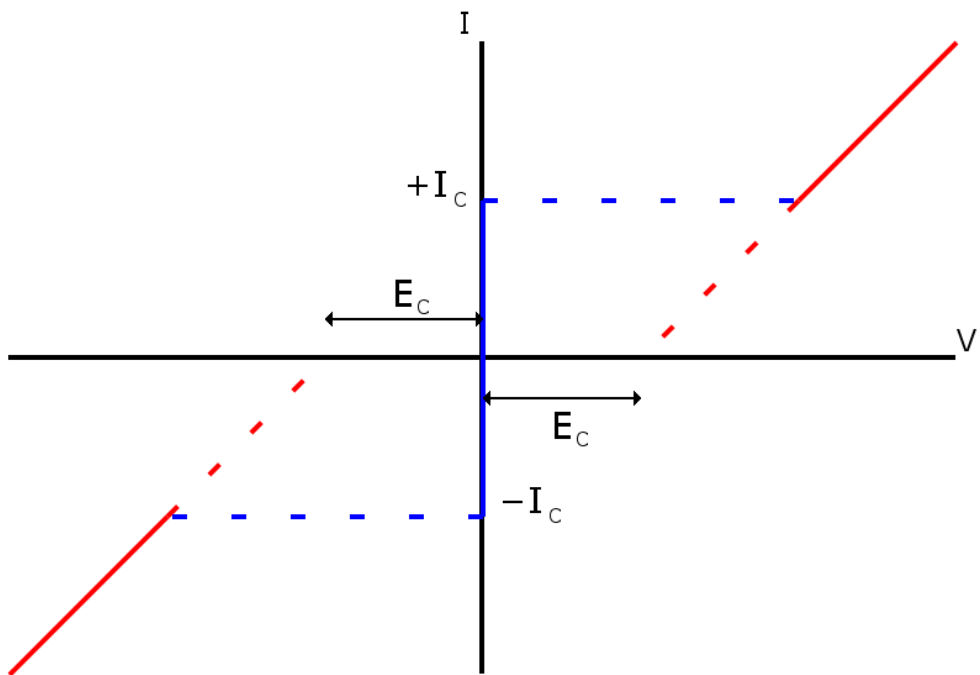


Figure 2.2: Ideal IV curve of a Josephson junction. The solid red lines show the resistive state of the junction and the blue lines the S state. The switch between these two states occurs at the critical current, which can then be used to calculate the Josephson energy(2.26). By extrapolating where the resistive part of the curve would intercept the x-axis, the charging energy can be measured(2.27).

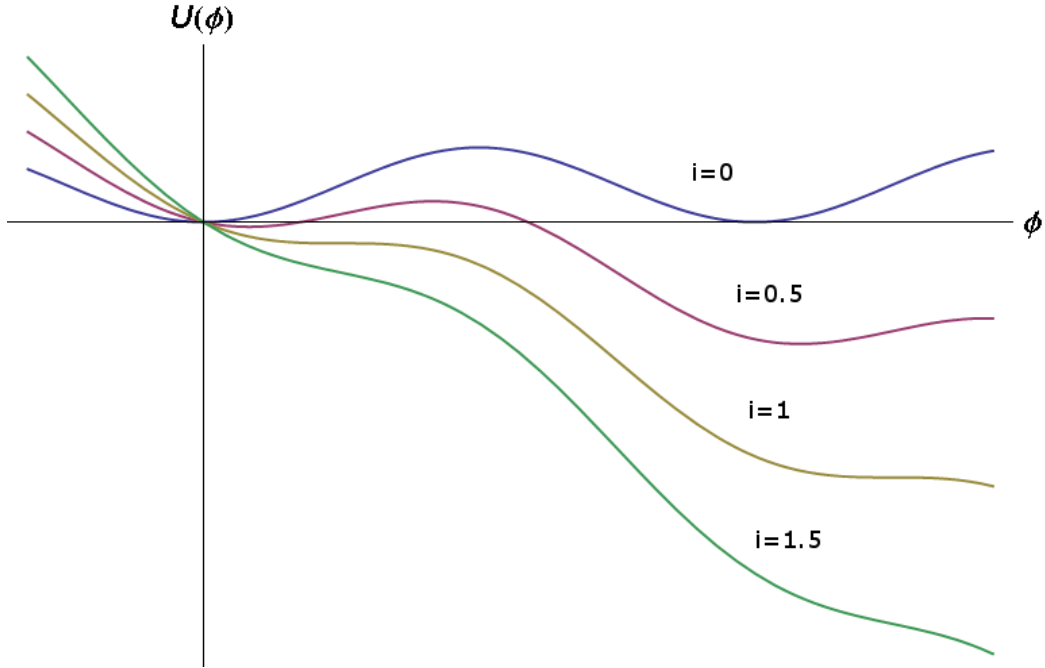


Figure 2.3: Potential energy of Josephson junction for different values of  $i = I/I_c$ .

where  $C$  is a constant.

The total energy of the system is thus equal to

$$U(\phi) = G = U_s(\phi) - I \frac{\hbar\phi}{2e} \quad (2.31)$$

Taking the  $U_s$  to be that which was calculated in 2.25

$$U(\phi) = E_c(1 - \cos \phi) + I \frac{\hbar\phi}{2e} + C = E_c(1 - \cos \phi - i\phi) + C \quad (2.32)$$

This takes the form as a washboard potential (see Figure 2.3). This is a series of potential wells tilted by the ratio of the current through the junction to the critical current  $I_c$ .

The height of the barrier separating the potential wells,  $U_0$  is equal to

$$2E_J [(1 - i^2)^{1/2} - i(\arccos i)] \quad (2.33)$$

where  $i = I/I_c$ . When  $i > 1$  then there is no barrier between the wells and the particle rolls down the slope, leading to a changing phase. From 2.12

this leads to a constant voltage across the junction. When  $i \ll 1$  then the barrier height that the particle is trapped within one well and the junction is in the S state.

When trapped within the well the particle oscillates with a frequency equal to

$$\omega_0 = \omega_p(1 - i^2)^{1/4} \quad (2.34)$$

Irradiating the junction with microwaves close to this frequency can cause resonant activation of the junction, allowing the particle to escape over the top of the barrier and causing the junction to switch to a voltage state[22].

However, because the Josephson junction is also a quantum system there is also a possibility for the particle to tunnel through the barrier and escape the well. Further experiment showed that the energy levels inside each well were quantized[23][24], and that by the application of the microwaves the junction could be excited into a higher energy state, increasing the probability of tunnelling. Because the shape of the well is not a perfect harmonic oscillator, the energy levels are not equidistant and spectroscopy could be carried out on the junctions.

This quantization of energy levels of Josephson junctions is exploited to create flux qubits, as discussed in the next chapter.

# Chapter 3

## Flux Qubits - A Mesoscopic Two State System

### 3.1 Flux Qubits

The macroscopic quantum nature of Josephson junctions makes them ideal candidates for qubits[25]. This chapter discusses the physics pertinent to one such qubit, the flux qubit, and examines the theory necessary to describe the behaviour of the ideal two state system a qubit is meant to replicate. A more detailed review of the behaviour of both flux and charge qubits can be found in [26]. There are two important variables of the Josephson junctions, the phase  $\phi$  and the charge  $2ne$  where  $n$  is the number of Cooper pairs in the superconductor.

These quantities are conjugate such that

$$[n, \phi] = i\hbar \tag{3.1}$$

So that if  $n$  is well defined then there is a large uncertainty in  $\phi$  and vice versa. The accuracy with which  $n$  and  $\phi$  can be determined is controlled by the ratio of  $E_c$  to  $E_j$ . In the case where  $E_c \gg E_j$  then it is the charge that is well defined and so is used to designate the state of the qubit. Such devices are known as charge qubits[27].

In the opposite case  $E_j \gg E_c$ , the junction phase and the junction current  $I_p$  are well defined and so are used as the control variable. Such qubits are known as flux or persistent current qubits. This is the type of qubit used in this project and the behaviour of such a qubit is described in this chapter.

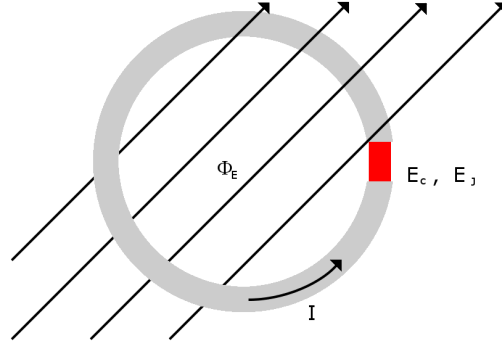


Figure 3.1: A simple RF squid consisting of a loop of superconductor (shown in gray) interrupted by a Josephson junction (shown in red). External flux  $\Phi_e$  generates a current  $I$  around the loop. For a given flux the magnitude and direction of this current is controlled by the loop geometry and junction parameters  $E_j$  and  $E_c$ .

### 3.1.1 A Simple Flux Qubit - The RF Squid

The simplest implementation of a flux qubit is a RF squid, a loop of superconductor interrupted by a Josephson energy with capacitance  $C$  and critical current  $I_c$  (see Figure 3.1). This method was first experimentally realized by [28].

Using 2.3 and 2.12 it can be shown that the phase drop across the junction  $\phi$  is related to the flux threading the loop  $\Phi$

$$\phi = 2\pi \frac{\Phi}{\Phi_0} \quad (3.2)$$

$\Phi$  is given by

$$\Phi = \Phi_e - LI \quad (3.3)$$

where  $\Phi_e$  is the externally applied flux,  $L$  is the inductance of the loop and  $I$  is the loop current.

Therefore, 3.2 can be rewritten as

$$\phi = \phi_e - \lambda i \quad (3.4)$$

where

$$\phi_e \equiv 2\pi \frac{\Phi_e}{\Phi_0} \quad (3.5)$$

$$\lambda \equiv 2\pi \frac{LI_c}{\Phi_0} \quad (3.6)$$

When junction is in the S state

$$I = I_c \sin \phi \quad (3.7)$$

Inserting this into equation 3.5 gives

$$\phi_e = \phi + \lambda \sin \phi \quad (3.8)$$

Figure 3.2 shows the variation of  $\phi$  with  $\phi_e$ . For  $\lambda = 0$  there is a linear dependence. This becomes increasingly non-linear with increasing  $\lambda$  until at  $\lambda = 1$ ,  $\phi$  becomes multivalued.

In order to analyze the stability of each of these states it is useful to again consider the potential energy of the system. This differs from that given for the single current biased junction in 2.32 by the introduction of an inductive term

$$U_L = \frac{LI^2}{2} \quad (3.9)$$

This gives a final potential

$$U = E_C \left[ 1 - \cos \phi + \frac{(\phi - \phi_e)^2}{2\lambda} \right] \quad (3.10)$$

which is shown in Figure 3.3. At  $\lambda < 1$  there is only one minimum in this potential, corresponding to the S state of the system. At  $\lambda > 1$  we have a potential formed from the superposition of a quadratic function and an oscillating function, leading to a number of potential wells. These wells have a minimum that satisfy the condition

$$k \equiv \frac{d^2U}{d\phi^2} = E_c[\cos\phi + \lambda^{-1}] > 0 \quad (3.11)$$

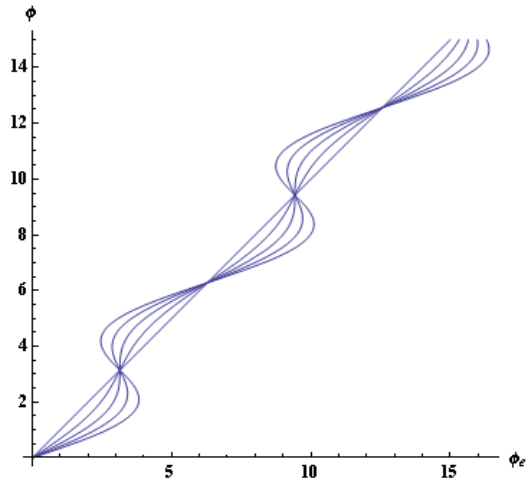
or

$$\frac{d\phi}{d\phi_e} > 0 \quad (3.12)$$

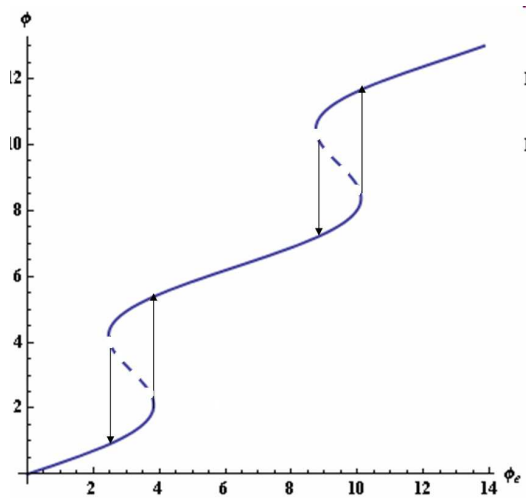
This means that in Figure 3.2 sections of  $\phi(\phi_e)$  with positive slopes are stable while sections with negative slopes are unstable. This leads to the behaviour shown, with sudden jumps in  $\phi$  at

$$\phi_e^\pm = 2\pi n \pm (\lambda^2 - 1)^{1/2} + \arcsin(\lambda^{-1}) - \pi/2 \quad (3.13)$$

This behaviour can be easily visualized by modelling the system as a particle moving in the potential given in 3.10, as shown in Figure 3.4. At  $\phi_e = 0$  the particle is trapped in the lowest potential well. Each well represents a different current direction, and equivalently a flux direction through the



(a)



(b)

Figure 3.2: Phase  $\phi$  around a RF squid as a function of external phase  $\phi_e$ . (a) Shows how the function changes for values of  $\lambda$  between 0 and 2. As  $\lambda$  increases the function becomes increasingly linear, and becomes multivalued at  $\lambda > 1$ . (b) Shows the phase jumps in  $\phi$ . The sections of the curve with negative slopes are unstable and so phase jumps occur at  $\lambda = \phi_e^\pm$ .

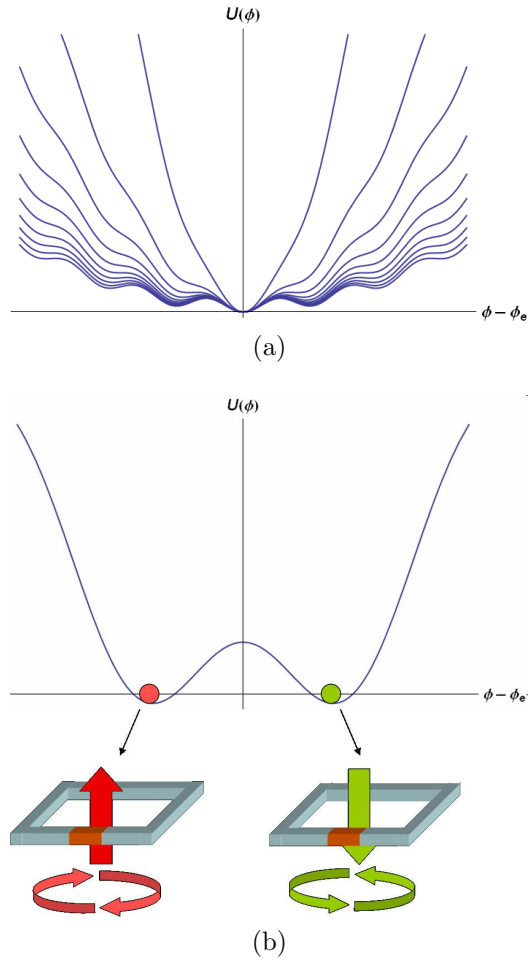


Figure 3.3: The potential energy of the RF squid  $U$  as a function of the phase  $\phi$ . (a) Shows the change in potential for increasing values of  $\lambda$ . As lambda increases the potential becomes a series of potential wells, representing alternating current directions. (b) Shows the energy of the system for  $\lambda = 5$  and  $\phi_e = 0.5\Phi_0$ . Here the system has two potential wells. When the particle is trapped in the left well the current flows clockwise, and when the particle is trapped in the right well the current flows anti-clockwise.



squid, so that when the particle is trapped in the left well the current flows clockwise around the squid and the total flux threading the squid points ‘up’, and when the particle is in the right well the current flows anti-clockwise and the flux points ‘down’. As  $\phi_e$  is increased the oscillating part of the potential is shifted relative to the quadratic part. This leads to the well the particle is trapped in being raised to higher energies and the barrier between this well and the next well being lowered. At  $\phi_e = \phi_e^+$  the barrier is reduced to zero and the particle can escape to the lower well, leading to a sudden jump in the phase and change in the current direction. This process then repeats itself as  $\phi_e$  continues to increase.

### 3.1.2 Macroscopic Quantum Effects

The above section describes the classical behaviour of a RF squid. In reality, macroscopic quantum effects can lead to important deviations from this behaviour. In the classical system at  $T = 0$  the particle can only escape from the well when  $\phi_e = \phi_e^\pm$ . However, quantum mechanics allows for the possibility of the particle tunnelling through the barrier. This leads to the system being the superposition of two basis states.

$$|\Psi\rangle = \alpha|\uparrow\rangle \pm \beta|\downarrow\rangle \quad (3.14)$$

The  $|\uparrow\rangle$  represents the flux through the loop being in the ‘up’ direction (and the current around the loop flowing in the clockwise direction) and the  $|\downarrow\rangle$  state represents the opposite case with the flux pointing in the ‘down’ direction and the current flowing anti-clockwise around the loop.

When the applied flux is equal to  $\Phi_E = \Phi_0/2$ , known as the degeneracy point, the system is symmetrical and due to tunnelling the eigenfunctions of the system are the symmetrical and anti-symmetrical superposition of the basis states, with  $\alpha = \beta = 1/\sqrt{2}$ . This leads to the system having a ground and excited state, with the wavefunction of the system in the ground state being equal to

$$|0\rangle = \frac{1}{\sqrt{2}}(|\uparrow\rangle - |\downarrow\rangle) \quad (3.15)$$

and in the excited state being

$$|1\rangle = \frac{1}{\sqrt{2}}(|\uparrow\rangle + |\downarrow\rangle) \quad (3.16)$$

The energy gap between the two states at the degeneracy point is  $\Delta$  and away from the degeneracy point is

$$\nu = (\Delta^2 + \epsilon^2) \quad (3.17)$$

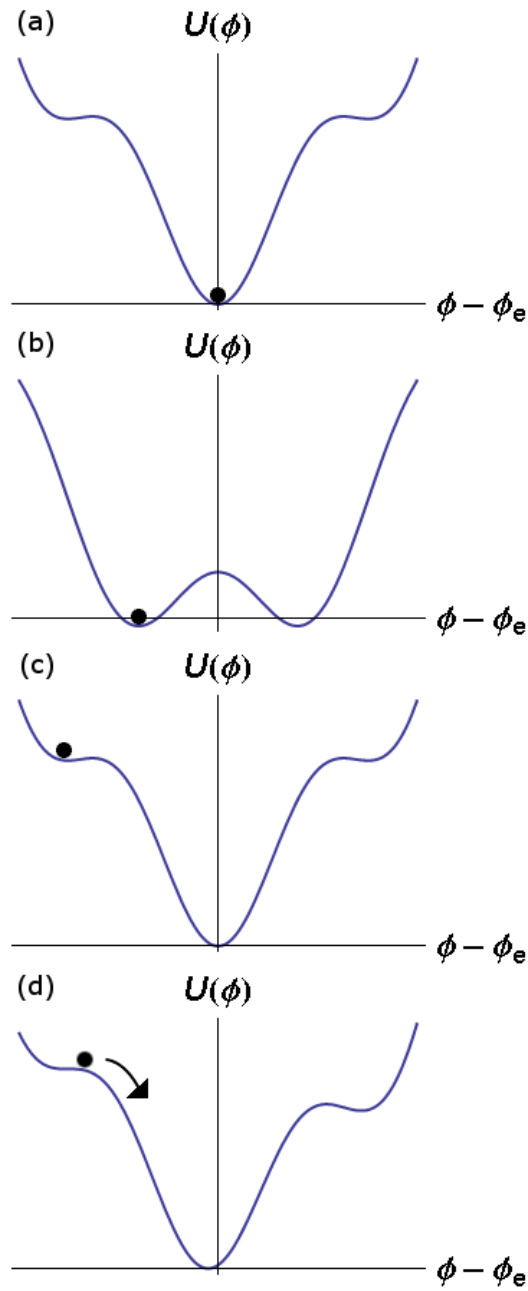


Figure 3.4: Potential energy of a single junction RF squid for different values of  $\Phi_e$ . (a)  $\Phi_e = 0$ , particle is trapped in the lower well. (b)  $\Phi_e = \Phi_0/2$ , wells are equal. (c)  $\Phi_e = \Phi_0$ , particle is trapped in the upper well. (d)  $\Phi_e = .667\Phi_0/2\pi$ , particle escapes from the upper well to the lower well, causing sudden change in phase and current.

where

$$\epsilon = 2I_q(\Phi_E - \Phi_0/2) \quad (3.18)$$

### 3.1.3 The Three Junction Flux Qubit

A working qubit requires  $\lambda > 1$ . For a single junction qubit this requires a large loop size, making the qubit more susceptible to flux noise, or a large critical current, meaning that the qubit is more susceptible to thermal excitation.

This problem is overcome in the three junction persistent qubit developed by Mooji and Orlando[29][30].

This qubit consists of a superconducting loop interrupted by three Josephson junctions with Josephson energies  $E_{j1}$ ,  $E_{j2}$  and  $E_{j3}$ , with phase drops across each junction  $\phi_1$ ,  $\phi_2$  and  $\phi_3$ .

The junctions are designed in such a way that

$$E_{j1} = E_{j2} = \alpha E_{j3} \quad (3.19)$$

The critical inductance of the junctions is much greater than the geometric inductance of the loop,  $L_j/L_s > 1$ . Therefore, the phase around the loop can be considered as created by the external field only and can be written as

$$\phi_1 + \phi_2 + \phi_3 = -2\pi \frac{\Phi_e}{\Phi_0} \quad (3.20)$$

Combining this with 2.25 the total energy of the system can then be written as

$$\frac{U}{E_j} = 2 + \alpha - \cos \phi_1 - \cos \phi_2 - \alpha \cos(2\pi \frac{\Phi_e}{\Phi_0} + \phi_1 - \phi_2) \quad (3.21)$$

Figure 3.5 shows a contour plot of  $U(\phi_1, \phi_2)$ . This potential consists of a repeating pattern of cells, with each cell containing a double well potential that behaves in an analogous way to that discussed for the single junction qubit. By engineering the value of  $\alpha$  during the qubit construction the shape of the potential, and thus the behaviour of the qubit, can be controlled. For a value of  $\alpha = 0.8$  tunnelling the cells between the cells is prohibited but tunnelling between the wells within each cell is at values of flux close to  $\Phi_e/\Phi_0 = 0.5$ .

## 3.2 Describing Qubit Behaviour

A flux qubit is a two state system. In order to understand how a flux qubit will behave we will examine the mechanics of an ideal two state system

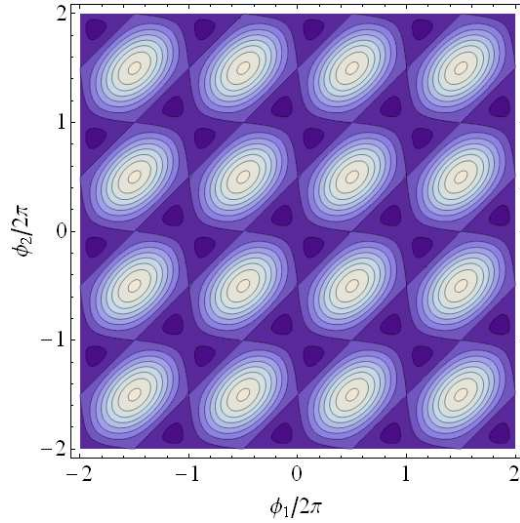


Figure 3.5: Potential Energy of the three junction flux qubit plotted as a function of  $\phi_1$  and  $\phi_2$ . The potential consists of a set of repeating cells. Each cell contains a double well potential. Tunnelling between the wells within each cell is possible at  $\Phi_e = \Phi_0/2$  but tunnelling between wells is prohibited.

under the influence of a perturbation with frequency  $\omega_{RF}$  which is close to the energy separation in our system  $\omega_{01} = (E_1 - E_0)/\hbar$ .

### 3.2.1 The Bloch Sphere

The Bloch sphere is a geometric representation of a two state system, which is useful for visualizing the behaviour of the qubit. The state of the system is represented by a vector, and the position of the end of the vector on a sphere represents the probability of finding the system in either state and gives information about the phase of the system.

An ideal qubit is a two state system[31]. Its wavefunction can be written as a superposition of the ground  $|\varphi_0\rangle$  and excited  $|\varphi_1\rangle$  states.

$$|\Psi\rangle = \alpha|\varphi_0\rangle + \beta|\varphi_1\rangle \quad (3.22)$$

where  $|\alpha|^2$  and  $|\beta|^2$  are the probabilities of finding the system in the ground or excited state after measurement, such that

$$|\alpha| + |\beta| = 1 \quad (3.23)$$

The Hamiltonian of the system can be represented by the spin model

$$H = -\frac{\hbar}{2}(\epsilon\sigma_z + \Delta\sigma_x) \quad (3.24)$$

where  $\epsilon$  is the energy bias as given in equation 3.18.

The wavefunction of a two state system can be represented by a vector, and the surface that this vector can be positioned on is known as the Bloch sphere, as shown in Figure 3.6. The angle between vector and the z-axis represents the amplitude of the eigenfunctions, with  $\alpha = 1$  when the vector is pointing straight up and  $\beta = 1$  when the vector is pointing straight down. The angle the projection of the vector on the xy plane makes with the y-axis gives the phase difference between the amplitudes  $\alpha$  and  $\beta$ .

$$|\Psi\rangle = e^{i\gamma} \left( \cos \frac{\theta}{2} |\varphi_0\rangle + e^{i\phi} \sin \frac{\theta}{2} |\varphi_1\rangle \right) \quad (3.25)$$

$e^{i\gamma}$  can be ignored so

$$|\Psi\rangle = \cos \frac{\theta}{2} |\varphi_0\rangle + e^{i\phi} \sin \frac{\theta}{2} |\varphi_1\rangle \quad (3.26)$$

### 3.2.2 Rabi Oscillations

A system driven by AC field with frequency equal to the energy separation between the two levels undergoes cycles of excitation and stimulated emission. The probability of finding the system in the excited state oscillates. This corresponds to the vector rotating about the z-axis on the Bloch sphere, as shown in Figure 3.7.

To derive results we shall use the method given in [32]. As described above, in the absence of any perturbation, the qubit can be described as a two level system with well defined basis eigenfunctions and eigenvalues such that

$$H_0|\varphi_0\rangle = E_0|\varphi_0\rangle H_0|\varphi_1\rangle = E_1|\varphi_1\rangle \quad (3.27)$$

The matrix Hamiltonian has the form

$$H_0 = \begin{pmatrix} E_0 & 0 \\ 0 & E_1 \end{pmatrix} \quad (3.28)$$

Now we introduce a perturbation to the system at the resonant frequency so that the new Hamiltonian becomes

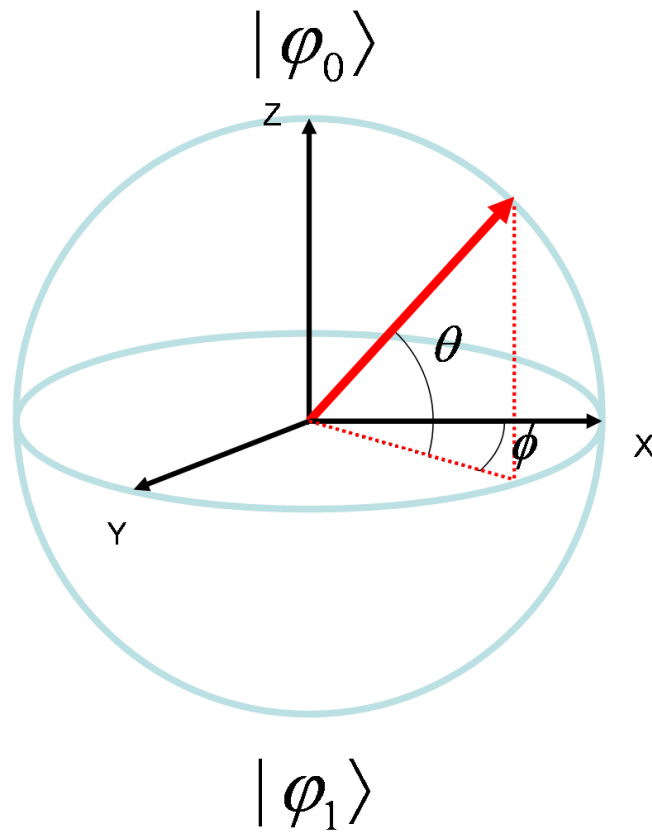


Figure 3.6: The Bloch sphere representation of a two state system. The qubit is represented by the vector shown in red. The vector can be in any position on the surface of the sphere. The angle  $\theta$  the vector makes with the x-y plane represents the probability of finding the qubit in either of the two states. The angle  $\phi$  that the vector makes with the x-axis represents that phase of the system.

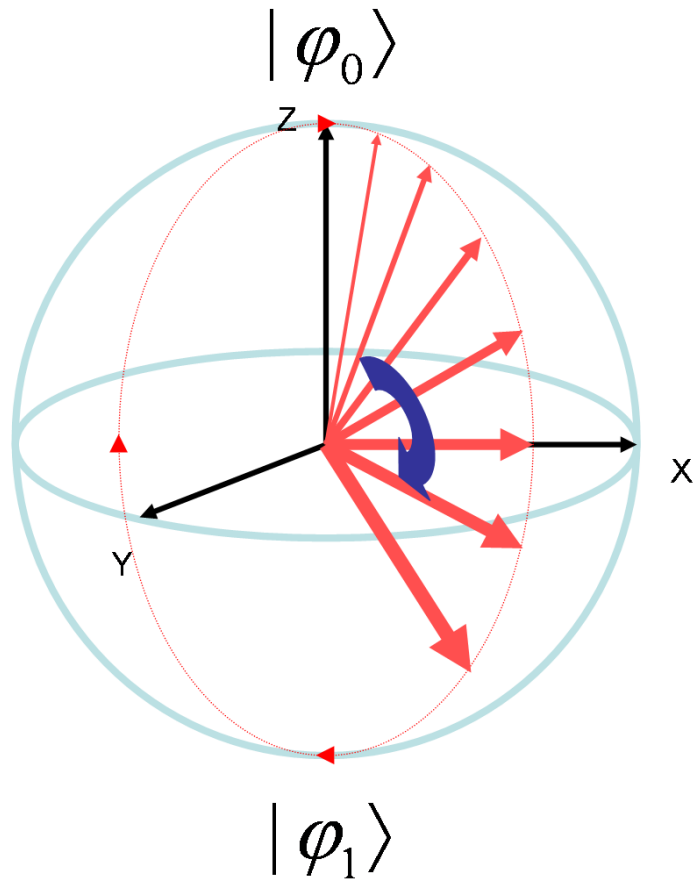


Figure 3.7: A resonant RF field causes a rotation of the state of the qubit about the z-axis of the Bloch sphere. This corresponds to the probability of finding the qubit in the excited oscillating between 1 and 0.

$$H = H_0 + W \quad (3.29)$$

with eigenfunctions and values

$$H|\Psi_+ = E_+|\Psi_+\rangle H|\Psi_- = E_-|\Psi_-\rangle \quad (3.30)$$

With coupling matrix

$$W = \begin{pmatrix} W_{00} & W_{01} \\ W_{10} & W_{11} \end{pmatrix} \quad (3.31)$$

$$W_{01} = W_{10}^* \quad (3.32)$$

$$W_{00} = W_{11} = 0 \quad (3.33)$$

$$E'_0 = E_0 + W_{00}E'_1 = E_1 + W_{11} \quad (3.34)$$

By diagonalizing the Hamiltonian using the method given in [32], we obtain the eigenvalues

$$E_{\pm} = \frac{1}{2}(E_0 + E_1) \pm \sqrt{(E_0 + E_1)^2 + 4|W_{01}|^2} \quad (3.35)$$

and the eigenfunctions

$$|\Psi_+\rangle = \cos\left(\frac{\theta}{2}\right) e^{-i\phi/2}|\varphi_0\rangle + \sin\left(\frac{\theta}{2}\right) e^{i\phi/2}|\varphi_1\rangle \quad (3.36)$$

$$|\Psi_-\rangle = \cos\left(\frac{\theta}{2}\right) e^{-i\phi/2}|\varphi_0\rangle - \sin\left(\frac{\theta}{2}\right) e^{i\phi/2}|\varphi_1\rangle \quad (3.37)$$

$\theta$  and  $\phi$  are the angles on the Bloch sphere described above and are given by

$$\tan\theta = \frac{2|W_{01}|}{E_0 - E_1} \quad (3.38)$$

$$W_{01} = e^{i\phi}|W_{10}| \quad (3.39)$$

The evolution of the system with time can be found using the time dependent Schrödinger equation

$$i\hbar \frac{d}{dt}|\Psi(t)\rangle = H|\Psi(t)\rangle \quad (3.40)$$

Applying this gives



$$|\Psi(t)\rangle = \alpha e^{-iE_+t/\hbar} |\Psi_+\rangle + \beta e^{-iE_-t/\hbar} |\Psi_-\rangle \quad (3.41)$$

By assuming that at  $t=0$ ,  $|\Psi(0)\rangle = |\varphi_0\rangle$ , and rearranging 3.36 to give us  $\varphi_0$  as a function of  $\Psi_-$  and  $\Psi_+$

$$|\Psi(0)\rangle = |\varphi_0\rangle = e^{i\phi/2} \left[ \cos\left(\frac{\theta}{2}\right) |\Psi_+\rangle - \sin\left(\frac{\theta}{2}\right) |\Psi_-\rangle \right] \quad (3.42)$$

we can then write

$$\Psi(t)\rangle = e^{i\phi/2} \left[ e^{-iE_+t/\hbar} \cos\left(\frac{\theta}{2}\right) |\Psi_+\rangle - e^{-iE_-t/\hbar} \sin\left(\frac{\theta}{2}\right) |\Psi_-\rangle \right] \quad (3.43)$$

The probability of finding the system in the excited state after a time  $t$  is  $P_1(t) = |\langle\varphi_1|\Psi(t)\rangle|^2$ . Using 3.43 we can write

$$\langle\varphi_1|\Psi(t)\rangle = e^{i\phi/2} \sin\left(\frac{\theta}{2}\right) \cos\left(\frac{\theta}{2}\right) [e^{-iE_+t/\hbar} e^{-iE_-t/\hbar}] \quad (3.44)$$

$$P_1(t) = \langle\varphi_1|\Psi(t)\rangle^2 \quad (3.45)$$

$$= \frac{1}{2} \sin^2\theta \left[ 1 - \cos\left(\frac{E_+ - E_-}{\hbar} t\right) \right] \quad (3.46)$$

$$= \sin^2\theta \sin^2\left(\frac{E_+ - E_-}{2\hbar} t\right) \quad (3.47)$$

Substituting 3.35 and 3.38 gives

$$P_1(t) = \frac{4|W_{01}|}{4|W_{01}|^2 + (E_0 - E_1)^2} \sin^2 \left[ \sqrt{4|W_{01}|^2 + (E_0 - E_1)^2} \frac{t}{2\hbar} \right] \quad (3.48)$$

This shows that the probability of finding the system in the excited state oscillates with a frequency

$$\omega_R = \sqrt{4|W_{01}|^2 + (E_0 - E_1)^2} \frac{1}{2\hbar} \quad (3.49)$$

For  $W_{01} \gg E_1 - E_0$  the amplitude of these oscillations is close to one.

### 3.2.3 Detuned Resonances

We have so far only looked at the case where the frequency of the driving field is equal to the energy separation between the two levels  $\omega_{RF} = E_1 - E_0/\hbar$ . We will now examine the case where there is a difference  $\delta$  between  $\omega_{RF}$  and the energy separation

$$\delta = \frac{E_1 - E_0}{\hbar} - \omega_{RF} \quad (3.50)$$

With this detuning taken into account 3.48 becomes

$$P_1(t) = \frac{|W_{01}|^2}{|W_{01}|^2 + \delta^2} \sin^2 \left[ \sqrt{|W_{01}|^2 + \delta^2} \frac{t}{2\hbar} \right] \quad (3.51)$$

Figure 3.8 shows the effect of detuning on Rabi oscillations, as  $\delta$  increases the amplitude of the oscillations decreases and the frequency increases.

### 3.2.4 Decoherence

The qubit cannot remain coherent in its excited state indefinitely. It will either relax back to the ground state by emitting a photon into the environment, or lose phase coherence while in the excited state. These two processes happen at rates  $\Gamma_d$  and  $\Gamma_\phi$  respectively. We can calculate the effect this will have on the Rabi oscillations using the method given in [33]. First we define the total off-diagonal decay rate as the sum of the other decay rates

$$\Gamma = \Gamma_d + 2\Gamma_\phi \quad (3.52)$$

To take account of the finite lifetime of each state we add an imaginary term to the energy such that

$$E'_n = E_n - i\hbar \frac{\Gamma}{2} \quad (3.53)$$

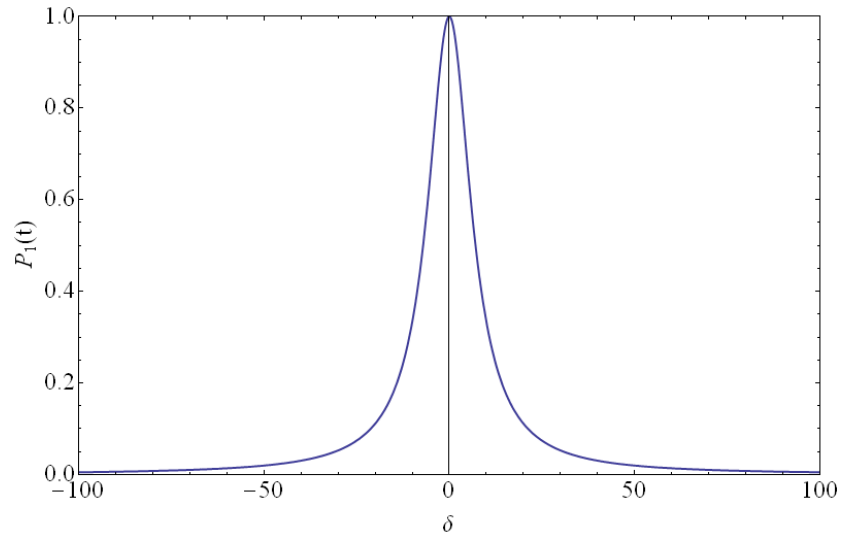
We can now rewrite equation 3.41 as

$$|\Psi(t)\rangle = \alpha e^{-iE_+t/\hbar} e^{-i\frac{\Gamma}{2}t/\hbar} |\Psi_+\rangle + \beta e^{-iE_-t/\hbar} e^{-i\frac{\Gamma}{2}t/\hbar} |\Psi_-\rangle \quad (3.54)$$

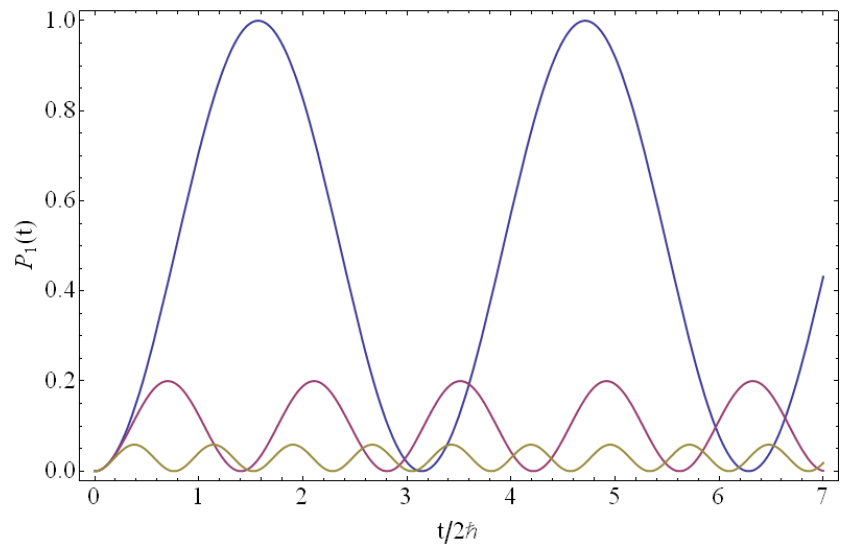
Using this method the probability of finding the system in the excited state after a time  $t$  becomes

$$P_1(t) = \frac{|W_{01}|^2}{|W_{01}|^2 - (\frac{\hbar}{2}\Gamma)^2} e^{-\Gamma t} \sin^2 \left[ \sqrt{|W_{01}|^2 - (\frac{\hbar}{2}\Gamma)^2} \frac{t}{2\hbar} \right] \quad (3.55)$$

Figure 3.9 shows Rabi oscillations for different values of  $\Gamma$ . At low rates of decoherence oscillations are damped, while for high rates no oscillations are seen before the system loses coherence.



(a)



(b)

Figure 3.8: (a) Shows  $P_1(t)$  as a function of detuning factor  $\delta$ . (b) Shows the Rabi oscillations at different values of  $\delta$  between 0 and  $4W_{01}$ . As delta increases the frequency increases and the amplitude decreases.

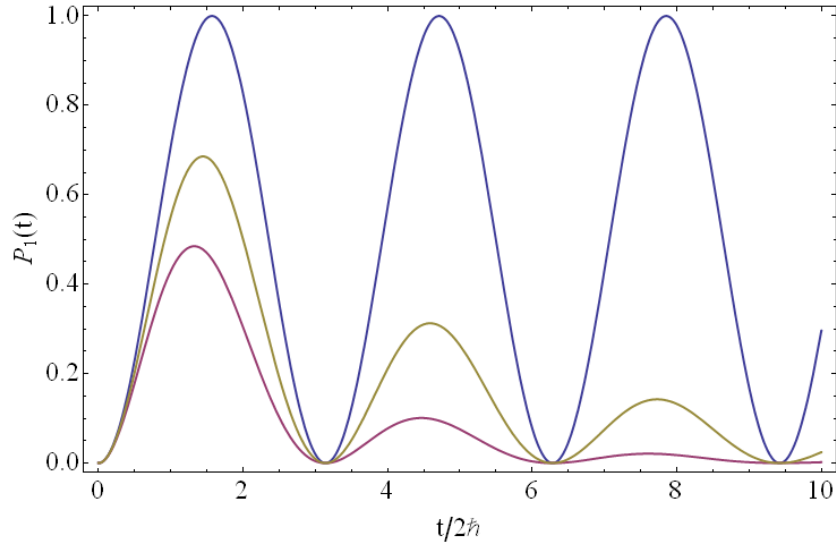


Figure 3.9: Shows  $P(t)$  for different values of the decoherence rate  $\Gamma$ . For  $\Gamma = 0$  the Rabi oscillations are sinusoidal. For  $\Gamma > 0$  the oscillations decay exponentially.

### 3.3 Summary

In this chapter we have shown how a superconducting loop and Josephson junctions can be used to construct a two state system. We have also examined the theory necessary to describe the behaviour of such a system under the influence of a resonant perturbation. In the next chapter the novel readout system used in this project, the Andreev interferometer will be introduced. Then in chapter 5 we will examine what happens when we combine a qubit with an Andreev interferometer, using the physics described in the preceding two chapters to build a model describing the behaviour of the Qubit/Interferometer system.

# Chapter 4

## The Proximity Effect and Andreev Interferometers

This chapter considers what happens when a superconductor is placed in contact with a normal metal. Close to the interface between the metals, the properties of both are changed. Superconductivity ‘leaks’ into the normal metal allowing it to carry a finite supercurrent. Electrons can move from the normal metal into the superconductor and remain uncoupled for a short distance, decreasing the density of Cooper pairs close to the interface. These changes are known collectively as the proximity effect. The proximity effect is responsible for the behaviour of Josephson junctions as discussed in the previous chapters, and the longer distance consequences of it are exploited in this project in order to create an Andreev interferometer.

### 4.1 S/N Interface

Figure 4.1 shows a superconducting to normal metal (S/N) interface. As mentioned above, the proximity of the superconductor to the normal metal changes its’ properties. Cooper pairs can move from the superconductor to the normal metal and remain coherent up to a certain distance from the interface. Conversely, quasi particles can move from the normal metal into the superconductor.

Ginzburg Landau theory describes this in terms of the superconducting condensate wave function[34]. The square modulus of this wave function describes the density of Cooper pairs within the superconductor. At a distance  $\xi_0$  away from the interface this wave function begins to decay as  $e^{-x/\xi_0}$  where  $x$  is the distance from the interface and  $\xi_0$  is the superconducting coherence length.

Inside the normal metal the wave function is still finite and decays as  $e^{-x/\xi_N}$  where  $\xi_N$  is referred to as the normal coherence length. This can be interpreted as there being a finite density of Cooper pairs in the normal metal close to the interface.

When the normal metal has an elastic mean free path,  $l$ , much shorter than the dimensions of the metal then it is said to be in the ‘diffusive’ or ‘dirty’ limit and  $\xi_N$  is given by

$$\xi_N = \sqrt{\frac{\hbar D}{2\pi k_B T}} \quad (4.1)$$

where  $k_B$  is the Boltzmann constant.  $D$  is the diffusion coefficient of the metal

$$D = \frac{v_F l}{3} \quad (4.2)$$

where  $v_F$  is the Fermi velocity.

In the opposite case, when  $l$  is much greater than the dimensions of the metal then it is said to be in the ‘clean limit’, and  $\xi_N$  is given by

$$\xi_N = \frac{\hbar v_F}{2\pi k_B T} \quad (4.3)$$

## 4.2 SNS Junctions

Now consider two superconductors separated by a length of normal metal, i.e. a SNS junction, as shown in Figure 4.2. If the length of the normal metal is shorter than  $2\xi_N$  then there will be significant overlap between the encroaching wave functions of the two superconductors. This means that a Cooper pair can remain coherent along the length of the normal metal and so a supercurrent can flow through it. The maximum critical current the normal metal can carry, in other words the critical current  $I_c$ , will be less than that of the two superconducting electrodes because it will be limited by the bottle neck in the wave function at the centre of the metal. This described is a SNS Josephson junction and will behave in the way described by equations 2.3 and 2.12 as well as have all the other properties given in chapter 2.

Work by de Gennes showed that the critical current in a SNS junction as a function of the junctions Length  $L$  has the relationship  $I_C(L) \propto e^{-L/\xi_N}$  [35]. From this, it follows that the critical current of the junction as a function of temperature should have the relationship  $I_C(T) \propto e^{-T/T_0}$ .

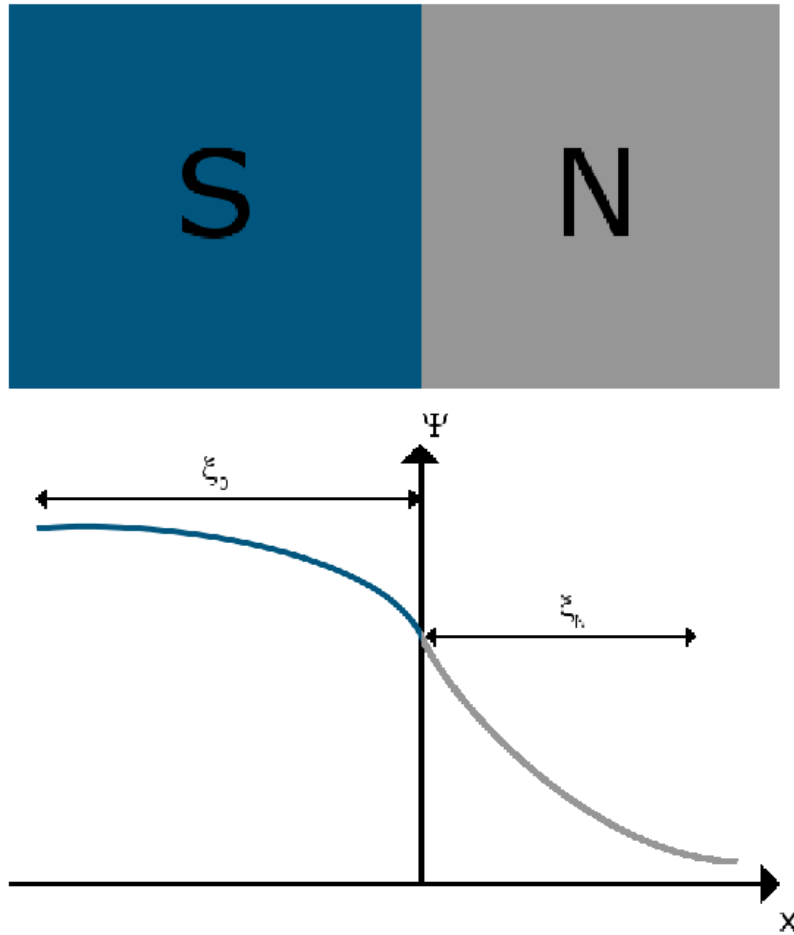


Figure 4.1: Behaviour of a superconducting wavefunction at the interface between a normal metal and a superconductor. The wave function begins to decay exponentially at a distance  $\xi_0$  from the interface. It continues to decay inside the normal metal allowing a finite density of Cooper pairs within the metal.

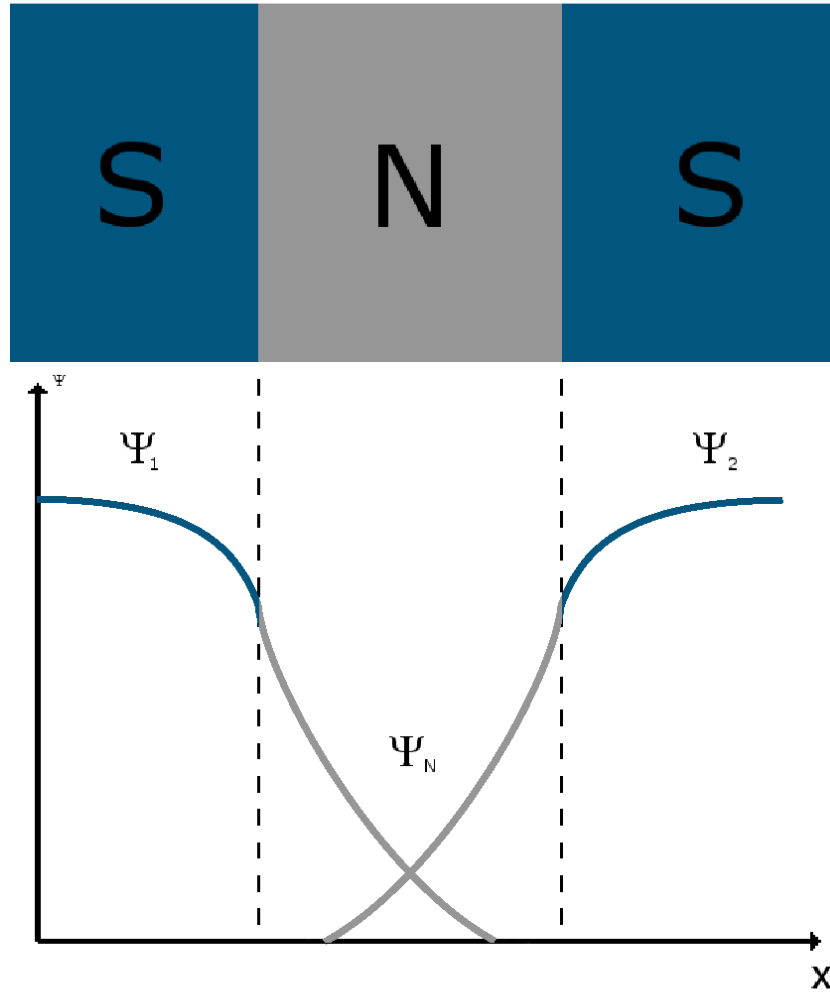


Figure 4.2: Behaviour of a superconducting wavefunction in a SNS junction.  $\Psi_1$  and  $\Psi_2$  are the wave functions of the two superconductors. The overlap between them in the normal metal allows a Cooper pair to remain coherent across its' length, meaning that a finite supercurrent can flow through the junction.



More recent work by Dubos et al has shown behaviour in junctions with  $L > \xi_N$  that deviates from this relationship[36]. A more rigorous theoretical analysis showed that in this case the critical current is given by

$$eR_N I_C = \frac{32}{3 + 2\sqrt{2}} E_T h \left[ \frac{L}{\xi_N} e^{-L/L_T} \right] \quad (4.4)$$

From this it follows that the critical current varies with temperature as  $I_C \propto T^{3/2} e^{-L/\xi_N}$

### 4.3 Tuning the Supercurrent in a SNS Junction

In 1997, Morpurgo et al showed that it is possible to influence the supercurrent through a SNS junction by injecting hot electrons into the normal metal[37]. The geometry they used for this experiment, shown in Figure 4.3, is similar to the geometry we use. It consisted of a Nb-Au-Nb SNS junction with vertical current lines that could be used to pass a current through the junction perpendicular to the direction of the supercurrent. They found that this current reduced and eventually completely suppressed the supercurrent in the junction.

The supercurrent through junctions has two contributions,  $I_{bs}$  from the bound states whose energy relative to the Fermi energy  $E_F$  in the electrodes is less than  $\Delta$  the superconducting energy gap, and  $I_{cont}$  the contribution of the continuum of states at a larger energy.

$$I_S(\phi) = I_{bs}(\phi) + I_{cont}(\phi) \quad (4.5)$$

The contribution of the bound states can be written as

$$I_{bs}(\phi) = \sum_n I[E_n^+(\phi)]p_n^+ + I[E_n^-(\phi)]p_n^- \quad (4.6)$$

Where  $E_N^+$  and  $E_N^-$  are the energy of the nth bound state carrying current in the positive and negative direction respectively,  $I(E_n^{+(-)})$  is the contribution of these states to the supercurrent and  $P^{+(-)}$  are their occupation probabilities.

Similarly, the contribution of the continuum can be written as

$$I_{cont}(\phi) = \left( \int_{-\infty}^{\Delta} + \int_{\Delta}^{\infty} \right) I(E, \phi) p(E, \phi) dE \quad (4.7)$$

Where  $I(E, \phi)$  is the net contribution of the states with energy between  $E$ , and  $E + dE$  and  $P(E, \phi)$  is the occupation probability.

Applying a voltage through the control electrodes changes the occupation of electronic states and so suppresses the supercurrent, as shown in Figure 4.3 (c).

Further experiments by Baselmans et al [38] showed that careful application of a control voltage could in fact change the Josephson current relationship  $I = I_C \sin(\Phi)$  to  $I = I_C \sin(\Phi + \pi)$  (see Figure 4.4).

## 4.4 Andreev Reflection

The discovery of the proximity effect presented a problem for theorists. The problem was this: how is it possible for an electron from the normal metal to move into a superconductor? At low temperatures the superconducting gap  $\delta$  is much greater than  $k_B T$ , and so there are no available energy states in the superconductor (see Figure 4.5). An elegant solution to this problem was provided in 1964 by A.F. Andreev[39]. He proposed a process by which an electron incident on the interface is reflected with its velocity, momentum and charge reversed. This means that an electron incident on the interface would be reflected, becoming a hole and traveling path along its incoming path (see Figure 4.6). At the same time, two quasi particles are injected into the superconductor where they survive for a short distance before combining to form a Cooper pair.

Andreev reflection is only perfect if the incoming particle is at the Fermi surface. For an incoming electron with energy,  $\epsilon_F + \delta$  and  $k_F + \delta k$  the reflected hole will have energy  $\epsilon_F - \delta$  and  $k_F - \delta k$ .

An important feature of Andreev reflection is that the reflected particle inherits phase information. An electron will gain a change of  $+\phi_s$  and a hole  $-\phi_s$ , where  $\phi_s$  is the phase of the superconductor. The reflected particle can be thought of as a time reversed version of the incoming particle and they will remain correlated for a distance  $L_\phi$ ,

$$L_\phi = \sqrt{\frac{\hbar D}{I} E} \quad (4.8)$$

This is the phase breaking or phase memory length of the system.

This means that for SNS systems such as that shown in Figure 4.2 an energy  $E_{Th}$ , known as the Thouless energy, can be defined such that

$$E_{Th} = \frac{\hbar D}{L_N^2} \quad (4.9)$$

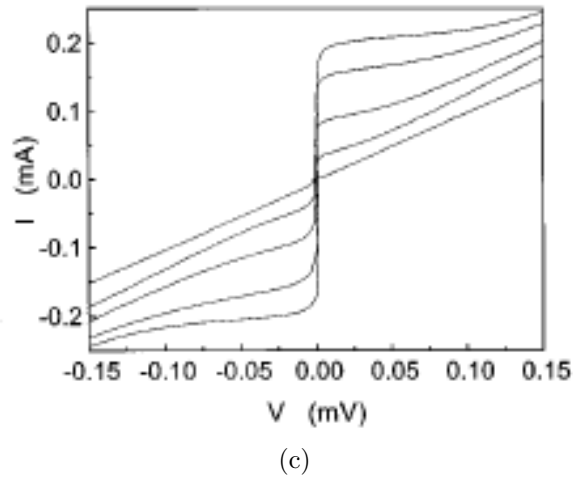
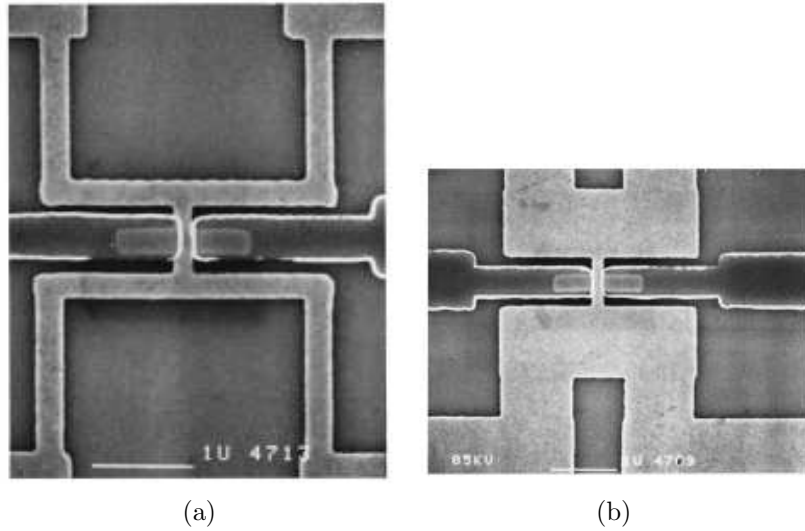


Figure 4.3: (a) and (b) SNS structures measured by Morpurgo et al [37]. These consist of an Au cross with Nb electrodes attached to the horizontal section to form a SNS junction. A current  $I_{ctrl}$  was used to change the properties of this junction. (c) IV curves for the SNS junction for different values of  $I_{ctrl}$ . Increasing  $I_{ctrl}$  decreases the critical current of the junction and very high values of  $I_{ctrl}$  suppress the supercurrent completely.

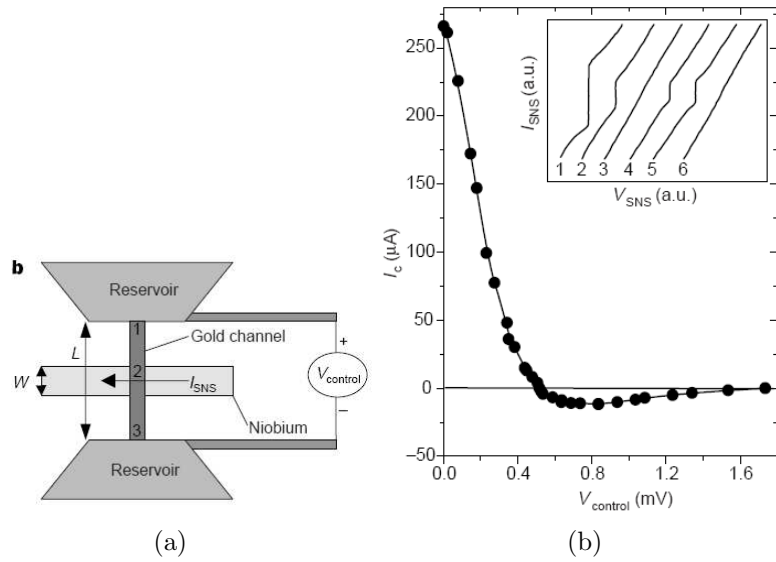


Figure 4.4: (a) Schematic representation of a sample measured by Baselmans et al[38]. (b) Results of experiment showing dependence of critical current on control voltage. For high  $V_{ctrl}$  supercurrent changes direction showing junction behaviour changing from  $I = I_c \sin(\phi)$  to  $I = I_c \sin(\phi + \pi)$ .

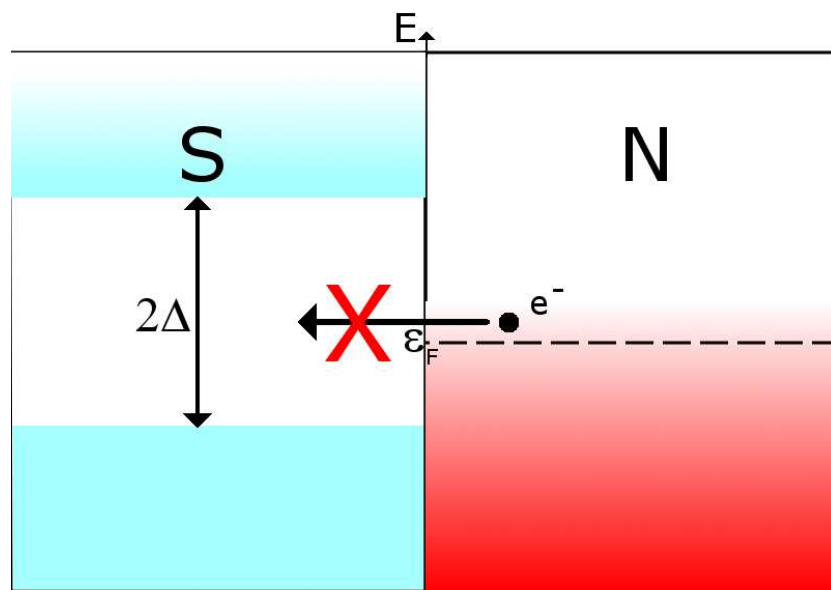


Figure 4.5: Diagram showing the energy levels at a SN interface. An electron  $k_B T$  above the Fermi energy in the normal metal N cannot move into the superconductor S because, as a consequence of the superconducting energy gap, there are no free energy levels.

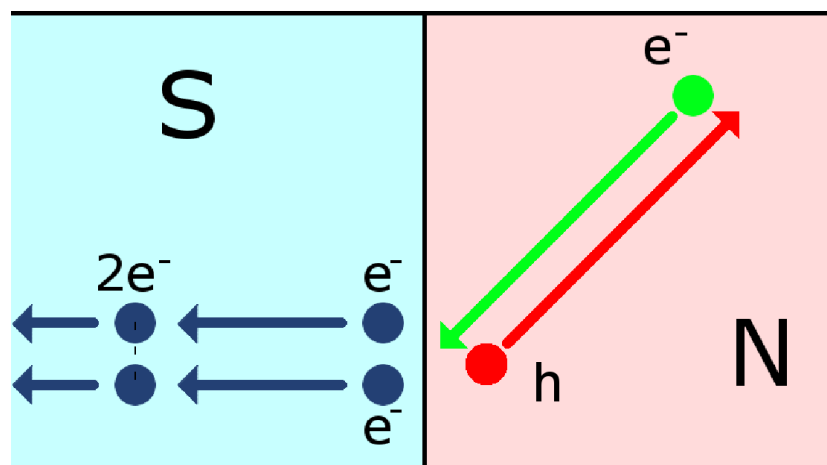


Figure 4.6: Diagram showing Andreev reflection. An incoming electron incident on a SN boundary has its charge and momentum reversed, becoming a hole which travels back along the incoming electrons path. Two quasi particles move into the superconductor where they survive for a short time joining to become a Cooper pair.

where  $L_N$  is the length of the normal section. This is the energy under which electron hole pairs will remain correlated across the whole system.

The interaction between the incoming and reflected particles leads to constructive or destructive interference effects and changes the electron density of the normal metal, leading to a change in the resistance. When the two are in phase, constructive interference takes place and there is maximum correlation between the electron and hole. This correlation leads to an energy gap in the metal similar to that observed in a superconductor. The size of the gap is equal to  $E_{Th}$  and as described above it is phase dependant, reaching a maximum when the phase difference  $\phi$  between the two superconductors is  $\phi = n2\pi$  and disappearing when  $\phi = n\pi$ , where  $n$  is an integer. This was first observed experimentally by Gu'eron et al in 1996[40]. Further experimental work by Ostrovsky showed that this gap was not perfect, with there being, in fact, a finite number of energy states below  $E_{Th}$ [41]. This type of energy gap is referred to as a soft gap.

The existence of an energy gap leads to a phase of the resistance of the normal metal. When  $\phi = n2\pi$  constructive interference takes place leading to a reduction in the resistance. When  $\phi = n\pi$  destructive interference destroys the correlations and the resistance is unchanged.

This effect is exploited in order to create an Andreev interferometer. This is a SNS junction with  $L_N$  greater than  $\xi_N$  but shorter than  $L_\phi$ . This means that there will be no significant supercurrent through the junction but that an electron with energy less than  $E_{Th}$  reflected from one N/S interface will retain its phase information until it reaches the other. Interference between these electrons will occur based on the phase difference between the two superconducting electrodes,  $\phi = \phi_2 - \phi_1$ . The resistance of the normal metal,  $R$ , is then given as

$$R = R_0 - \gamma(1 + \cos \phi) \quad (4.10)$$

where  $R_0$  is the normal resistance of the metal and  $\gamma$  is an amplitude factor controlled by the properties of the system such as the diffusivity of the normal metal, the numbers of impurities and the quality of the S/N interface.

The first experimental evidence of interference effects in a SNS structure was provided by Petrashov et al in 1993[42]. In this experiment the magneto-resistance of mesoscopic metal rings was measured. Three different configurations were used, as shown in Figure 4.7. In the structures with superconducting islands placed on the current leads (Figure 4.7 (b)) the Aharonov-Bohm oscillations were observed to be 100 times greater than on those without superconductors. On those with superconducting islands placed perpendicular to the current flow (Figure 4.7 (c)) oscillations with pe-

riod  $h/2e$  were observed. This experiment showed that the superconductor clearly had some affect on the magneto-resistance of the sample. The results were limited by the inability to control the phase difference between the two superconductors, meaning the interference occurring was arbitrary.

This situation was improved upon in 1994 in the next experiment by Petrashov et al[43]. In this experiment a mesoscopic ring of normal metal, similar to that used in [42], was connected to a loop of superconductor, as shown in Figure 4.8. By controlling the flux through the loop of superconductor they were able to show that the resistance of the ring oscillated as a function of the phase difference across. They were able to show a similar result when a current was passed through the loop.

Work by Vegvar et al showed similar results[44]. They conducted an experiment in which a Nb-Au-Nb SNS junction was shunted by a series of SIS Josephson junctions, as shown in Figure 4.9. The resistance of the normal section was measured while the phase difference between the two superconducting electrodes were controlled by passing a current through the Josephson junctions. This experiment showed a clear dependence of the resistance on  $\phi$ , with a period of  $2\pi$ .

An experiment by Petrashov et al in 1995 expanded on these results. In this experiment a cross of Ag or Sb connected to a superconducting loop of Al, as shown in Figure 4.10. The resistance of the vertical section of the cross was measured, while the horizontal part formed a SNS junction with the Al. The phase across the junction could be controlled by using a magnetic field to generate flux through the loop, or by passing a current through the loop using two attached superconducting leads. In the ideal case the phase difference due to the magnetic flux  $\Phi_{ext}$  and control current  $I_{ctrl}$  can be expressed as

$$\phi = \frac{2\pi(\Phi_{ext} + I_{ctrl})}{\Phi_0} \quad (4.11)$$

The results produced are shown in Figure 4.11 and were similar to those seen by Vegvar, with oscillations in  $\Delta\phi$  of period  $2\pi$ . For samples with a Sb cross these oscillations were sinusoidal, but those for the Ag cross were significantly different, with cusp-like peaks. An explanation for this was provided by B. J. Van Wees et al. They suggested that for the Ag sample the length of the cross was comparable to  $\xi$ , so that there could be a significant supercurrent through the SNS section. An applied flux would then generate a large screening current around the loop and the total flux would then be given by

$$\Phi_t = \Phi_{ext} - \frac{LI_c}{\Phi_0} \sin\left(\frac{2\pi\Phi_{ext}}{\Phi_0}\right) \quad (4.12)$$



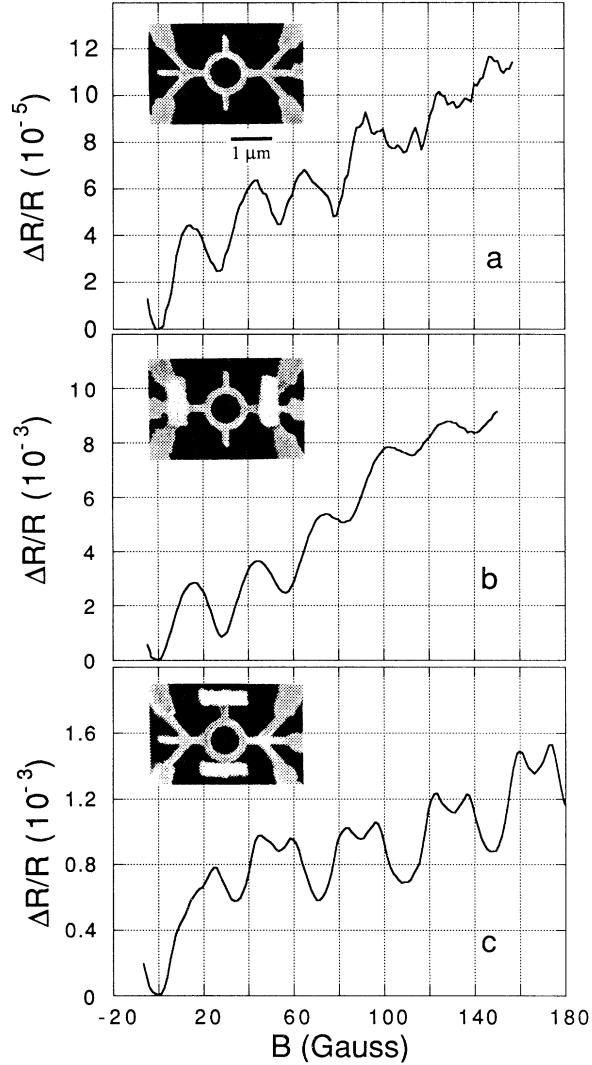
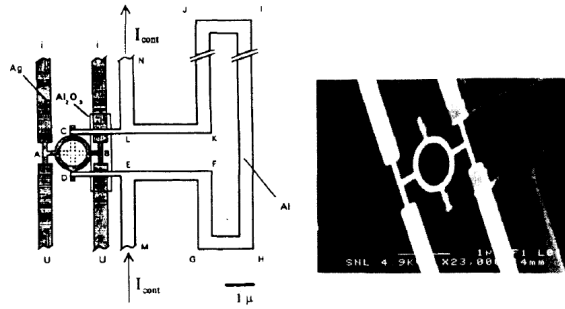
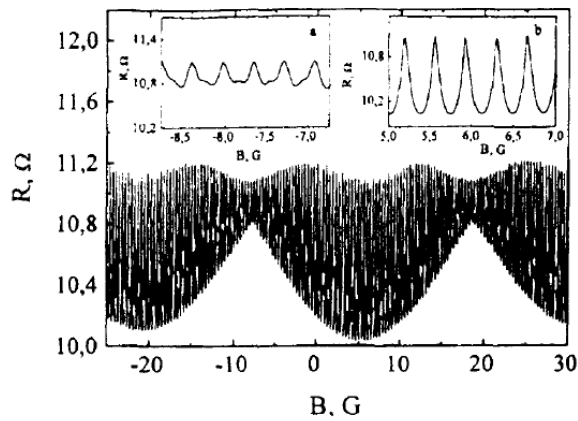


Figure 4.7: Results of experiments by Petrashov et al[42] measuring the magnetoresistance of mesoscopic silver rings. (a) Rings without superconducting mirrors showed the expected  $h/2e$  Aharonov-Bohm oscillations. (b) Rings with superconducting mirrors on the current leads showed 100 times enhanced  $h/2e$  oscillations. (c) Rings with superconducting mirrors perpendicular to the current direction showed  $h/4e$  oscillations.



(a)



(b)

Figure 4.8: (a) Schematic of the sample measured by Petrashov et al in [43]. In this experiment a mesoscopic ring of silver was connected to a loop of aluminium and cooled to 20mK. By controlling the flux through the superconducting loop, they were able to show that the resistance of the ring oscillated as a function of the phase drop across it, as shown in (b).

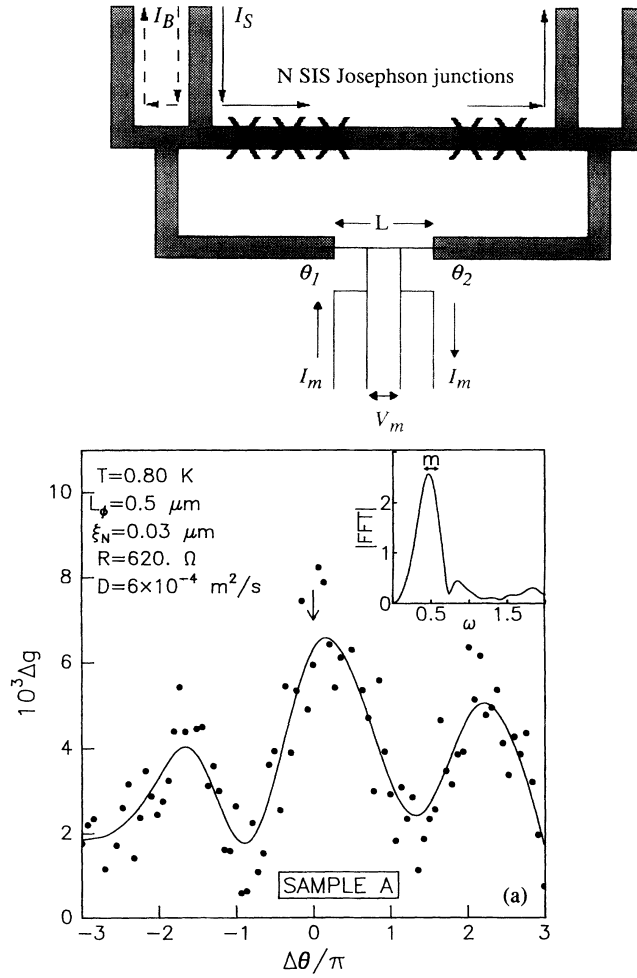


Figure 4.9: Sample measured by Vegvar et al[44]. A Nb-Au-Nb SNS junction is shunted by a series of SIS Josephson junctions. The phase difference across the SNS is controlled using a current passed through the junction. The resistance of the Au section is probed using a four point measurement. The results of this experiment showed oscillations in the conductance of period  $2\pi$ .

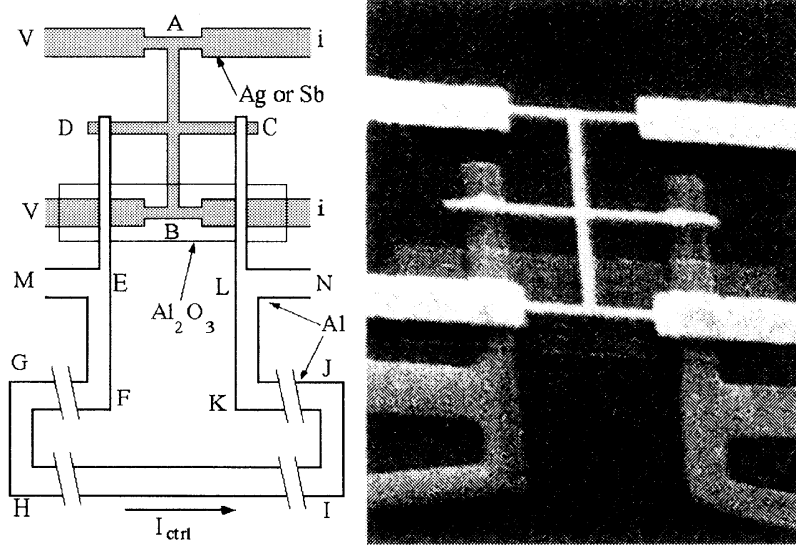


Figure 4.10: The sample measured by Petrashov et al[45]. A mesoscopic cross of Ag or Sb. Attached to this cross at C and D is an Al loop. The resistance of the cross between A and B is probed using a four point measurement. The phase difference between C and D can be controlled by changing the flux through the loop and by passing current through the loop using the attached control leads.

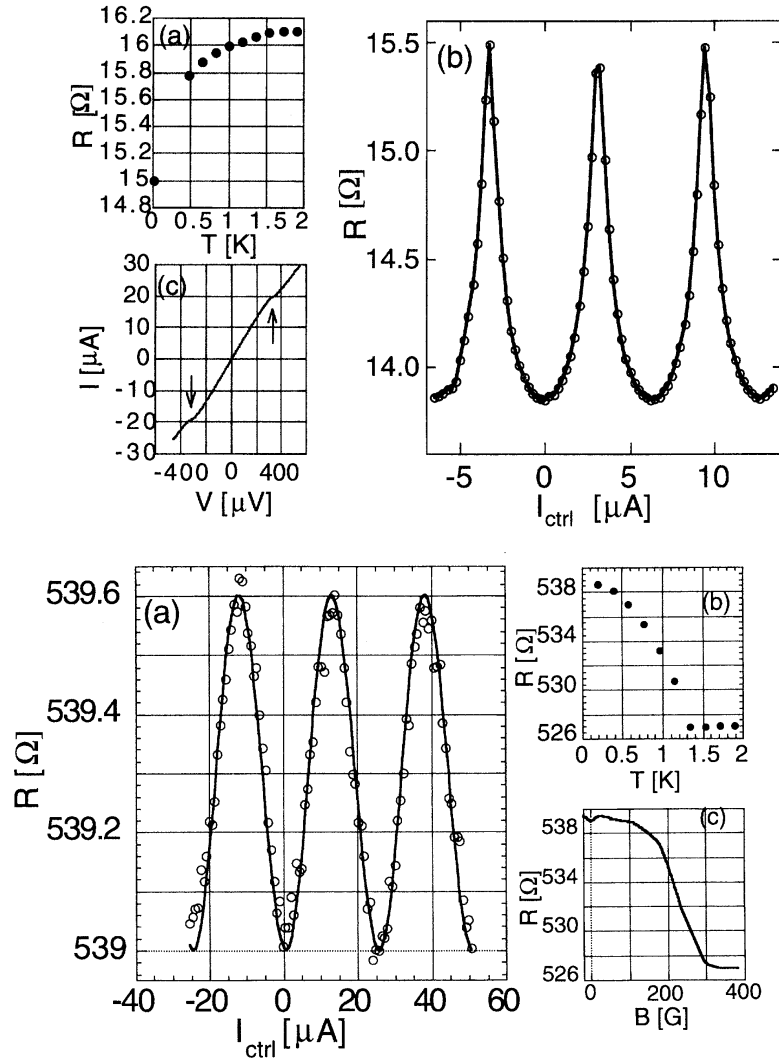


Figure 4.11: Experimental results of Petrashov et al[45]. Samples with both Ag and Sb crosses showed the resistance of the cross oscillating with phase. The oscillations were much larger in the Ag sample, but their shape deviated substantially from the sinusoidal line shape expected. This behaviour was later explained by Nazarov and Stoof[46].

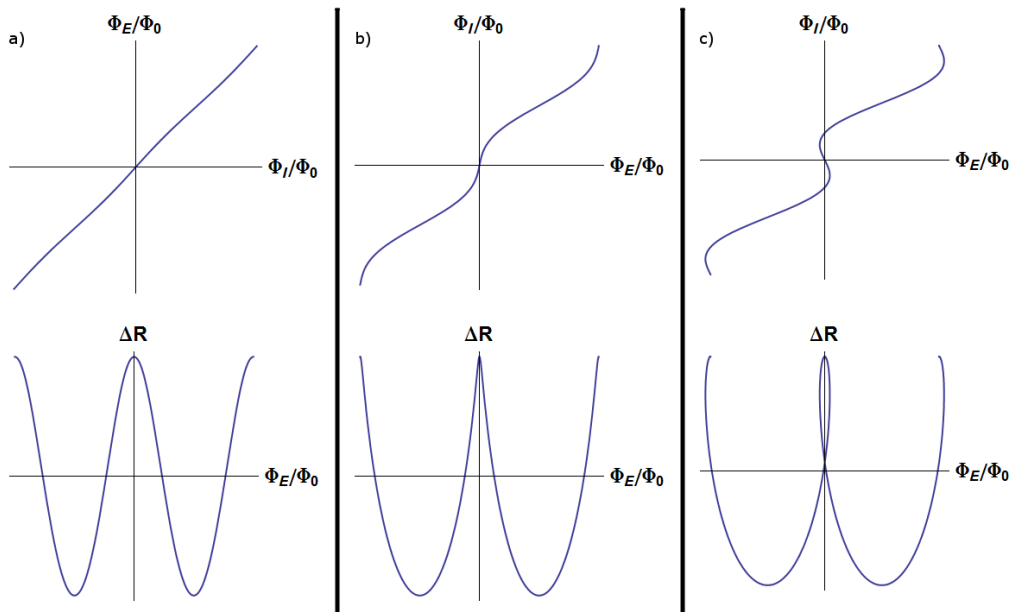


Figure 4.12: Dependence of internal flux  $\Phi_I$  and change in resistance  $\Delta R$  on external flux  $\Phi_E$  for a)  $\alpha = 0.1/2\pi\Phi_0$ , b)  $\alpha = 0.8/2\pi\Phi_0$  and c)  $\alpha = 0.8/2\pi\Phi_0$ . For (a)  $\Phi_I$  dependence and so resistance oscillations are approximately linear. For (b)  $\Phi_I$  dependence becomes strongly non-linear and resistance oscillations show cusp-like behaviour. For (c) both  $\Phi_I$  and  $\Delta R$  become double valued for certain values of  $\Phi_E$ .

Where  $L$  is the inductance of the loop. The response of the system depends on the parameter  $\alpha$ , where  $\alpha = LI_c\Phi_0$ . As  $\alpha$  increases the dependence of  $\Phi_t$  on  $\Phi_{ext}$  becomes increasingly non-linear, resulting in the change in the resistance  $\Delta R$  deviating from a sinusoidal line shape. For  $\alpha > 1/2\pi$ ,  $\Phi_t$  becomes degenerate leading to jumps in  $\Delta R$  and hysteretic behaviour or  $\delta R$ , as shown in Figure 4.12.

The temperature dependence of the resistance change at  $\phi = 0$  was studied and the results are shown in Figure 4.11. These results were put within a theoretical framework by Nazarov and Stoof[46]. They showed that results could be interpreted in terms of the Keldysh Greens function technique [4] and made some further predictions about the behaviour of the system at low temperatures. Until this point, it had been theorized that at zero, or very low temperatures, the penetration of superconductivity into a normal metal

should have no effect on its properties, yet the results of Petrashov showed large amplitude oscillations in this regime. Nazarov and Stoof showed that by considering the affect of superconductivity on the quasi particle diffusion coefficient  $D$ , the theory in fact predicts oscillations at low temperatures, which reach a maximum amplitude when the diffusion coefficient reaches a maximum at energy

$$E^* = \frac{\hbar D}{L^2} = E_{Th} \quad (4.13)$$

i.e. at the Thouless energy. This means that the maximum amplitude of oscillations would be reached at a temperature  $T^*$

$$T^* = \frac{\hbar D}{k_B L^2} \quad (4.14)$$

Below this temperature the amplitude of the oscillations decreases again before reaching zero at zero  $T$ . These predictions were confirmed in a further experiment by Petrashov et al[47].

Courtious et al[36] carried out further experiments on long SNS junctions. Their results mostly reiterated previous experiments, but in more detail showing a clear transition between shorter junctions with  $L < \xi_N$  and junctions with  $\xi_N < L < L_\phi$ . Takayanagi et al then provided a thorough theoretical treatment of these and the other results[48].

## 4.5 Summary

In this chapter the physics of long SNS Josephson junctions have been discussed. In particular, we have described how Andreev reflection allows for the passage of an electron from a normal metal into a superconductor. We have described the experiments showing how this phenomenon can be exploited in order to create Andreev interferometers, devices where the resistance of a piece of normal metal is controlled by the phase difference between two superconducting mirrors. In the next chapter we shall show how an Andreev interferometer can be used as a readout method for a flux qubit and what the consequences of using such a method are.

# Chapter 5

## Readout Methods for Flux Qubits

In the previous chapter the physics of flux qubits and Andreev interferometers have been introduced. This chapter shall examine what happens when these two devices are combined to create a system where the state of a macroscopic quantum system can be controlled and readout. We shall use the physics we have already discussed to create a model of the behaviour we expect to see and discuss the consequences of using such a system on the qubit coherence times. We shall also examine the other methods that have been employed to readout a flux qubit and discuss the advantages and disadvantages of these methods when compared to a flux qubit.

The models used in this chapter were developed by me, based on the work of Dr. Kok Gnee Chua[4] and Dr. Kevin Marshall[3].

### 5.1 Modelling the Behaviour of a Qubit and Interferometer

In this chapter a model of the behaviour of the system will be devised. A simple diagram of a qubit/interferometer system is shown in Figure 5.1. The measurable variable will be the change in resistance of the vertical section of the cross,  $\Delta R_m$ , where

$$R = R_0 - \gamma(1 + \Delta R) \quad (5.1)$$

This variable will change as a function of the external flux,  $\Phi_e$ . The parameters controlling how the system behaves are the ratio of the qubit loop area to the measurement loop area,  $f$ , the ratio of the Josephson energy and charging energy in the qubit junctions,  $E_j/E_c$ , and the energy splitting



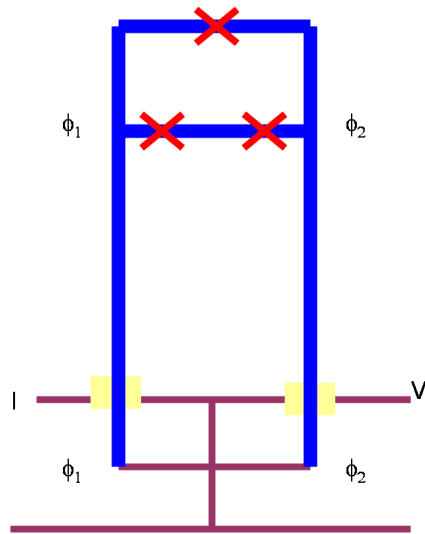


Figure 5.1: A simple schematic of the Andreev interferometer qubit combination system. The qubit is formed of an aluminium loop shown in blue, interrupted by three Josephson junctions, represented as red crosses. Aluminium wires lead from the qubit to the silver Andreev interferometer, shown in purple. The phase difference across the qubit mediates the resistance of the cross, which probed using a simple four point measurement.

of the qubit,  $\Delta$ .

If we take a generic energy spectrum for the qubit

$$E_{\pm}(\Phi_e) = \frac{\varepsilon_q(\Phi_e) + \varepsilon_q(\Phi_e - \Phi_0)}{2} \pm \sqrt{\left(\frac{\varepsilon_q(\Phi_e) - \varepsilon_q(\Phi_e - \Phi_0)}{2}\right)^2 + \Delta^2} \quad (5.2)$$

where  $2\Delta$  is the energy gap at  $\Phi_0/2$ . If  $E_J \gg E_C$  then we can use the 2 junction energy  $\varepsilon = E_J[1 - \cos\pi\frac{\Phi_e}{\Phi_0}]$ . This energy spectrum plotted as a function of  $\Phi_e$  is shown in Figure 5.2 (a).

The phase drop across the qubit is then

$$\phi_{\pm} = \sin^{-1}\left(\frac{I_q}{I_{cq}}\right) \quad (5.3)$$

$$\phi_{\pm} = \sin^{-1}\left(\frac{1}{I_{cq}} \frac{\partial E_{\pm}}{\partial \Phi_e}\right) \quad (5.4)$$

where  $I_q$  is the current flowing around the qubit and  $I_{cq}$  is the critical current of the qubit. Using equation 2.26  $I_{cq}$  can be approximated as

$$I_{cq} = \frac{2eE_j}{\hbar} \quad (5.5)$$

The phase of the qubit as a function of  $\Phi_e$  is shown in Figure 5.2 (b). We must now consider how the qubit interacts with the interferometer. As discussed in the previous chapter, if the resistance of the interferometer is long enough so that the supercurrent through it is small, the resistance of the interferometer is a function of the phase difference between the two superconducting mirrors. In this case, the phase drop is made up of two components, the phase drop from the qubit loop and the phase drop from the measurement loop, so that the resistance change is equal to

$$\Delta R = \cos(\phi_q + \phi_{andreev}) \quad (5.6)$$

$$\Delta R = \cos\left(\phi_q + 2\pi f \frac{\Phi_e}{\Phi_0}\right) \quad (5.7)$$

The change in resistance plotted as a function  $\Phi_E$  is shown in Figure 5.2 (c).

The ratio of the superconducting loops must be chosen so that the difference between the resistance measurements between the ground and excited states is maximized near the  $\Phi_e = \Phi_0/2$ . As Figure 5.4 shows, this is the case when

$$f = n + 0.5 \quad (5.8)$$

where  $n$  is an integer.

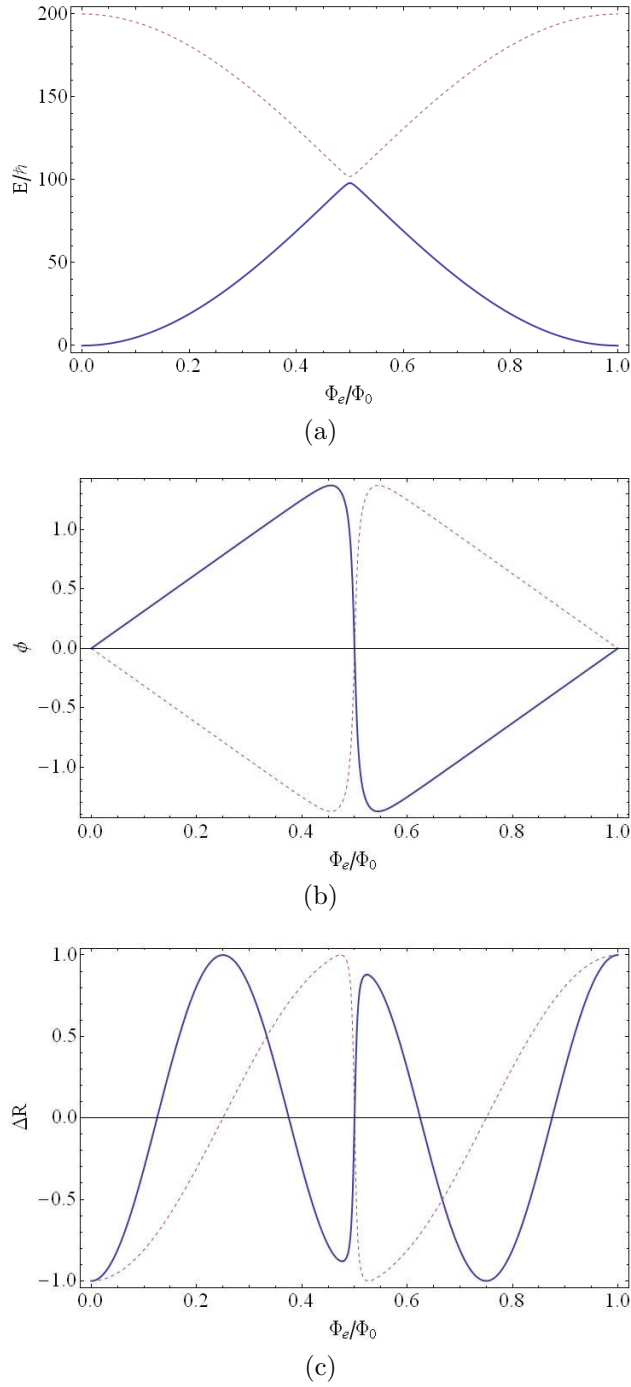


Figure 5.2: a) The energy spectrum,  $E_{\pm}$ , b) Qubit phase,  $\phi_q$ , and c) change in resistance  $\Delta R$  plotted as a function of  $\Phi_e$ . In each case the ground state of the system is shown as a solid line, while the excited state is shown as a dotted line.

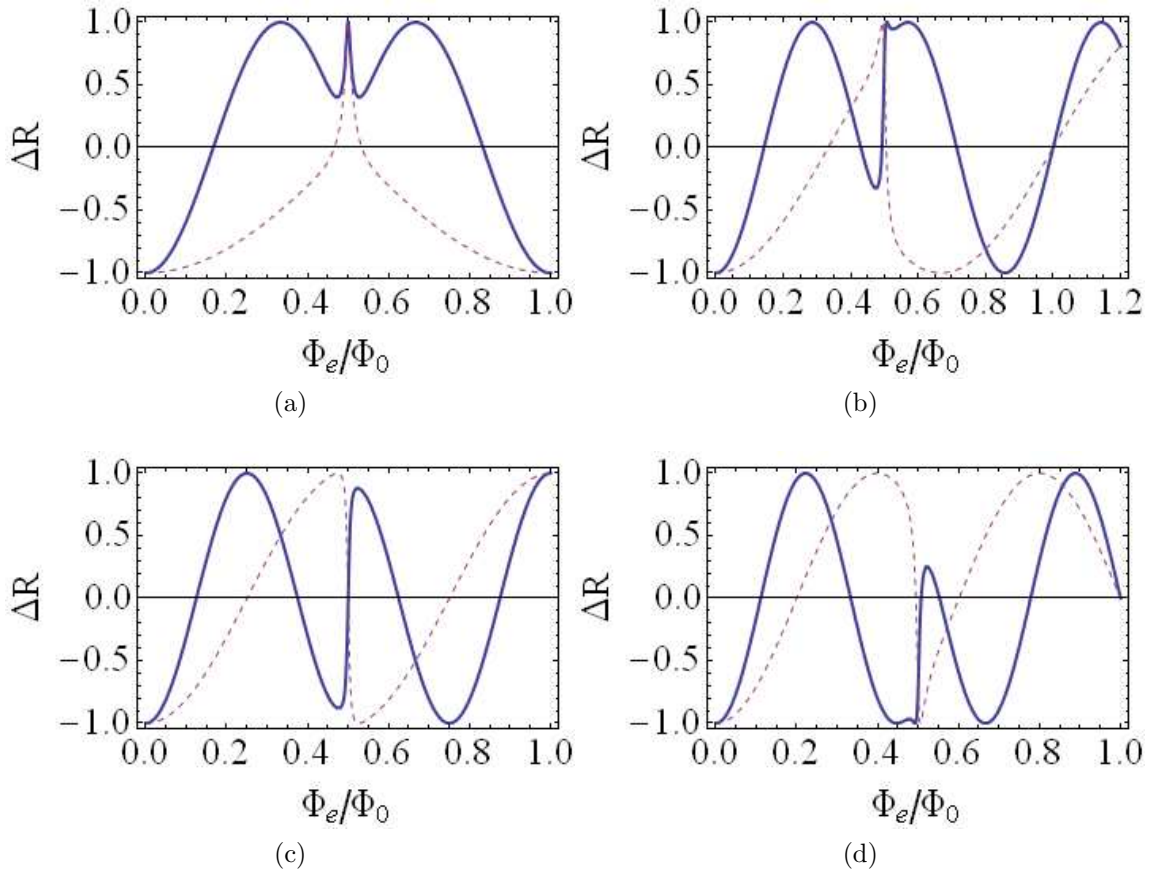


Figure 5.3:  $\Delta R$  for the ground state (shown as a solid line) and the excited state (shown as a dashed line) plotted as function of  $\Phi_e$  for different ratios of qubit area to Andreev loop area. In (a)  $f = 1$ , (b)  $f = 1.25$ , (c)  $f = 1.5$  and (d)  $f = 1.75$ . The difference between the ground and excited states is maximized close to the degeneracy point at  $f = 1.5$ .

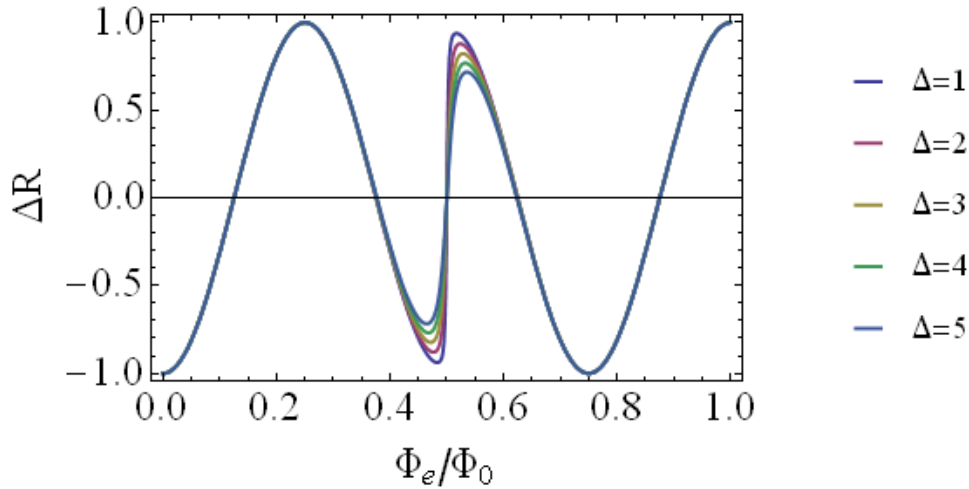


Figure 5.4:  $\Delta R$  plotted as a function of  $\Phi_e$  for values of  $\Delta$  between 1GHz and 5GHz.

## 5.2 Other Readout Methods

This section describes two other methods, DC superconducting quantum interference devices (SQUIDs) and tank circuits, that have been used to readout the state of a flux qubit. It describes the advantages and disadvantages these methods have in comparison to a flux qubit, and details the achievements of other groups who are using these methods.

### 5.2.1 DC Squid Readout Method

One method employed by other groups to read out flux qubits is the DC SQUID. A DC SQUID is a superconducting loop interrupted by two under damped Josephson junctions which acts as a magnetometer. This DC SQUID is inductively coupled to the qubit. This coupling is chosen to give a measurable signal while minimizing the environmental impedance to seen by qubit to lengthen coherence times. The critical current of the SQUID is a function of the flux threading it. By taking repeated IC curves and recording current at which SQUID switches to a voltage state,  $I_{sw}$ , the state of qubit can be inferred.

This process cannot be done as a single shot measurement. The switching current  $I_{sw}$  is not constant, even at fixed flux, due to thermally assisted tunnelling. This means that many readings must be taken at each flux and

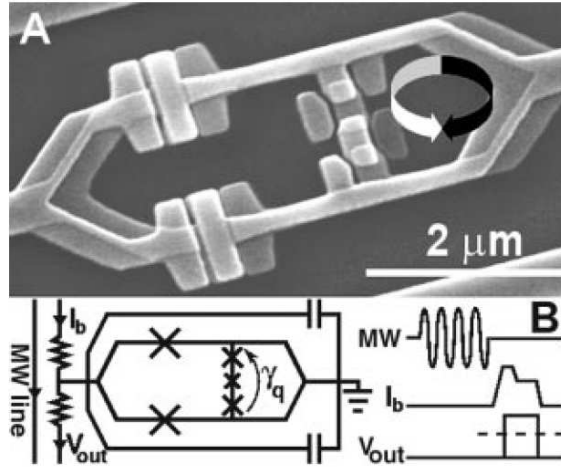


Figure 5.5: SEM image of the SQUID and qubit used by Mooji et al. The SQUID (on the left) has two large Josephson junctions. The qubit (on the right) is made of a loop containing three smaller junctions. Image taken from [17].

an average  $I_{sw}$  calculated.

Professor Mooij and his colleagues working at Delft University have employed this technique with considerable success[17][49]. As shown in Figure 5.5, using a DC SQUID readout coupled to a 3 junction persistent current qubit of the type described in chapter 3, they first mapped out the ground state of the qubit by measuring  $I_{sw}$  at different values of external flux the  $\Phi_E$  and observing a sudden change around  $\Phi_E = \Phi_0/2$ . They then carried out spectroscopy by applying a  $1\mu s$  microwave pulse before each readout. When the frequency of this pulse was equal to the energy level separation at a given flux a peak, or dip, in  $I_{sw}$  was observed. By varying the frequency of the applied radiation and observing the position of these peaks it was possible to map out the energy spectrum for the first two levels of the qubit.

Next measurements in time domain were made. At a fixed flux, a microwave pulse of frequency equal to the energy gap was applied. The length of the pulse determined the probability that the system would be found in the ground or excited state. By varying the length of the pulse it was possible to observe the system under going Rabi oscillations, as shown in Figure 5.6. The frequency of these oscillations were found to be linearly proportional to the amplitude of microwave pulse. As expected, the oscillations took the form of a damped sinusoidal wave. At large pulse times maximum decay

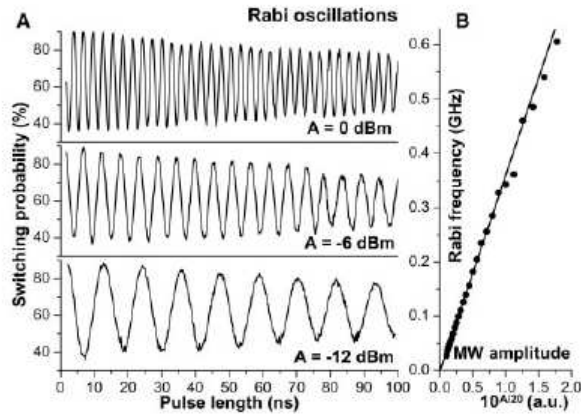


Figure 5.6: Rabi oscillations observed by Mooij et al. The qubit was exposed to a pulse and at a time  $t$  afterwards the DC SQUID was pulsed and the switching current measured. By plotting the probability of switching as a function of  $t$ , it was possible to observe the qubit oscillating between the ground and excited states. The frequency of these oscillations were shown to be a linear function of the RF power. Image taken from [17].

time was  $\tau_{rabi} \approx 150\text{ns}$  was observed.

A  $\pi$  pulse method was then used to relaxation times. A  $\pi$  pulse was applied so that the qubit was fully in the excited state and then time before readout varied. Using the method the relaxation time found to be  $\tau_{relax} = 900\text{ns}$ .

Mooji then went on to measure two coupled flux qubits[50]. The SEM image of the sample measured is shown in Figure 5.7. Two flux qubits were fabricated so that one side was common to both of them and they were inductively coupled. By carrying out spectroscopy on the system as described above, they were able to show that the coupled qubits formed a quantum mechanical four state system. They then went on to show that this work can be extended to create a C-NOT logic gate using a two coupled flux qubits[51]. C-Not logic gates are the building blocks of a quantum computer.

## 5.2.2 Tank Circuit Readout Method

Another method of reading out flux qubits has been devised by Prof. Il'ichev working at Universität Erlangen-Nrnberg. In this method, a tank circuit with inductance  $L_T$  and quality factor  $Q$  coupled to qubit by mutual inductance  $M$ . The tank circuit is driven by DC bias current  $I_{dc}$  and AC current  $I_{RF}$ .

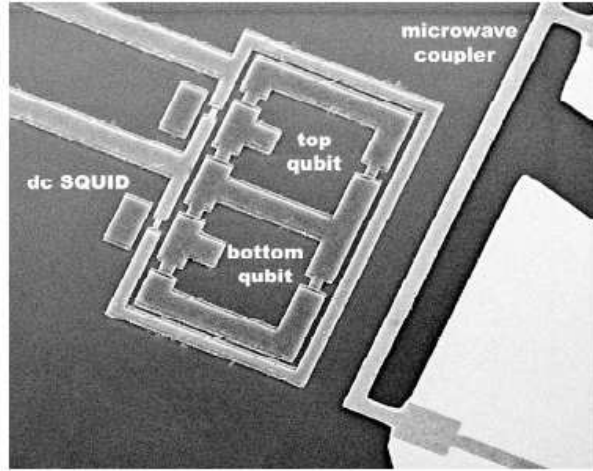


Figure 5.7: The two couple qubits measured by Mooij et al. The two qubits each are  $5\mu\text{m}$  wide, have three Josephson junctions, and share one common side. They are surrounded by a large DC SQUID. Image taken from [50].

The flux through qubit is  $\Phi_e = \Phi_{dc} + \Phi_{RF}$ . The amplitude of  $\Phi_{RF}$  is small so that  $\Phi_e \cong \Phi_{dc}$ . By measuring the effective impedance of the circuit as a function of  $\Phi_e$ , the properties of qubit can be determined. The imaginary part of the total impedance can be expressed as a phase angle between driving current  $I_{rf}$  and tank voltage

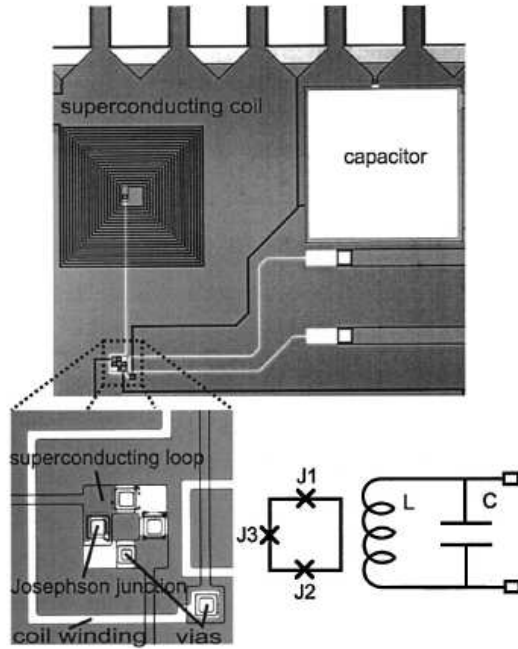
$$\tan\alpha = k^2Q \frac{\beta i'(\Phi)}{1 + \beta i'(\Phi)} \quad (5.9)$$

where  $i(\phi) = I(\phi)/I_c$ , the normalised supercurrent.  $i'(\Phi)$  is the derivative of this with respect to the magnetic flux,  $\Phi = \Phi_e - \beta i(\Phi)$ , through it. The term  $\beta = 2\pi LI_c/\Phi_0$ .  $\alpha$  and  $k^2Q$  are measurable and the rest of the terms are known so that by measuring the  $\alpha$  the supercurrent  $i(\Phi_e)$  can be reconstructed.

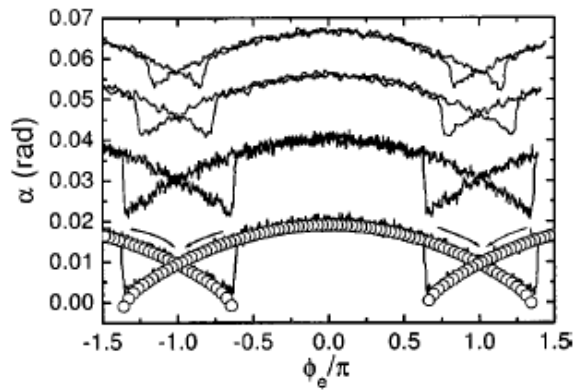
In their first experiment, Ilichev et al tested a circuit with large Josephson junctions so that inter well tunnelling was suppressed and the system behaved classically. As expected, hysteresis was observed, as shown in Figure 5.8.

A tank circuit was then used for the continuous measurements of Rabi oscillations in qubit with smaller junctions[2]. Rabi oscillations lead to a rapid change in the magnetic moment of the qubit as the qubit flips between the ground and excited state. If the frequency of oscillations is close to the resonance frequency of the tank a response can be observed in the spec-





(a)



(b)

Figure 5.8: (a) The tank circuit readout design used by Il'ichev et al. In this design a 3 Josephson junction is coupled to a high quality tank circuit. The behaviour of the qubit is probed by observing changes in impedance of the tank circuit. Results obtained from a qubit with large Josephson junctions. The system can be seen behaving classically with two metastable states. Image taken from [52].

tral density of tank voltage, as shown in Figure 5.9. As expected, a linear dependence of the Rabi frequency on microwave amplitude was observed.

This method was then used to investigate two coupled flux qubits[53], with the two qubits again read out by a large high quality tank circuit. In this experiment the qubits were coupled by a single shared large Josephson junction. This avoided the problem of a small inductive coupling between the two qubits because of their small areas, and allowed the magnitude of the coupling to be controlled by engineering the size of the Josephson junction.

### 5.2.3 Non-Linear Oscillator Readout Method

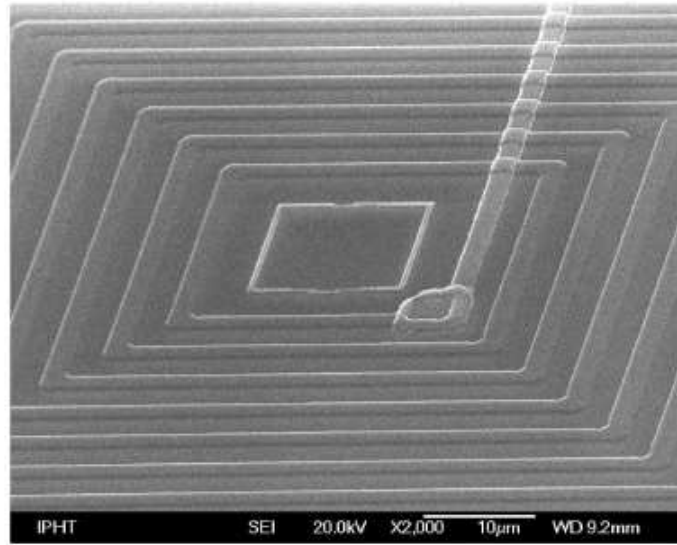
The most successful measurements on a flux qubit to date have been made using non-linear oscillators[54][55][56][57][58]. In previous SQUID measurements the qubit is strongly disturbed when the SQUID switches to a voltage state. Dispersive readouts such as those discussed in the section above overcome this problem by coupling the qubit to a linear oscillator and observing the change in the resonant frequency. However, in these systems the time needed to properly measure the impedance are close to the relaxation time of the qubit, limiting their effectiveness.

In a non-linear oscillator readout, the qubit is coupled to an oscillator formed from a DC SQUID and a capacitance. The hysteretic behaviour of the SQUID means that the qubit state can be probed for a very short time and then the impedance of the system measured over a much longer time, allowing for high contrast measurements, as shown in Figure 5.10.

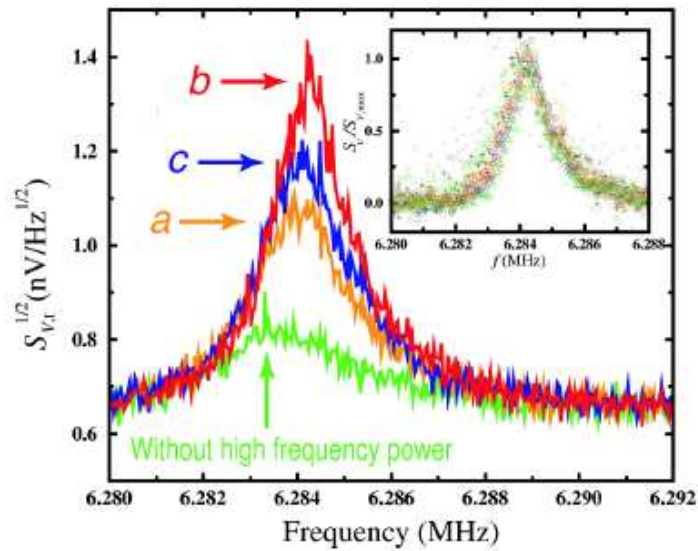
### 5.2.4 Comparison of Other Readouts to Andreev Interferometer

As described above, projects that investigate the properties of flux using other readout methods are already quite advanced, now mostly focusing on coupling two or more qubits. However, it is believed that the Andreev interferometer would have some advantages over these methods. They both involve taking a large number of measurements and using statistical methods to infer the state of the qubit from these results. The Andreev interferometer promises to allow continuous monitoring of the state of the qubit, making spectroscopy quicker and simpler. The design used in this project also allows for each qubit to have its own individual readout, as opposed to a SQUID or tank circuit which must surround and be coupled to a large number of qubits.

There are some disadvantages to using an Andreev interferometer. The direct connection of a normal metal wire to the flux qubit leads to low envi-



(a)



(b)

Figure 5.9: (a) Shows a SEM image of the qubit and superconducting coil used by Il'ichev et al. (b) Shows the continuous observation of Rabi oscillations made by Il'ichev in this experiment. The coupling of the qubit to the tank lead to a change in the resonant frequency of the tank circuit when the qubit underwent resonant excitation. The magnitude of this change was dependent on the RF power, showing that the frequency of the Rabi oscillations were dependent on RF power. Images taken from [2].

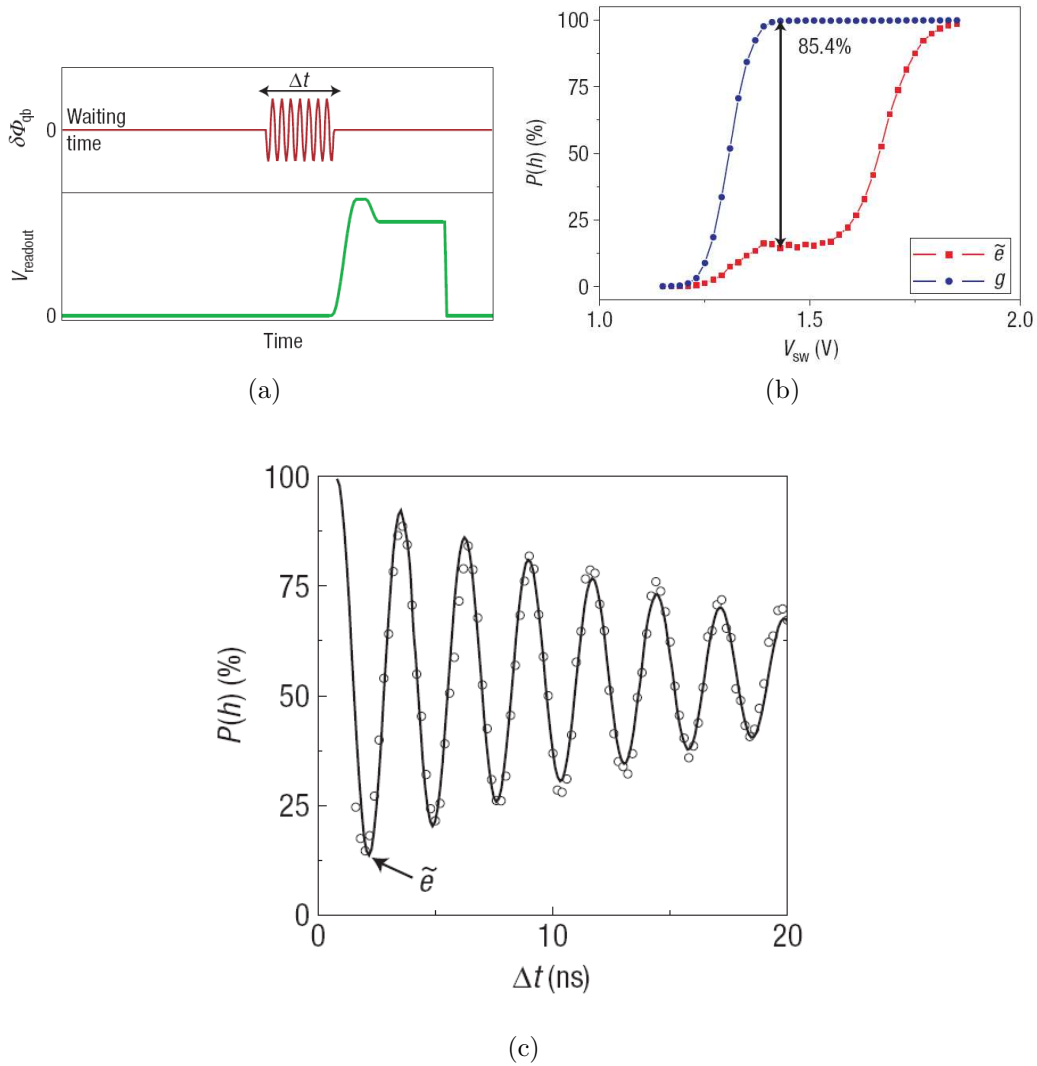


Figure 5.10: (a) Measurement scheme used in non-linear oscillator experiments of [57]. First the qubit is excited by a short pulse of RF. Then a pulse of voltage is applied to the oscillator, coupling it to the qubit to probe the state of the qubit. The voltage applied to the oscillator is then lowered, latching it and allowing its state to be readout with a high degree of accuracy. (b) Switching probability of the oscillator as a function of the amplitude of the voltage probe. This shows that by controlling the voltage, a high level of contrast between the ground and excited states can be obtained. (c) Switching probability as a function of RF pulse length. This shows the qubit undergoing exponentially damped Rabi oscillations. Images taken from [57].

ronmental impedance, short relaxation and therefore short coherence times. In other methods environmental impedance can be increased by engineering the coupling of the readout to the qubit. Johnson–Nyquist noise from the normal wire could also affect the coherence of the qubit, leading to shortened dephasing times.

# Chapter 6

## Decoherence

One of the major challenges when working with solid state qubits is overcoming the short coherence times of the systems caused by their many degrees of freedom[59]. In this section we will discuss the sources of noise in a flux qubit system and attempt to estimate the decoherence rates associated with them.

The sources of the noise in the system can be split into two groups. The first is circuit noise coming from the electronic circuits which we have deliberately coupled to the qubit in order to manipulate it and read it out. The nature of this noise is well understood and our analysis will, therefore, concentrate on describing how it effects our particular qubit with its novel Andreev inteferometer readout.

The second type of noise is macroscopic and microscopic. Microscopic noise includes charge fluctuations[60] and barrier defect fluctuations[61][62]. Macroscopic noise consists of a  $1/f$  flux noise[61]. The origins and characters of these noise sources are less understood and more difficult to characterise.

### 6.1 Dephasing and Relaxation

In chapter 3 we showed that the dynamics of the qubit could be described by a vector which ended on the Bloch sphere. This vector rotates about the z-axis at the Larmor frequency while resonant excitation of the qubit causes a rotation about the x-y plane. Modulation of the Larmor frequency leads to an uncertainty in the qubit phase  $\phi$ , referred to as pure dephasing. By absorbing or emitting a photon into the environment, the qubit can be excited to or relaxed from the ground state, leading to a change in  $\theta$ .

Using the Bloch-Redfield approximation we can relate the noise power spectral density to the transverse ( $\phi$ ) and longitudinal ( $\theta$ ) degrees of freedom

of the qubit. The average longitudinal energy relaxation rate is written as  $\Gamma_1$ . This is related to the noise power spectral density by  $S_{\delta\nu\perp}(\nu)$ . Using Fermi's golden rule we can write

$$\Gamma_1 = T^{-1} = \Gamma_r + \Gamma_{ex} \quad (6.1)$$

$$(6.2)$$

Since the qubit is operated at temperatures where  $k_B T \ll h\nu$  the excitation rate is negligible and we can write

$$\Gamma_1 = \Gamma_r = \pi S_{\delta\nu\perp}(\nu) \quad (6.3)$$

The average transverse dephasing rate,  $\Gamma_2$  is written as

$$\Gamma_2 = \Gamma_\phi + \frac{1}{2}\Gamma_1 \quad (6.4)$$

Here  $\Gamma_\phi$  is the pure dephasing which can be written as

$$\Gamma_\phi = \lim_{f \rightarrow 0} \pi S_{\delta\nu\parallel}(f) \quad (6.5)$$

In this dissertation we will use the descriptions of the relaxation and dephasing times derived by Grifoni et al.[63], which are shown below

$$\Gamma_r = \tau_r^{-1} = \frac{1}{2} \left( \frac{\Delta}{\nu} \right)^2 J(\nu/\hbar) \coth \frac{\nu}{2k_B T} \quad (6.6)$$

$$\Gamma_\phi = \tau_\phi^{-1} = \frac{\Gamma_r}{2} + \left( \frac{\epsilon}{\nu} \right)^2 \alpha 2\pi \frac{k_B T}{\hbar} \quad (6.7)$$

$$\alpha = \lim_{\omega \rightarrow 0} \frac{J(\omega)}{2\pi\omega} \quad (6.8)$$

$$\approx \frac{1}{2\pi} \frac{\delta J(\omega)}{\delta \omega} \quad (6.9)$$

where  $\epsilon = 2I_p(\Phi_q - 1/2\Phi_0)$  and  $\nu = \sqrt{\Delta^2 + \nu^2}$  and  $J(\omega)$  is environmental spectral density.

As equations 6.7 and 6.8 show, relaxation is caused by environmental noise at the resonant frequency of the system while dephasing is caused by environmental noise at low frequencies.

## 6.2 Sources of Circuit Noise in Qubit/Interferometer System

There are four main sources of circuit noise in our system. These are-

1. Johnson-Nyquist noise in the Andreev interferometer and measurement leads.
2. Johnson-Nyquist noise from the antenna.
3. Johnson-Nyquist noise from the magnet.
4. Noise from the measurement electronics.

Using the methods developed by Van der Wal[64], I can calculate a relaxation and dephasing rate for each of these sources. To do this it is necessary to know how a change in the current,  $\delta I$ , of any of these elements is linked to the qubit energy splitting  $\epsilon$ . Imagine an element which is coupled to the qubit by mutual inductance  $M$ . A change in current in this element will then result in a change in flux through the qubit  $\Phi_q$

$$\delta\Phi_q = M\delta I \quad (6.10)$$

Using 3.18 we can then write

$$\delta\epsilon = 2I\delta\Phi_q \quad (6.11)$$

$$= 2I_p M\delta I \quad (6.12)$$

### 6.2.1 Relaxation and Dephasing Due to Andreev Interferometer

#### Noise from interferometer

Figure 6.1 shows a schematic representation of the Qubit and Andreev Interferometer. In this representation the qubit is modelled as a single Josephson junction with critical current  $I_{cq}$  and the interferometer is modelled as a Josephson junction with critical current  $I_{ca}$  shunted by resistance  $R_a$  and capacitance  $C$ . The three elements that make up the Andreev interferometer combine to form total impedance  $Z(\omega)$ . The Johnson-Nyquist noise across this impedance results in a current  $\delta I_q$  flowing through the qubit, leading to fluctuations in the qubit energy and decoherence. This Johnson-Nyquist noise has a power spectrum described by



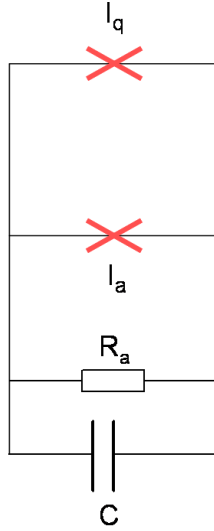


Figure 6.1: Schematic representation of the qubit and Andreev interferometer. The qubit is represented as a single Josephson junction with critical current  $I_{cq}$ . The Andreev interferometer is represented by a Josephson junction, resistor and capacitance connected in parallel.

$$\langle \delta V \delta V \rangle_w = \hbar \omega \operatorname{Re}(Z(\omega)) \coth \left( \frac{\hbar \omega}{2k_B T} \right) \quad (6.13)$$

Using 2.3, the current through the qubit can be written as

$$I_q = I_{cq} \sin \gamma_q \quad (6.14)$$

$$= I_{cq} \sin(\phi_{ext} + M_1 \phi_{int}) = I_{cq} (\sin \phi_{ext} \cos M_1 \phi_{int} - \cos \phi_{ext} \sin M_1 \phi_{int}) \quad (6.15)$$

where  $\phi_{ext}$  is the phase drop across the junctions due to the voltage fluctuations in  $Z(\omega)$ ,  $\phi_{int}$  is the phase drop across both junctions due to the magnetic flux threading the loop. Here  $M_1$  is defined as

$$M_1 = \frac{I_{cq}}{I_{cq} + I_{ca}} \quad (6.16)$$

meaning that the  $\phi_{int}$  is related to the flux through the loop by

$$\phi_{int} = 2\pi M_1 \Phi \quad (6.17)$$

To describe the voltage fluctuations we can write

$$\frac{dI_q}{dt} = i\omega I_q = I_{cq} (\cos\bar{\phi}_{ext} \cos M_1 \phi_{int} - \sin\bar{\phi}_{ext} \sin M_1 \phi_{int}) \frac{d\phi_{ext}}{dt} \quad (6.18)$$

where  $\bar{\phi}_{ext}$  is the time average of  $\phi_{ext}$ . Since this should equal zero we can rewrite 6.18. Substituting using the Josephson voltage relationship 2.3

$$i\omega I_q = I_{cq} \cos M_1 \phi_{int} \frac{\delta\phi_{ext}}{\delta t} \quad (6.19)$$

$$= \frac{1}{\Phi_0} I_{cq} \cos(M_1 \phi_{int}) V \quad (6.20)$$

We can now link this to the qubit energy using 6.11

$$\delta I = \frac{1}{i\omega\Phi_0} I_{cq} \cos(M_1 \phi_{int}) \delta V \quad (6.21)$$

$$\delta\epsilon = 2I_p M \frac{1}{i\omega\Phi_0} I_{cq} \cos(M_1 \phi_{int}) \delta V \quad (6.22)$$

We can, therefore, write the power spectrum of the qubit energy fluctuations as

$$\langle \delta\epsilon \delta\epsilon \rangle_\omega = \left( \frac{2I_p M}{\Phi_0 \omega} \right) I_{cq}^2 \cos^2(M_1 \phi_{int}) \langle \delta V \delta V \rangle_\omega \quad (6.23)$$

$$= \hbar\omega \left( \frac{2I_p M}{\Phi_0 \omega} \right) I_{cq}^2 \cos^2(M_1 \phi_{int}) \text{Re}(Z(\omega)) \coth\left(\frac{\hbar\omega}{2k_B T}\right) \quad (6.24)$$

resulting in a spectral density

$$J(\omega) = \frac{4I_p^2 M^2 I_{cq}^2}{\Phi_0^2 \hbar\omega} \cos^2(M_1 \phi_{int}) \text{Re}(Z(\omega)) \quad (6.25)$$

### Impedance of Interferometer

The impedance of the interferometer is formed from an inductance in parallel with a resistance and a capacitance. This leads to a total inductance

$$Z(\omega) = \left( \frac{1}{i\omega L_a} + \frac{1}{i\omega C} + \frac{1}{R} \right)^{-1} \quad (6.26)$$

here  $L$  is the inductance of the interferometer which can be written as

$$L = \frac{\hbar}{2eI_{ca}\cos(M_2\phi_{int}nt)} \quad (6.27)$$

where

$$M_2 = \frac{I_{ca}}{I_{ca} + I_{cq}} \quad (6.28)$$

This combination can be treated as a LC oscillator with resonant frequency

$$\omega_{LC} = 1/\sqrt{L_a C} \quad (6.29)$$

For  $\omega \ll \omega_{LC}$  this simplifies to

$$Z(\omega) \approx \frac{\omega^2 L_a^2}{R} \quad (6.30)$$

and for  $\omega \gg \omega_{LC}$  this simplifies to

$$Z(\omega) \approx \frac{1}{\omega^2 C^2 R} \quad (6.31)$$

## Relaxation and Dephasing Rates

Using the inductances from the above section with 6.7 and 6.8 we can now calculate the relaxation and dephasing rates due to noise from the interferometer.

$$\Gamma_{ra} = \left(\frac{\Delta/\hbar}{\omega_{res}}\right) \frac{4I_p^2 M^2 I_c q^2}{\Phi_0^2 \hbar \omega_{res}} \cos^2\left(M\phi_{int} \frac{1}{\omega^2 C^2 R}\right) \coth\left(\frac{\hbar \omega_{res}}{2k_B T}\right) \quad (6.32)$$

$$\Gamma_{\phi a} = \frac{\Gamma_{ra}}{2} + \left(\frac{\epsilon}{\hbar \omega}\right)^2 \frac{8\pi I_p^2 M^2}{\hbar \Phi_0^2} I_{cq}^2 \cos^2(M_1\phi_{int}) \frac{L^2 k_B T}{R \hbar} \quad (6.33)$$

Therefore, the dephasing rate can be written as

$$\Gamma_{\phi a} = \frac{\Gamma_{ra}}{2} + \left(\frac{\epsilon}{\hbar \omega}\right)^2 \frac{8\pi I_p^2 M^2}{\hbar} \left(\frac{I_{cq}}{I_{ca}}\right)^2 \frac{\cos^2(M_1\phi_{int})}{\cos^2(M_2\phi_{int})} \frac{1}{R} \frac{k_B T}{\hbar} \quad (6.34)$$

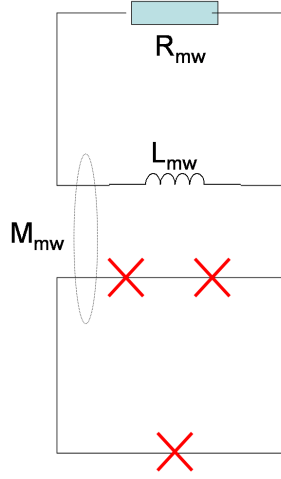


Figure 6.2: Schematic representation of the qubit and antenna.

## 6.2.2 Relaxation and Dephasing Due to Microwave Antenna

Another source of decoherence in the system is the superconducting antenna used to excite the qubit. The relaxation and dephasing rates due to the antenna can be calculated using a similar method to that used in the previous section. As shown in Figure 6.2, this is formed by an inductance of inductance  $L_{mw}$  shunted by resistance  $R$  coupled to qubit by mutual inductance  $M_{mw}$ . The shunting resistance  $R$  is assumed to be the  $50\Omega$  impedance of the coaxial cable.

The current noise in the antenna is related to the voltage noise by

$$\delta I_{mw} = \frac{1}{i\omega L_{mw}} \delta V \quad (6.35)$$

from 6.10 and 6.11 this gives

$$\delta \epsilon = 2I_p M \frac{1}{i\omega L_{mw}} \delta V \quad (6.36)$$

Substituting from 6.13

$$\langle \delta \epsilon \delta \epsilon \rangle_\omega = \frac{4\hbar}{\omega} \left( \frac{I_p^2 M_{mw}}{L_{mw}} \right)^2 \text{Re}(Z(\omega)) \coth \left( \frac{\hbar\omega}{2k_B T} \right) \quad (6.37)$$

$$\langle \delta\epsilon\delta\epsilon \rangle_\omega = \frac{4}{\hbar\omega} \left( \frac{I_p^2 M_{mw}}{L_{mw}} \right)^2 \text{Re}(Z(\omega)) \quad (6.38)$$

The real part of the impedance of the system is equal to

$$\text{Re}Z(\omega) = \frac{\omega^2 L_{mw}^2 R_{mw}^2}{R_{mw} + \omega^2 L_{mw}^2} \quad (6.39)$$

$$\approx \frac{\omega^2 L_{mw}^2}{R_{mw}} \quad (6.40)$$

Combining with 6.38

$$J(\omega) = \frac{4\omega}{\hbar} \frac{(M_{mw} I_p)^2}{R_{mw}} \quad (6.41)$$

and

$$\alpha = \frac{2}{\pi\hbar} \frac{(M_{mw} I_p)^2}{R_{mw}} \quad (6.42)$$

So the relaxation rate due to noise from the antenna is equal to

$$\Gamma_{rmw} = 2 \frac{\Delta^2}{\hbar^3 \omega} \frac{M_{mw}^2 I_p^2}{R_{mw}} \coth \frac{\hbar\omega}{2k_B T} \quad (6.43)$$

and, assuming the qubit is operated near  $\epsilon = \nu$ , the dephasing rate is

$$\Gamma_{\phi mw} = \frac{\Gamma_{rmw}}{2} + \frac{4M_{mw}^2 I_p^2}{\hbar R} k_B T \quad (6.44)$$

### 6.2.3 Relaxation and Dephasing Due to Solenoid

The noise from the superconducting solenoid can be calculated using the same method as the microwave antenna. In this case we have a solenoid of inductance  $L_{sol}$  coupled to qubit by mutual inductance  $M_{sol}$ . The solenoid is in parallel with two resistances,  $R_{sol}$ , the measurement leads and source, and  $R_{shunt}$ , the shunting resistance. Since  $R_{shunt} \ll R_{sol}$  total resistance  $R_T \approx R_{shunt}$ .

### 6.2.4 Estimates of Relaxation and Dephasing Times for Our System

The relaxation rate and dephasing rate of the qubit due to its interaction with the Andreev interferometer can be written as

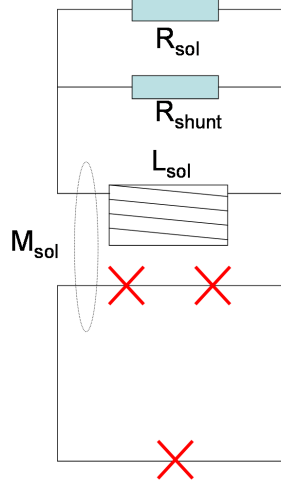


Figure 6.3: Schematic representation of the qubit and solenoid.

$$\Gamma_{ra} = \left( \frac{\Delta/\hbar}{\omega_{res}} \right) \frac{4I_p^2 M^2 I_c q^2}{\Phi_0^2 \hbar \omega_{res}} \cos^2(M_1 \phi_{int}) \frac{1}{\omega^2 C^2 R} \coth \left( \frac{\hbar \omega_{res}}{2k_B T} \right) \quad (6.45)$$

$$\Gamma_{\phi a} = \frac{\Gamma_{ra}}{2} + \left( \frac{\epsilon}{\hbar \omega} \right)^2 \frac{8\pi I_p^2 M^2}{\hbar} \left( \frac{I_{cq}}{I_{ca}} \right)^2 \frac{\cos^2(M_1 \phi_{int})}{\cos^2(M_2 \phi_{int})} \frac{1}{R} \frac{k_B T}{\hbar} \quad (6.46)$$

where  $I_{cq}$  and  $I_{ca}$  are the critical currents of the qubit and interferometer respectively,  $R$  is the normal resistance of the interferometer, and  $C$  is the capacitance shunting the interferometer.  $\phi_{int}$  is the phase drop across the qubit and interferometer due to the flux threading the loop. This can be written as  $\phi_{int} = 2\pi f \Phi_q / \Phi_0$ . Where  $\Phi_q$  is the flux through the qubit (approximately  $0.5\Phi_0$  for qubit operations) and  $f$  is the ratio of the area of the loop to the qubit area.

The relaxation and dephasing due to the qubit interaction with the solenoid and antenna can both be described by the same formulas, given below-

$$\Gamma_r = 2 \frac{\Delta^2}{\hbar^3 \omega} \frac{M_{mw}^2 I_p^2}{R_{mw}} \coth \frac{\hbar \omega}{2k_B T} \quad (6.47)$$

$$\Gamma_\phi = \frac{\Gamma_r}{2} + \frac{4M_{mw}^2 I_p^2}{\hbar R} k_B T \quad (6.48)$$

	Parameters	M	$\Gamma_r^{-1}$	$\Gamma_\phi^{-1}$
Inteferometer	$I_{cq} = 1\mu\text{A}$ $I_{ca} = 0.1\mu\text{A}$ $R = 10\Omega$ $C = 10\text{nF}$ $T = 20\text{mK}$	10pH	$200\mu\text{s}$	0.2ns
Antenna	$R = 50\Omega$ $T = 20\text{mK}$	1pH	300ns	30ns
Solenoid	$R = 1\Omega$ $T = 4.2\text{K}$	0.1pH	5ns	10ns

Table 6.1: Estimated contributions to the relaxation and dephasing time of the qubit from the interferometer, antenna and solenoid.

The table below gives the estimated relaxation and dephasing times for each of these elements.

The values of  $M_{mw}$  and  $M_{sol}$  were measured experimentally by observing the change in resistance of the interferometer. The estimates of  $I_{cq}$  and  $I_{ca}$  were based on the work of [4] [65]. The value of  $M_a$  is more difficult to estimate. For these calculations a ‘worst case scenario’ has been assumed, where the coupling of the Andreev interferometer to the qubit is 100 times greater than that of the solenoid.

### 6.3 Modelling Spectroscopy

Using the model described in the previous chapters I can show how the resistance oscillations as a function of flux will change when we apply a RF field to resonantly excite the qubit. To do this I have used the Lorentzian line shape of resonance peaks described by

$$P_+ = \frac{\omega_{rabi}}{\omega_{rabi} + (\omega_q - \omega_{RF})\frac{\Gamma_\phi}{\Gamma_r} + \sqrt{\Gamma_r\Gamma_\phi}} \quad (6.49)$$

where  $\omega_q$  is defined as

$$\omega_q\Phi_e = \frac{E_+ - E_-}{\hbar} \quad (6.50)$$

Since the system only has two states and must at all times be in one of them, we can write

$$P_- = 1 - P_+ \quad (6.51)$$

Using this fact a new current,  $I_T$ , can be calculated which is the current flowing around the qubit under the influence of a perturbation

$$I_T = P_+ I_+ + P_- I_- \quad (6.52)$$

Using the method described in section 5.1 we can write

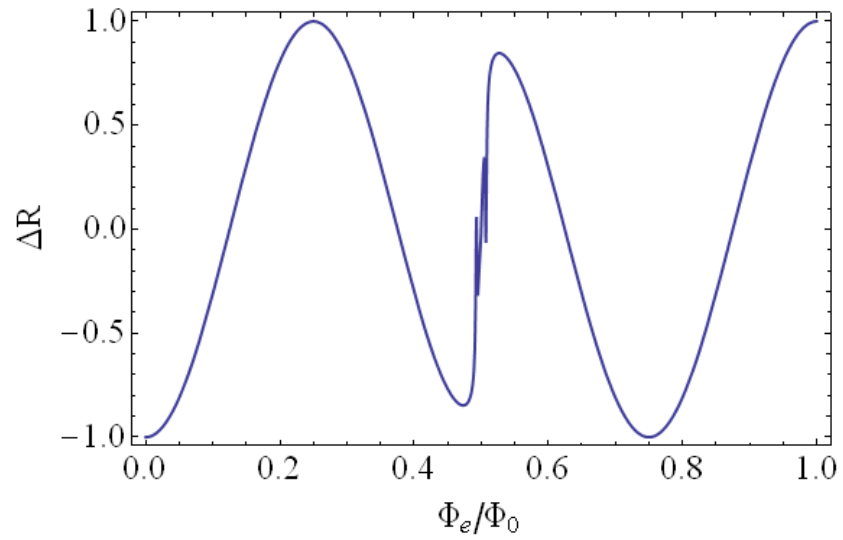
$$\Delta R_T = \text{Cos} \left[ \sin^{-1} \left( \frac{I_T}{I_{cq}} \right) + 2\pi f \frac{\Phi_e}{\phi_0} \right] \quad (6.53)$$

For our modelling we have chosen a constant decoherence rate  $\Gamma = \sqrt{\Gamma_r \Gamma_\phi}$ . The above section shows that the decoherence due to circuit noise is a function of the qubit current and therefore the flux, so assuming a constant decoherence rate is an approximation. However, there will be a constant term in the decoherence rate due to the charge noise and we believe that this approximation should give us a good estimate of the upper limit of the coherence times.

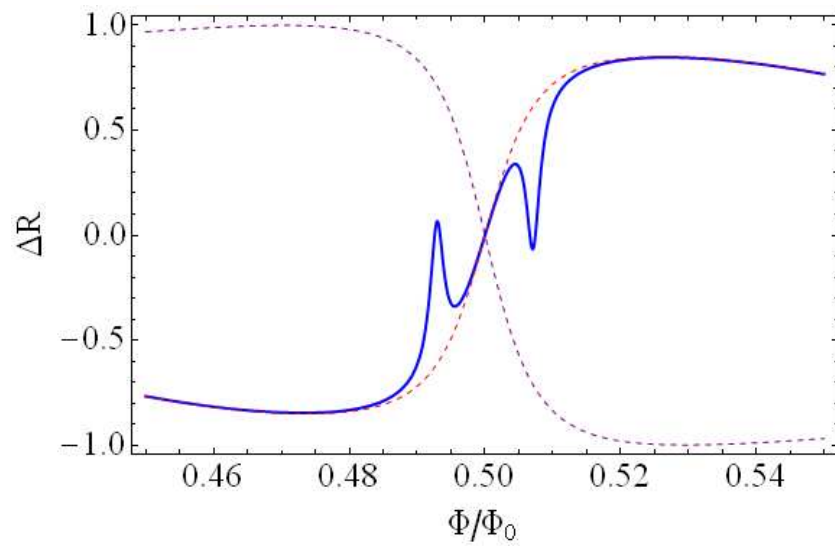
Figure 6.4 shows that at low decoherence rates the qubit resonance takes the form of a sharp peak in the resistance. Figure 6.5 shows that as the decoherence rate is increased, the quality factor of the resonance is reduced until it is no longer a clear peak, but instead a more subtle change in the line shape. Figures 6.6, 6.7, 6.8 and 6.9 show examples of how the resonant behaviour changes as a function of RF frequency and amplitude, for both high and low decoherence rates.

The proceeding section suggests that influence of the Andreev interferometer on the qubit will lead to large decoherence rates, and so it is this type of resonance behaviour that will be observed experimentally. It is, therefore important to examine how these high decoherence rates peaks will behave as we vary the RF signal. Figures 6.10 and 6.11 show the behaviour of the position and amplitude of the peaks as a function of RF frequency and amplitude respectively. The model predicts that the position and amplitude of the peak will change with both RF frequency and amplitude. These predictions are borne out by the experimentally obtained results described in chapter 9.



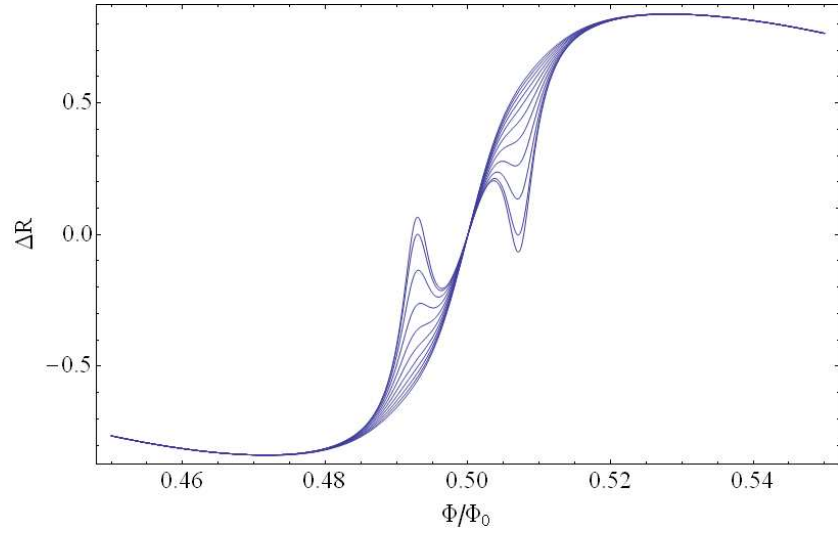


(a)

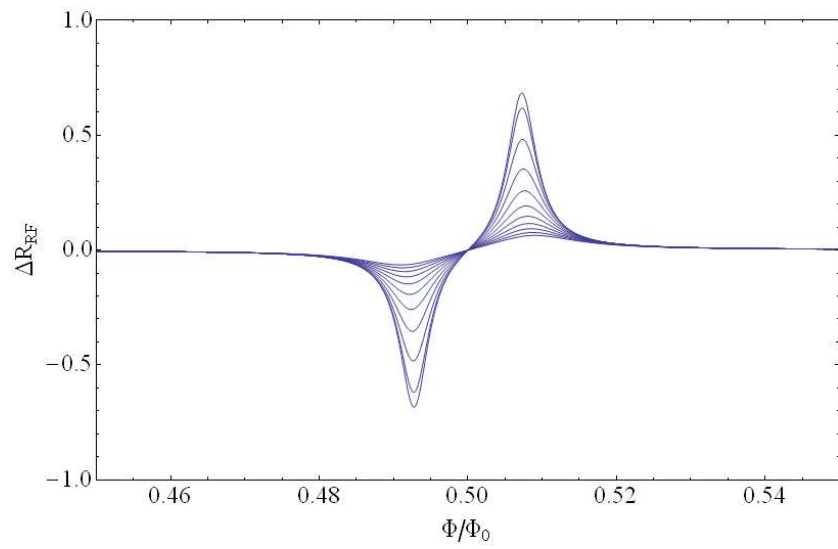


(b)

Figure 6.4: This Figure shows how the model predicts the system behaviour under the influence of a resonant RF field. There are two resonant peaks, either side of the degeneracy point.

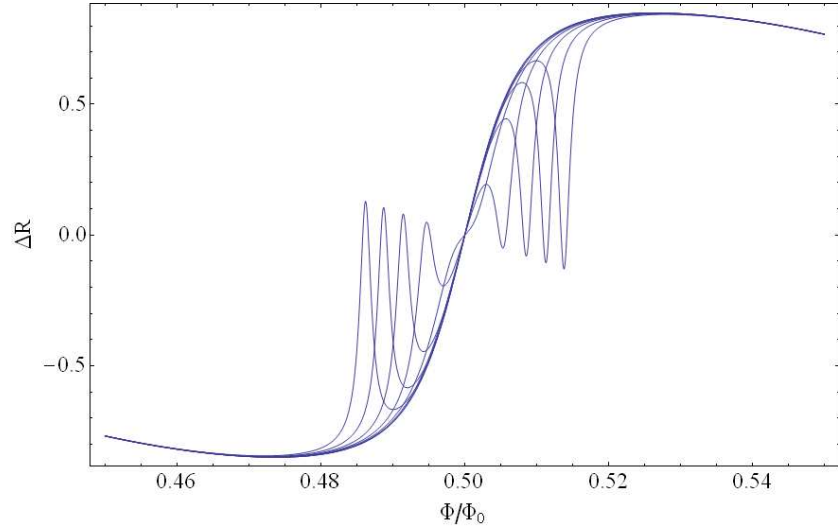


(a)

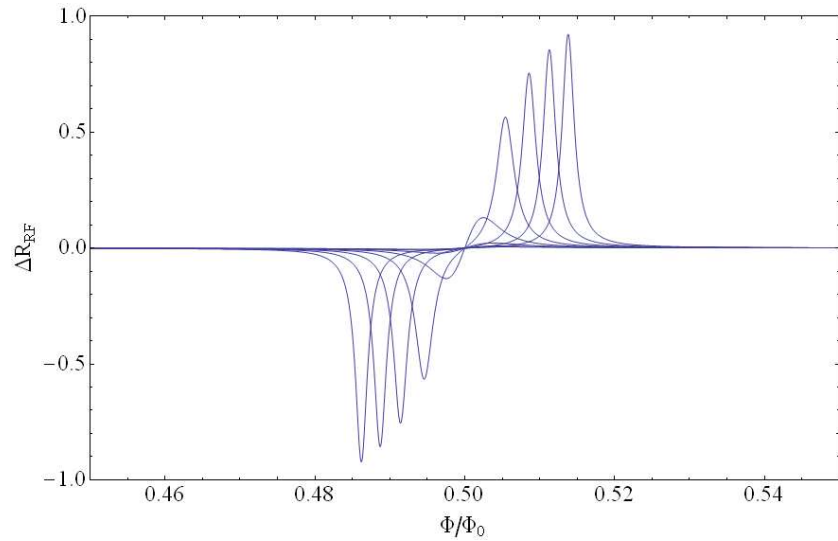


(b)

Figure 6.5: The above Figure shows how the shape of the resonances change with an increasing decoherence rate. (a) Shows the change in resistance as a function of flux. (b) Shows this curve subtracted from the ground state curve. As decoherence increases, the quality factor of the resonance peak is decreased and they change from sharp peaks to broader changes in the shape of the resistance curve.

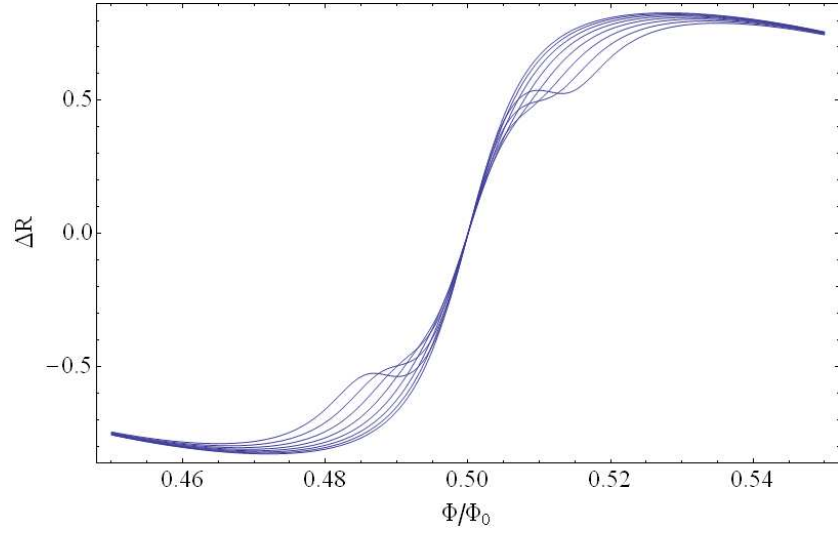


(a)

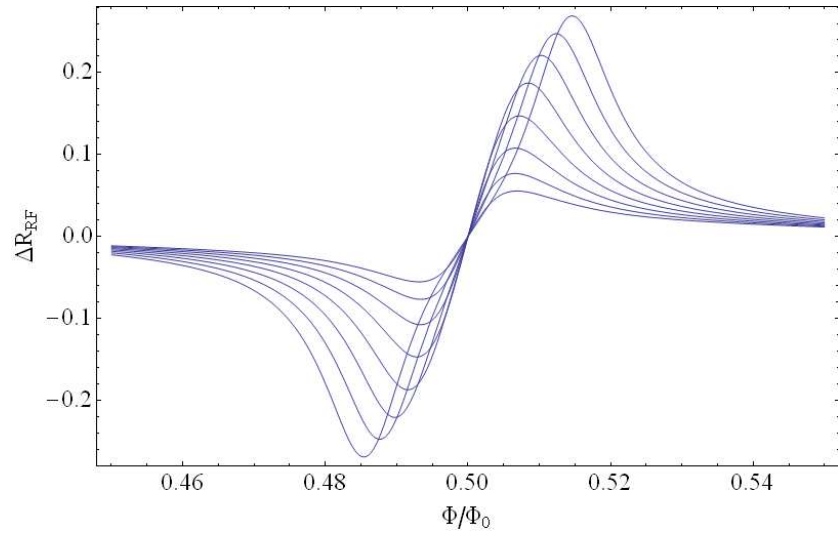


(b)

Figure 6.6:  $\Delta R$  plotted as a function of  $\Phi_e$  for values of  $\omega_{RF}$  between 1GHz and 15GHz for high Q resonances. (a) Shows the change in resistance as a function of flux. (b) Shows this curve subtracted from the ground state curve. As  $\omega_{RF}$  increases the resonances move away from the degeneracy point.

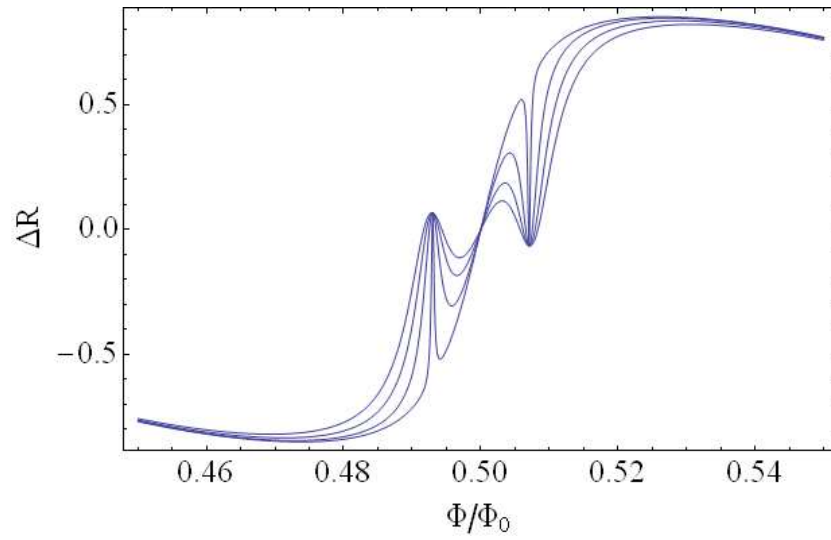


(a)

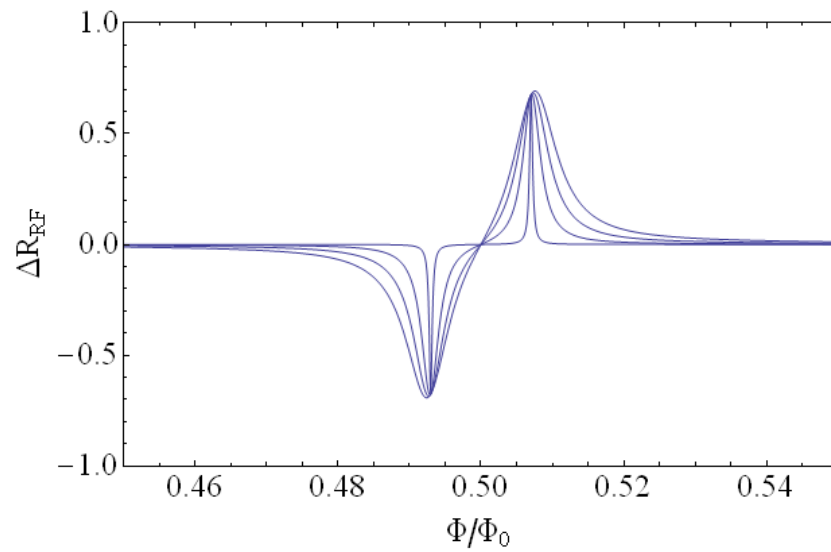


(b)

Figure 6.7:  $\Delta R$  plotted as a function of  $\Phi_e$  for values of  $\omega_{RF}$  between 1GHz and 15GHz for low Q resonances. (a) Shows the change in resistance as a function of flux. (b) Shows this curve subtracted from the ground state curve. As  $\omega_{RF}$  increases the resonances move away from the degeneracy point.

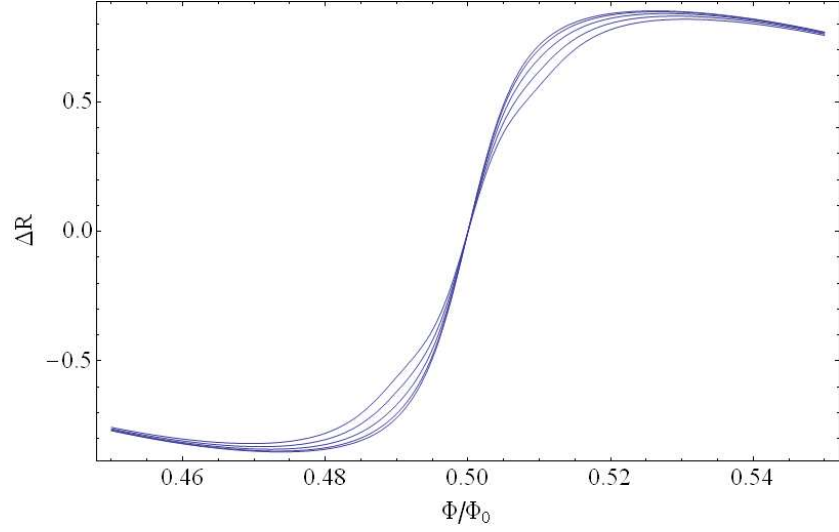


(a)

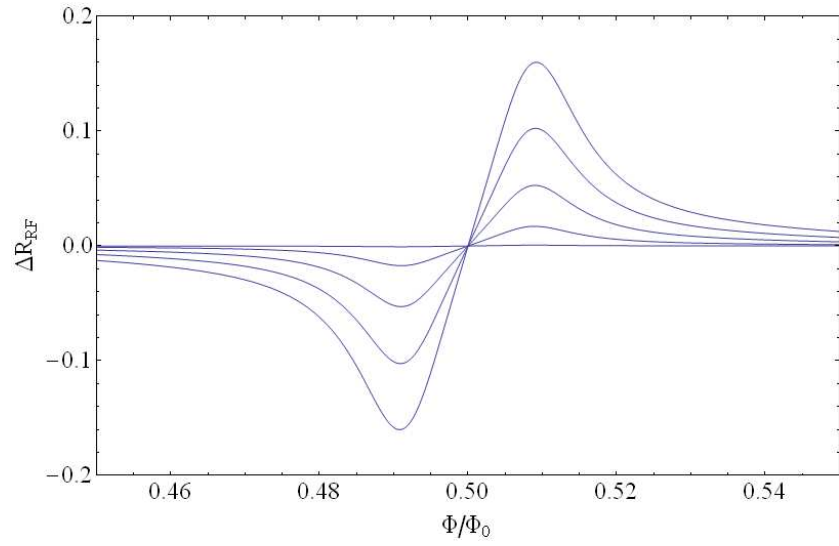


(b)

Figure 6.8:  $\Delta R$  plotted as a function of  $\Phi_e$  for values of  $\omega_{rabi}$  between 0 and  $1.5 \times 10^{-9}$  for high Q resonances. (a) Shows the change in resistance as a function of flux. (b) Shows this curve subtracted from the ground state curve. As  $\omega_{rabi}$  increases the resonances increase in width.



(a)



(b)

Figure 6.9:  $\Delta R$  plotted as a function of  $\Phi_e$  for values of  $\omega_{rabi}$  between 0 and  $1.5 \times 10^{-9}$  for low Q resonances. (a) Shows the change in resistance as a function of flux. (b) Shows this curve subtracted from the ground state curve. As  $\omega_{rabi}$  increases the resonances increase in width.

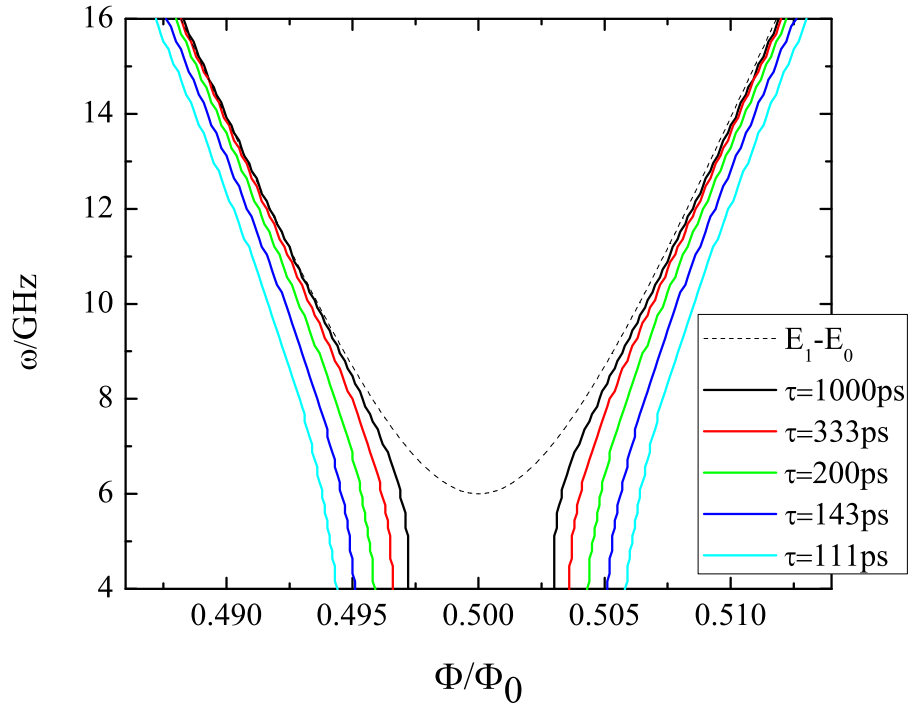


Figure 6.10: The above Figure shows how the model predicts the position of resonances at high RF amplitudes and low coherence times will change as a function of RF frequency. The dotted line shows the energy spectrum of the qubit with  $E_j/E_c = 200$  and  $\Delta = 3\text{GHz}$ . The solid lines show the position of the resonance peak as a function of RF power for coherence times between 111ps and 1000ps.

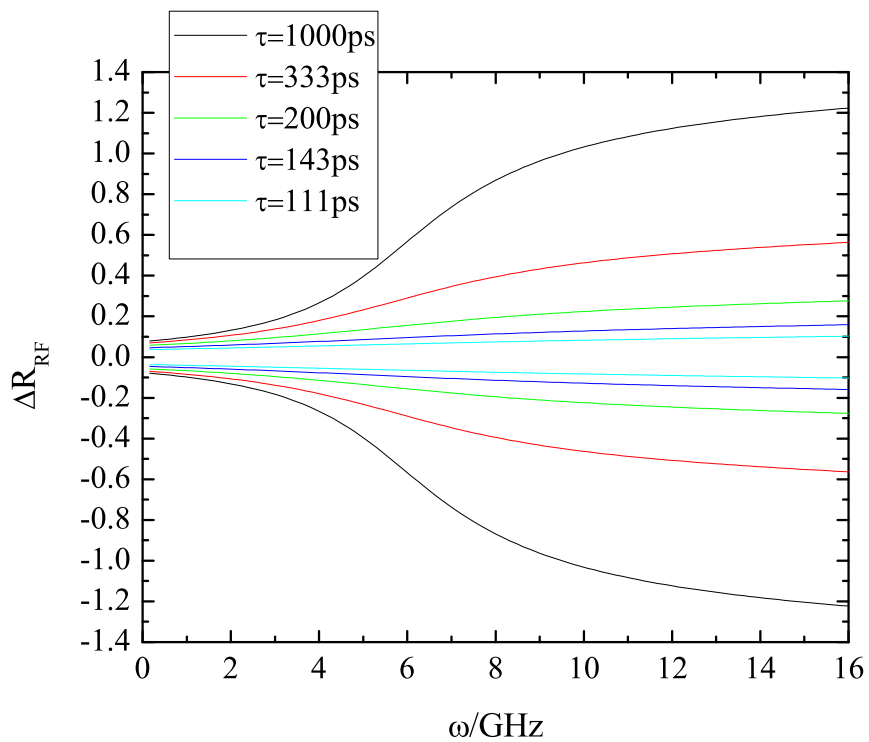


Figure 6.11: The above Figure shows how the model predicts the amplitude of resonances at high RF amplitudes and low coherence times will change as a function of RF frequency. The solid lines show the position of the resonances peak as a function of RF power for coherence times between 111ps and 1000ps.



# Chapter 7

## Fabrication

### 7.1 Introduction

The previous chapters have examined the theory describing flux qubits and Andreev interferometers. We now move onto more practical matters. In this chapter, the process used to fabricate the qubit/interferometers is outlined, and in the next chapter the measurement system used to test their properties at low temperatures is described.

The structures tested in this project are made by evaporating a thin film onto a silicon substrate. Four separate layers are used to create the structures. Of particular interest is the qubit layer, where a novel tri-layer polymer-germanium-polymer resist system was used. This technique allowed the application of selective undercutting for Dolan bridge evaporation (evaporation at an angle) and much greater control of the overlap of the Josephson junctions. The four layers fabricated are-

1. Contact Layer, usually Au
2. Andreev Layer, usually Ag
3. Spacer Layer, usually AlO
4. Qubit Layer, usually Al

The different techniques used to create each of these layers is detailed on the following pages. This new fabrication procedure was developed by myself, Professor Petrashov and Dr. Shaikhaidarov.

## 7.2 Fabrication Techniques

### Resists

The creation of each layer starts with the sample being covered with one or more resists. These resists form the masks which define the structure created. In order to ensure that an even and controllable thickness of resist on the sample, resists are spread by placing a drop of the resist in solution on to the sample, and then rotating it at several thousand RPM. The thickness achieved is controlled by the type of resist used, the concentration of the solution and the speed of rotation. The sample is then placed on a hot plate and baked to evaporate the solution and harden the resist.

In general, two resists are used in conjunction. The top layer resist acts as a mask and defines the pattern of structures created on the chip. The bottom layer resist is thicker and develops at a slightly quicker rate. This makes the lift off of the unneeded thin film from the sample easier, and makes the Dole bridge technique possible.

### Photolithography

Photolithography is used to create structures down to sizes of a few micrometers. Resist is coated onto the sample then a ‘master’ mask (made from chrome covered quartz) is placed over the sample and it is exposed to UV light. The UV light damages the polymer chains in the resist allowing them to be easily dissolved by a developer and when this is done a copy of the mask has been created in the resist.

The advantage of UV lithography is that all areas of the samples are exposed simultaneously. This means that large structures can be exposed quickly, and that many different structures (in this case dozens of contact layers) can be exposed at once. The disadvantage of UV lithography is that the maximum resolution achievable is limited by diffraction.

In this project, particular care has to be taken during UV lithography to ensure that-

- The wafer is clean before depositing the resists; this is achieved through oxygen plasma etching.
- There is good contact between the chrome mask and the resist.
- The resist is developed long enough to ensure a good undercut in the bottom layer resist, allowing for easier lift-off of the deposited metal.

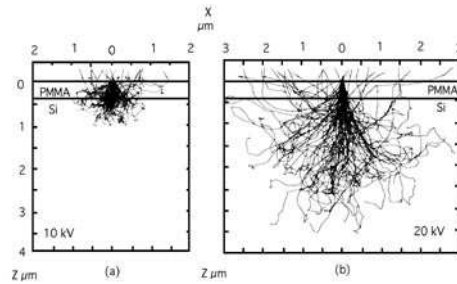


Figure 7.1: Monte Carlo simulation of electron scattering in resist on a silicon substrate at a) 10 kV and b) 20 kV. From [66].

## Electron Beam Lithography

In electron beam (e-beam) lithography, a beam of electrons is used to directly draw a pattern into a resist. Electrons are produced by heating the cathode, then accelerated to a large velocity by a high voltage and focused on a small spot using EM lenses. This spot is then used to expose a pattern of dots on the resist. Exposure to the high energy electrons causes chain scission in the polymer based resist. This means that these sections dissolve quickly in developer, causing a positive mask of the structure desired.

Over exposure of the resist can lead to cross linking of the chains in the polymer. This has the opposite effect to chain scission, causing the resist to develop more slowly and creating a negative mask. In this project, this was something that had to be avoided.

During e-beam lithography the effect of electron scattering must be taken into account. Monte Carlo simulations (see figure 7.1) show that forward scattering of electrons leads to a slight broadening of the image, while back scattering of electrons causes a large fog of exposure. This can lead to over exposure of the resist and distortion of the pattern. This effect, known as the proximity effect, can be minimized by using a thin top layer resist, and by adjusting the dosing pattern to take account of the back scattering of electrons.

Electron beam lithography can be used to create structures with resolutions of  $0.1\mu\text{m}$ , much smaller than what is possible with optical lithography. The disadvantage of e-beam lithography is the amount of time it takes to create each mask. Whereas in optical lithography many structures can be created simultaneously, in e-beam lithography each element of each structure must be written in individually. This makes the process too slow for most commercial applications.

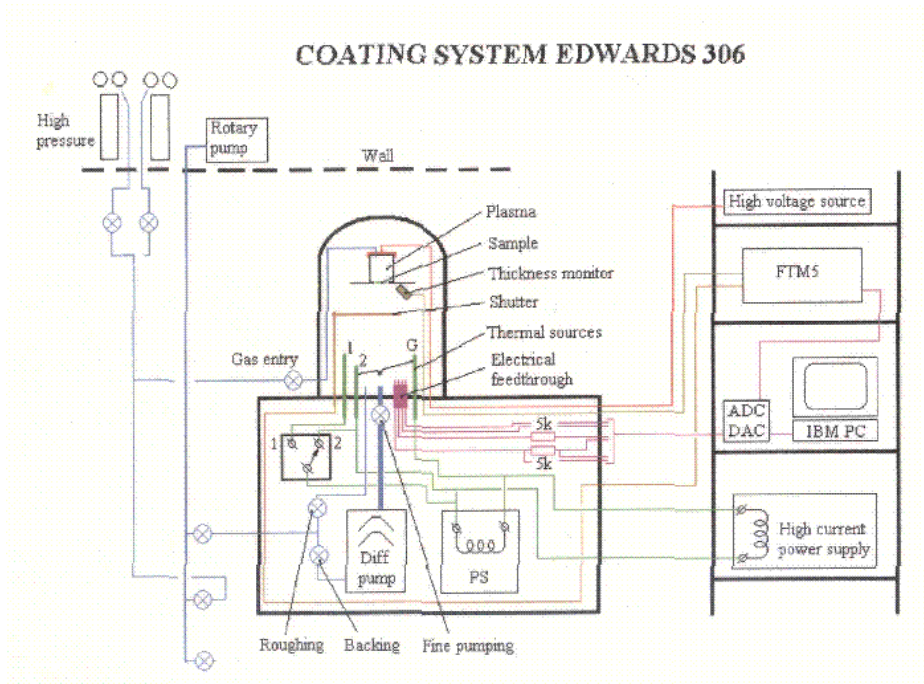


Figure 7.2: Schematic of the evaporator. A vacuum of  $< 5 \times 10^{-6}$  Torr is achieved using a combination of rotary and diffusion pumps. There is a small quartz chamber inside a bell jar which can be used for in situ etching of the sample.

### Thin Film Evaporation

In this project all of the thin metal films created have been thermally evaporated. A diagram of the evaporator used in this project is shown in Figure 7.2. The chamber of the evaporator is pumped down to a pressure of  $5 \times 10^{-6}$  Torr using a rotary and diffusion pump. The metal charge is placed in a small tungsten boat at the bottom of the chamber where it can be heated by passing a large current through the sample. The sample sits on a stage at the top of the chamber, which can rotate in order to allow the Niemeyer-Dolan technique (evaporation at an angle) to be used. Above the sample is a smaller chamber that can be filled with argon gas to allow in situ etching of the chip.

## 7.3 Layers

### 7.3.1 Contact Layer

The contact layer is made of Au using photolithography techniques. Its purpose is to act as a set of leads between the microscopic test structure and the macroscopic measurement system. The design used for the contact layer can be seen in Figure 7.3. It is created using photolithography techniques as shown in Figure 7.3.1. Dozens of versions of the contact layer are fabricated simultaneously on a circular 100mm diameter 5mm thick wafer of silicon, which is later broken up into individual chips. First, the wafer is cleaned by exposing it to oxygen plasma for 4 minutes. Then, 1200nm layer of LOR-5B is spun onto the wafer and baked. This resist creates an undercut and allows for easier lift of the excess metal film. Then a 400nm layer of S1183 photo resist is spun onto the wafer and baked. This is the layer that after exposure and development defines the shape of the structures created. A mask made from quartz and silver (see Figure 7.3) is placed over the wafer and it is then exposed to UV light for 150 seconds. It is then placed in a MF69 liquid developer for 90s, then washed with de-ionized water and blown dry with nitrogen. At this stage it should be possible to see the pattern developed in the resist, with the undercut created by the first layer of resist clearly visible. The wafer is then placed in an evaporator, which is pumped down to a pressure  $5 \times 10^{-6}$ Torr, and 10nm film of NiCr and a 80nm film of Au evaporated onto the sample. The purpose of the NiCr film is to aid in the adhesion of the Au to the silicon. The wafer is then removed from the evaporator and the excess metal and remaining resist is removed by placing it in microposit remover 1165. The wafer is then, again, rinsed in de-ionized water and blown dry. A picture of a finished wafer is shown in Figure 7.3. At this stage the wafer is scored and then broken up into individual chips.

### 7.3.2 Andreev Layer

The Andreev layer is a 50nm layer of Ag and forms the interferometer and leads of the circuit. It is created using a two layer polymer resist system using e-beam lithography techniques. The steps used to create the contact layer are shown in Figure 7.3.2. A typical design for the contact layer is shown in Figure 7.5. The Andreev layer is fabricated on a 7mm square silicon chip with the contact lead layer already in place. Onto this chip a layer of copolymer resist is spun to a thickness of 1000nm and then baked. This resist forms an undercut and allows for easier lift-off. A layer of PMMA resist is then spun to a thickness of 85nm and then baked. This resist forms the mask

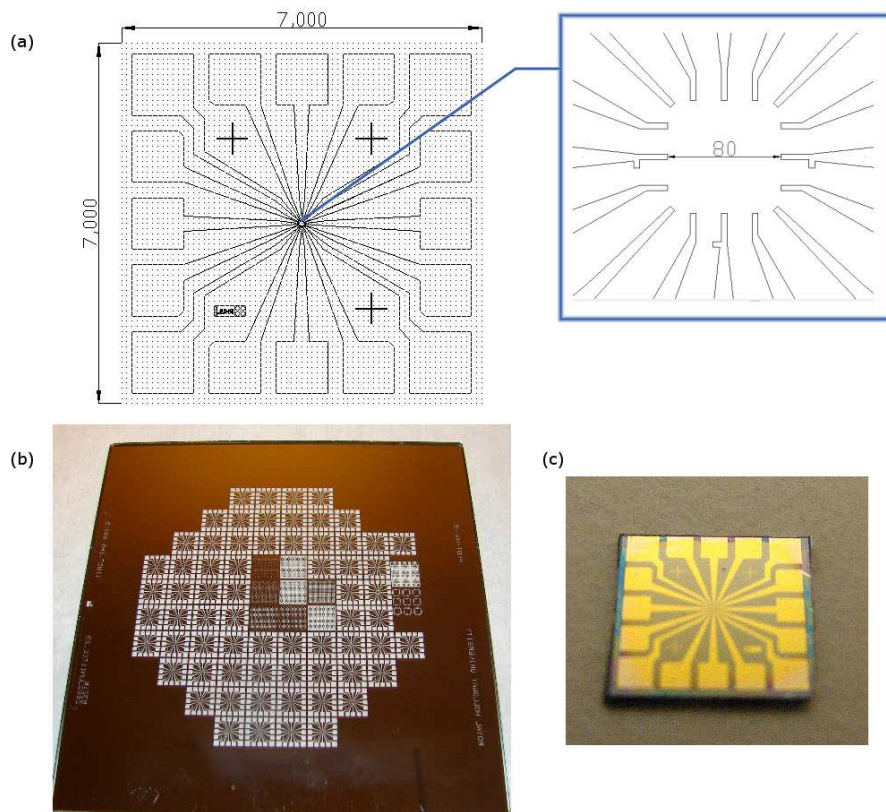


Figure 7.3: (a) Schematic of the contact layer.(b) The quartz mask used to create the contact layer. It has the contact layer pattern repeated many times so that a large number of chips can be created simultaneously on a single silicon wafer. This is then broken up into individual chips shown in (c).


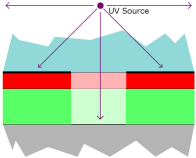
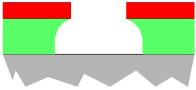
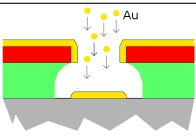

	<p>Silicon wafer is cleaned in oxygen plasma. Two layers of resist (S183 and LOR-5B) are spun onto silicon wafer and baked.</p>
	<p>Quartz-chrome mask is placed over wafer which is then exposed to UV light.</p>
	<p>Resists are developed. Bottom layer of resist creates undercut.</p>
	<p>Wafer is again cleaned in oxygen plasma to remove residuals of resist. A 10nm thin film of Nichrome is evaporated onto the wafer to aid adhesion of gold. 80nm thin film of gold is evaporated.</p>
	<p>Microposit remover is used to wash off remaining resist and lift-off excess silver. Wafer is then again cleaned in oxygen plasma to remove any remaining resist.</p>

Figure 7.4: Steps used in creating the contact layer.

which defines the shape of the structures created. The chip is then placed in the SEM and the pattern is exposed. It is then removed and developed using a solution of 3% de-ionized water and 97% isopropanol for 10s. The chip is placed in the evaporator which is pumped down to a pressure of less than  $5 \times 10^{-6}$ Torr. It is then etched for 20s in an argon plasma to remove residuals of the resist, and 50nm of silver evaporated from a tungsten boat onto the surface of the chip. After being removed from the evaporator, the excess metal film and remaining resist is lifted off of the sample by placing it in 1165 microposit remover which has been heated to 70°C. It is then rinsed with isopropanol.

### 7.3.3 Spacer Layer

The spacer layer is a 10nm thick layer of oxidized aluminium. Its purpose is to isolate the Andreev layer from the qubit layer in the position where the wires cross. A design for the spacer layer can be seen in Figure 7.5. The spacer mask layer is fabricated in an almost identical way to that of the Andreev layer. The only difference is that only a single 80nm layer of PMMA resist is used, instead of a layer of copolymer and then PMMA. This is because the mixer used in the copolymer resist, a mixture of ethyl lactate and a small amount of an unknown substance (which the company supplying the resists would not reveal), was found to have a severely degrading effect on the silver in the Andreev layer. Using a single layer of PMMA solves this problem, and the lack of an undercut is not an obstacle to successful lift-off because the design of the spacer layer is so simple.

Once the mask has been created, the chip is placed in the evaporator, which is then pumped down to a pressure of less than  $5 \times 10^{-6}$ Torr, and the 5nm is evaporated onto its surface. Oxygen is then admitted to the evaporator and the pressure is allowed to rise to 80mbar. It is then maintained at this pressure for 5 minutes. The chamber is then pumped back down to less than  $5 \times 10^{-6}$ Torr and the evaporation and oxidation process is repeated. The chip is then removed from the evaporator and the excess material lifted off in the same way as used in the Andreev layer.

### 7.3.4 Qubit Layer

The qubit layer is a 70nm thick layer of aluminium that forms the qubit, as well as the antenna. It is created using a three layer resist system, with a layer of germanium sandwiched between two layers of polymer resist. This allows the undercutting to be developed independently of the image layer,



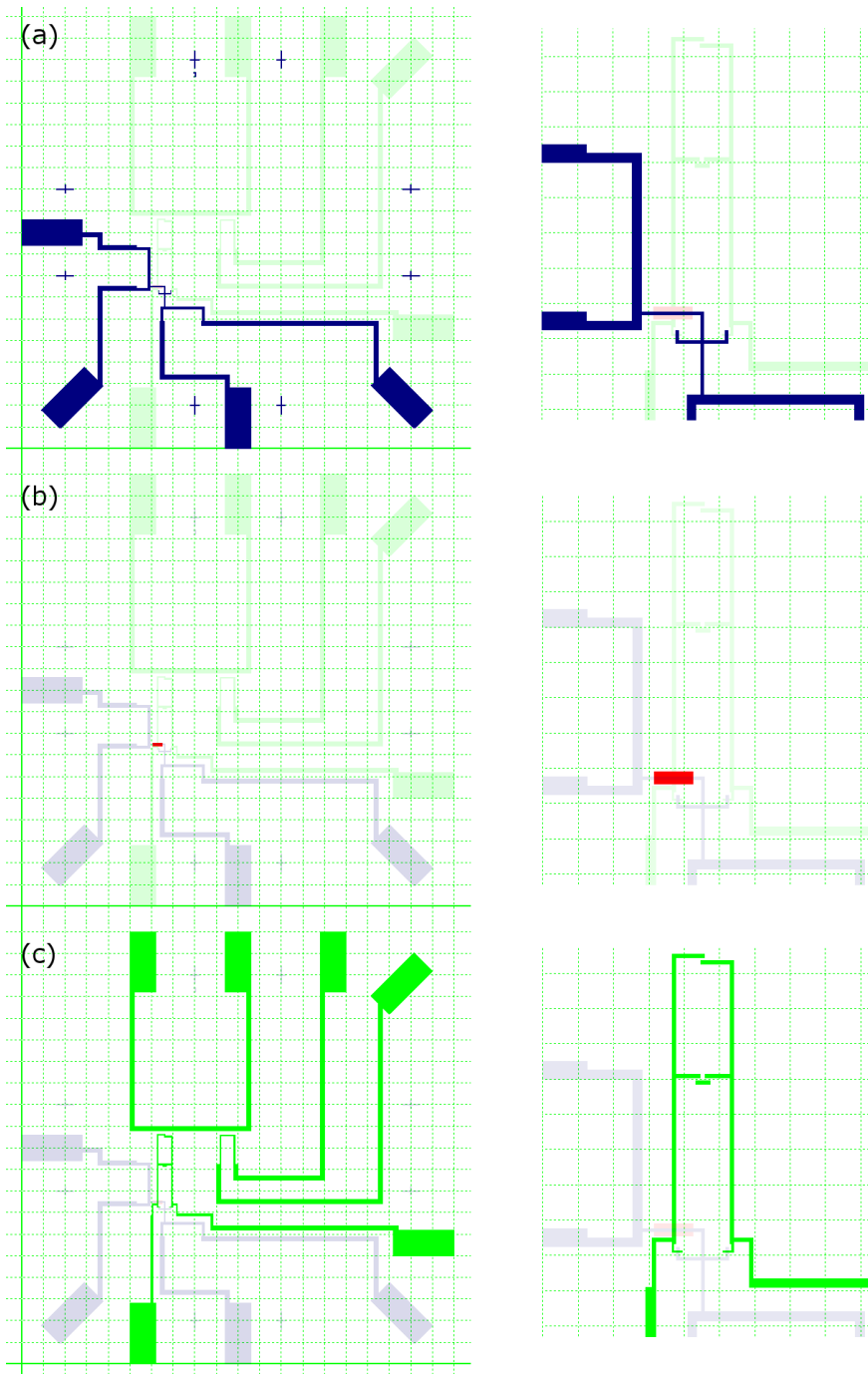


Figure 7.5: The designs of each microscopic layer needed for a complete sample. (a) The Andreev layer. (b) The spacer layer. (c) The qubit layer.


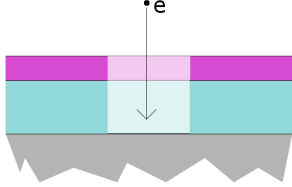
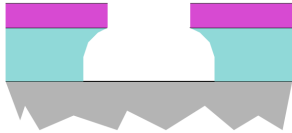
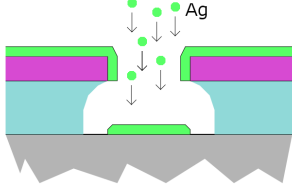

	<p>Two layers of resist (copolymer and PMMA) are spun onto the silicon wafer and baked.</p>
	<p>Resists are exposed in Scanning electron microscope.</p>
	<p>Resists are developed. The bottom layer of resist creates undercut.</p>
	<p>50nm thick film of silver is evaporated onto silicon.</p>
	<p>Microposit remover is used to wash off remaining resist and lift-off excess silver.</p>

Figure 7.6: Steps used in creating the Andreev layer.

giving higher definition to the qubit. In order to create the superconductor/insulator/superconductor interface needed for the Josephson junctions, evaporation is done at two angles using the Niemeyer-Dolan technique (see Figure 7.7). The steps used to create the qubit layer can be seen in Figure 7.3.4.

When using the Doleem bridge technique, it is not possible to create a loop containing only three Josephson junctions. The double layer nature of the technique means that the number of junctions created must always be even, and so using this technique means there will be a forth, unwanted, junction. However, the area of the junction, and therefore the critical current, will be large so that it should not affect the dynamics of the qubit[67].

A typical design for the qubit layer can be seen in Figure 7.5. First a 1000nm layer of PMMA resist is spun onto the chip and baked. Then a 20nm layer of germanium is evaporated onto the sample using the techniques described above. After this, another 80nm thick layer of PMMA resist is spun on and baked. The qubit pattern is then exposed in the resist using the SEM, and developed for 10s in a mixture of 97% isopropanol and 3% de-ionized water. The germanium is then etched through the mask formed in resist so the exposure pattern is created in the germanium. This is achieved by etching for 30s in an oxygen sulphur hexafluoride plasma. Once this is done the chip is returned to the SEM and the undercut pattern exposed and then developed for 60s. The sample is then placed in the evaporator and etched for 20s in argon plasma to any residual resists. Thirty five nanometers of aluminium is evaporated onto the sample at an incident angle of  $10^\circ$ . Oxygen is then admitted to the chamber and the pressure allowed to rise to  $6 \times 10^{-4}$ torr where it is maintained for 5 minutes. The sample is then rotated and another 35nm of aluminium is evaporated, this time with an incident angle of  $10^\circ$  in the opposite direction. Finally, the chip is removed from the evaporator and the excess metal film and resist is lifted off using microposit remover 1165.

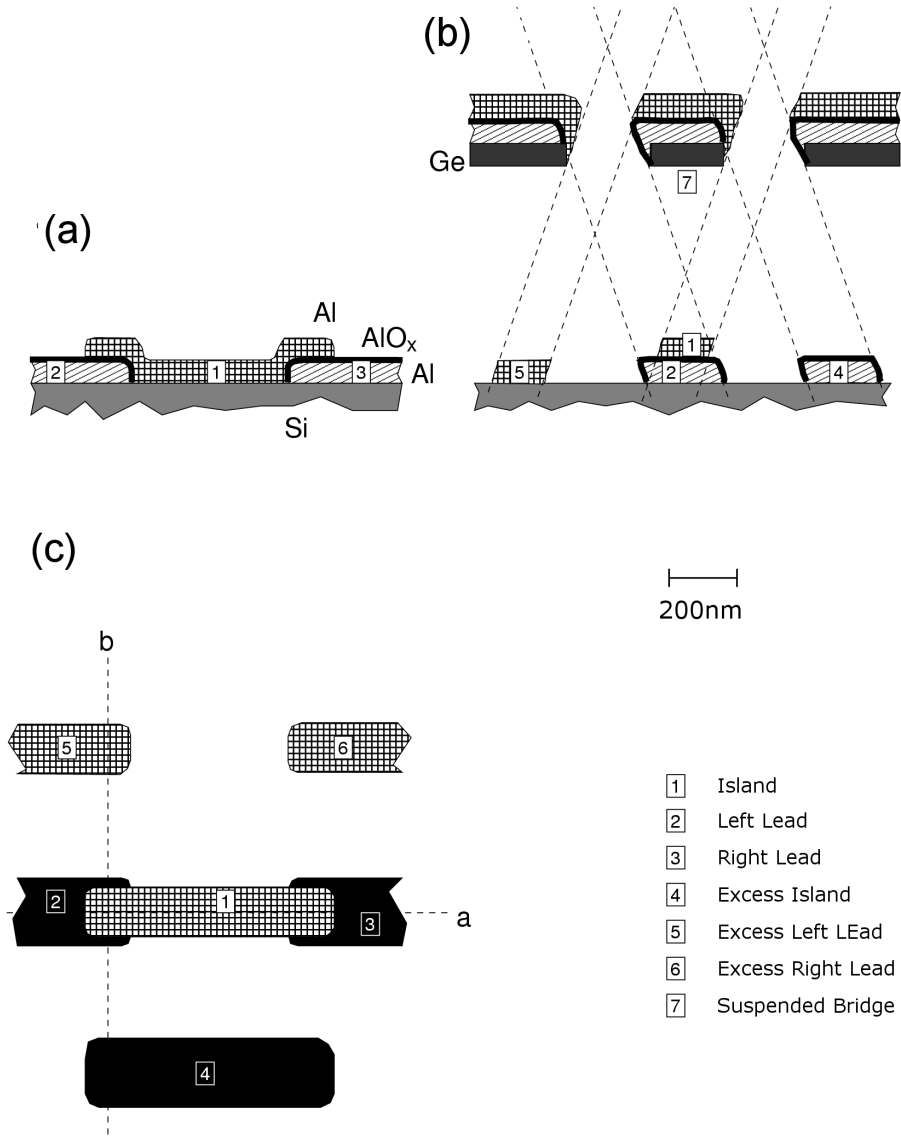


Figure 7.7: Diagram showing the creation of Josephson junctions using the Niemeyer-Dolan technique. (a) Shows a cross section of the structure created along the line of the aluminium wire, (b) shows a cross section of the structure perpendicular to the aluminium wire, and (c) shows a plan of the structure from above with dotted lines indicating where sections (a) and (b) were taken. Image adapted from [68].

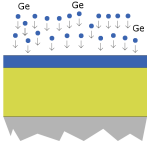
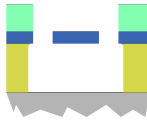
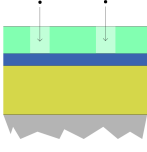

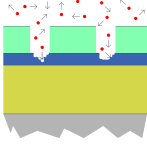

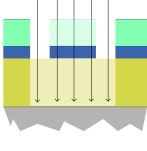
	<p>A 1000nm layer of PMMA resist is spun onto the wafer and baked. 20nm of germanium is then evaporated onto the surface of resist.</p>		<p>The bottom layer of resist is developed, creating an undercut while leaving the mask created in germanium intact.</p>
	<p>The top layer of resist is exposed in a scanning electron microscope.</p>		<p>35nm of aluminium is evaporated onto sample at an angle of 10 degrees to the surface normal. This aluminium is then oxidised. Another 35nm of aluminium is then evaporated at 10 degrees from the surface normal in the opposite direction.</p>
	<p>Resist is developed, then germanium is etched through the mask made in resist with SF<sub>6</sub> plasma.</p>		<p>Microposit remover is used to wash off remaining resist and lift-off excess silver.</p>
	<p>Bottom layer resist is exposed in electron microscope with pattern designed to create undercut.</p>		

Figure 7.8: Steps used in creating the qubit layer.

# Chapter 8

## Measurement Setup

This chapter describes the setup used to measure the state of the qubit. Experiments on flux qubits must be carried out at low temperatures. Aluminium has a critical temperature of 1.2K, but in order to avoid thermal excitation of the qubit the sample must be cooled well below this to millikelvin temperatures. To achieve this a dilution refrigerator was used, allowing the sample to be cooled to temperatures of less than 20mK. In order to minimize decoherence of the qubit caused by the environment, the qubit must be as much, as possible, decoupled from any external noise. To achieve this the qubit was shielded and all of the wiring connecting to the qubit was heavily filtered. To avoid the problems associated with employing commercially available filters at low temperatures, a custom tape filter was used[69]. The sample is contained within a radio frequency tight copper box attached to the mixing chamber of the refrigerator. The dilution refrigerator and all of the measurement equipment was housed within a screened room. The computer used to record data was outside this room and connected via a fibre optic cable.

The measurement setup used is shown in Figure 8.1. The measurement electronics and wiring can be divided into three groups, one working at low frequencies used to probe the resistance of the Andreev interferometer, one used at microwave frequencies used to control the state of the qubit, and one used to control the magnetic flux bias via a small superconducting magnet.

In some experiments a second sample with its own set of wiring was placed at a different position on the mixing chamber.

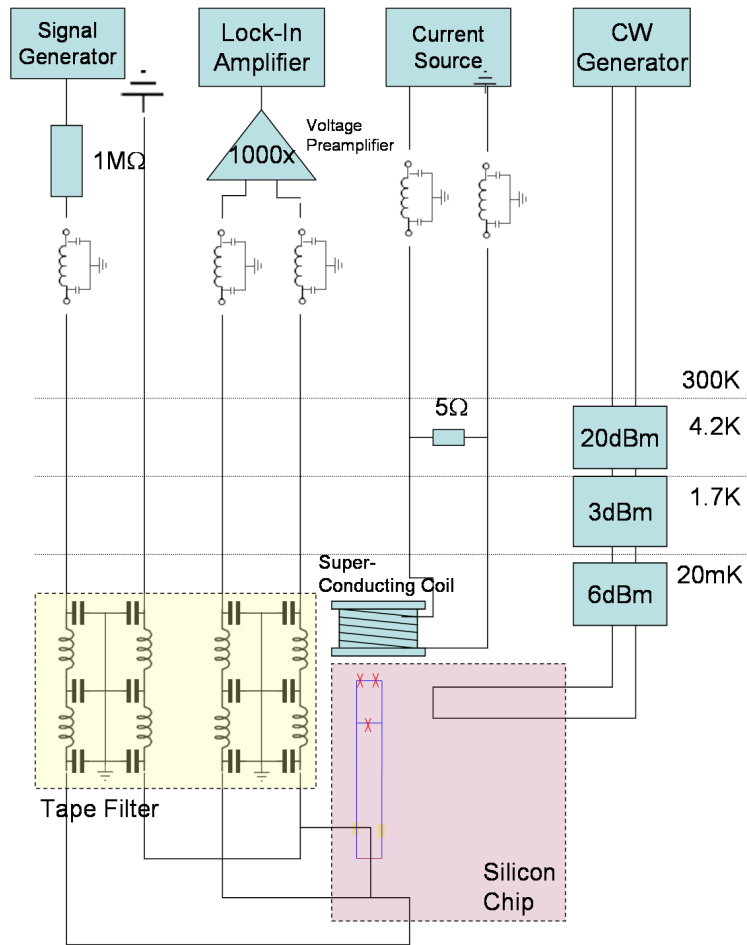


Figure 8.1: This diagram shows the measurement setup used to measure the properties of Qubit/Interferometer samples. Samples were cooled to 20mK in a dilution refrigerator. The fridge wiring can be divided into three groups. Low frequency twisted pair wiring was used to carry out a four point measurement of the resistance of the interferometer. This wiring is filtered by commercial  $\pi$  filters at room temperature and a custom tape filter at 20mK. A superconducting coil was used to generate the external flux. The wiring for this magnet was filtered by a commercial  $\pi$  filter at room temperature. A rigid coaxial cable was used to transmit the RF signal to the qubit. This cable had 29dBm of attenuation at various temperatures between 4.2K and 20mK.

## 8.1 Low Frequency Measurements

In order to probe the resistance of the interferometer a four point measurement was used as shown in Figure 8.1. An oscillator set to a low frequency and a current limiting resistor at room temperature were used to drive a current through the vertical section of the cross. The voltage drop across this section was measured by two voltage probes, which were connected to a low noise voltage pre-amplifier at room temperature. The output from this amplifier was then passed to a lock-in amplifier. Data from the lock-in amplifier was then recorded on a computer outside the screen room via an optical decoupler.

The wiring inside the dilution fridge consisted of a twisted pair ribbon down the mixing chamber stage. Here a bespoke tape filter[70] was used to pass the signal into the copper box containing the sample. Figure 8.2 shows the frequency response of the tape filter. At room temperature commercial  $\pi$  filters were used. The frequency response of these filters can be seen in Figure 8.3.

## 8.2 Microwave Frequencies

In order to manipulate the qubit, it was necessary to irradiate the sample with microwaves of frequency from  $< 1\text{GHz}$  to  $20\text{GHz}$ , both pulsed and continuous wave. The microwaves were carried to the sample by coaxial cable. Attenuators were placed at  $4.2\text{K}$ , at the  $1\text{K}$  pot and at the mixing chamber. The purpose of these attenuators was to heat sink the coaxial line and to eliminate the standing waves caused by reflections in the lines.

Inside the copper box containing the sample, a printed circuit board was used (see Figure 8.5). The sample was glued in the centre of the PCB. Coplanar wave guides, connected to the coax by SMP connectors, led from the edge of the PCB to the sample. Finally, the ends of the wave guides were wire bonded to the sample. The transmission properties of the system were measured using a VNA and the results are shown in Figure 8.4.

The continuous wave signal was generated using an Anritsu MGS69A. In order to generate pulses we combined this signal with a pulse pattern generator, using the setup shown in Figure 8.6. In order to achieve better isolation of the pulses, multiple mixers were used.



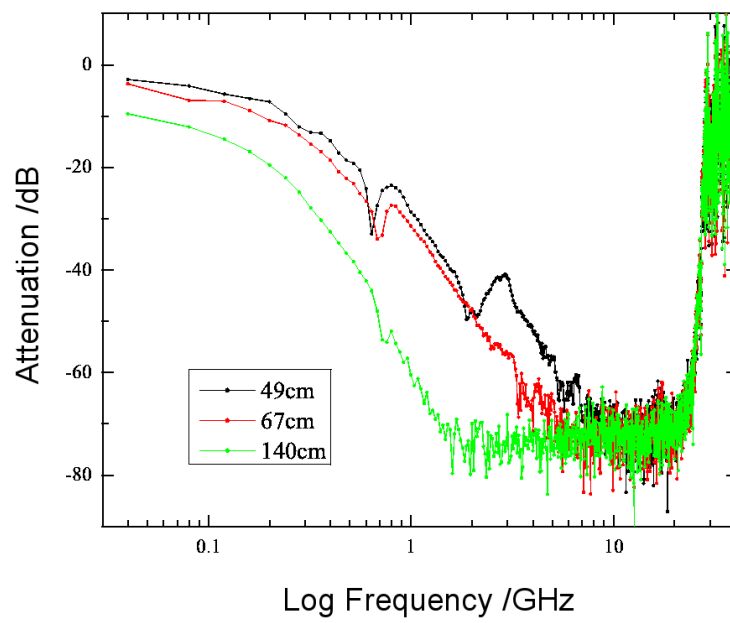


Figure 8.2: Frequency response of the tape filter used on the low frequency wiring.

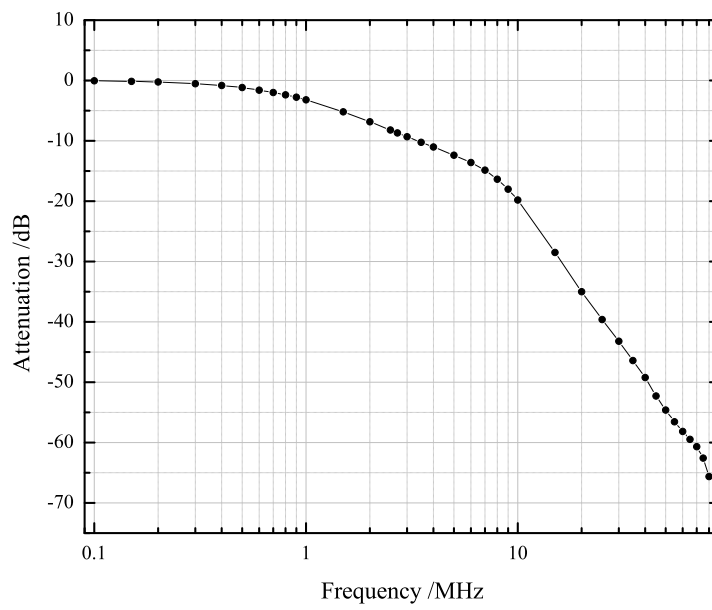


Figure 8.3: Frequency response of the TUSONIX - 4209-053LF  $\pi$  filters.

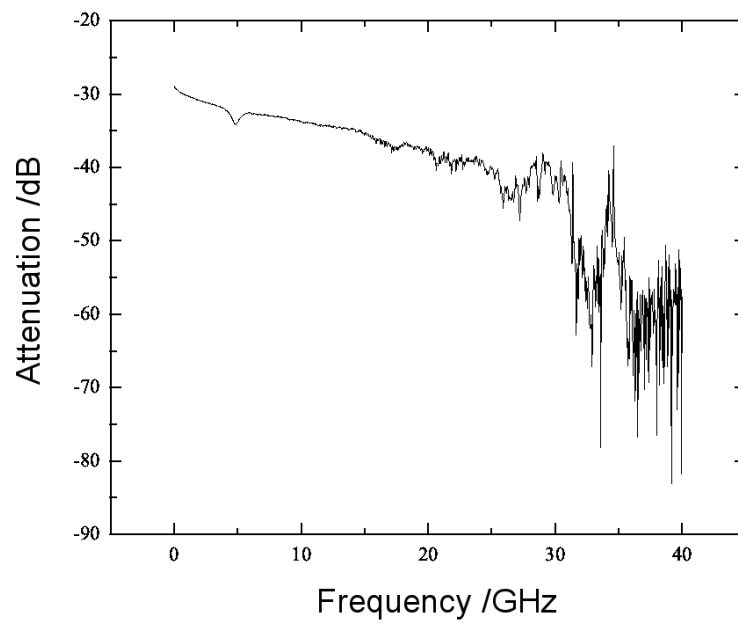


Figure 8.4: Transmission properties of dilution fridge coaxial cable, measured using a VNA.

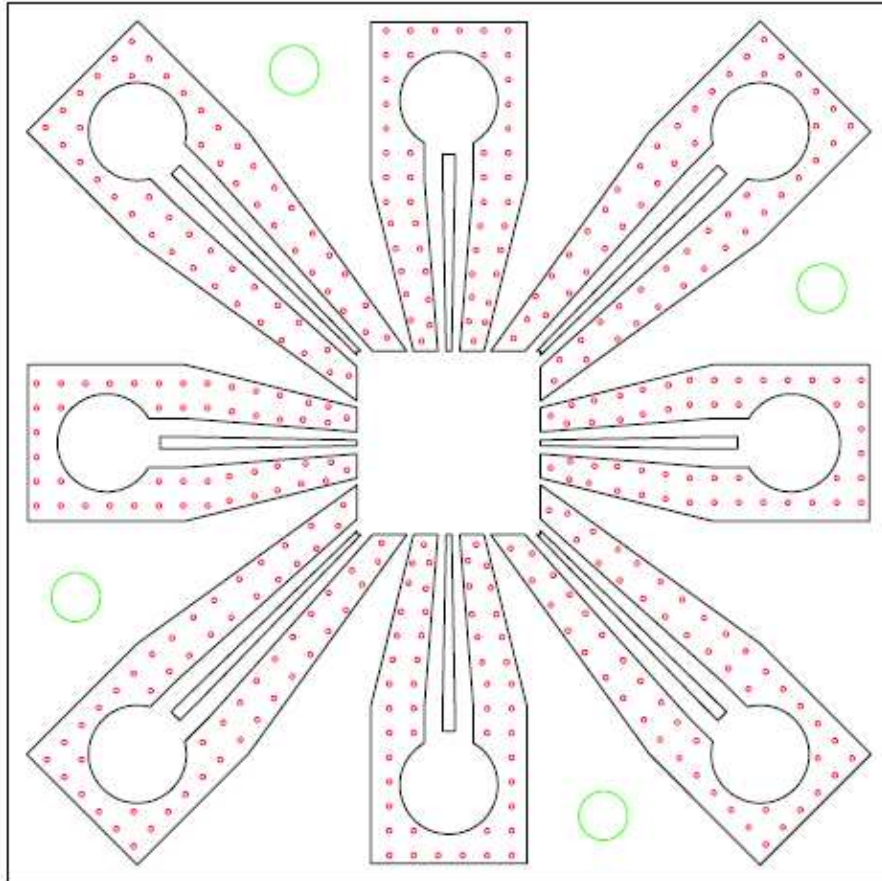


Figure 8.5: PCB onto which the sample was mounted.

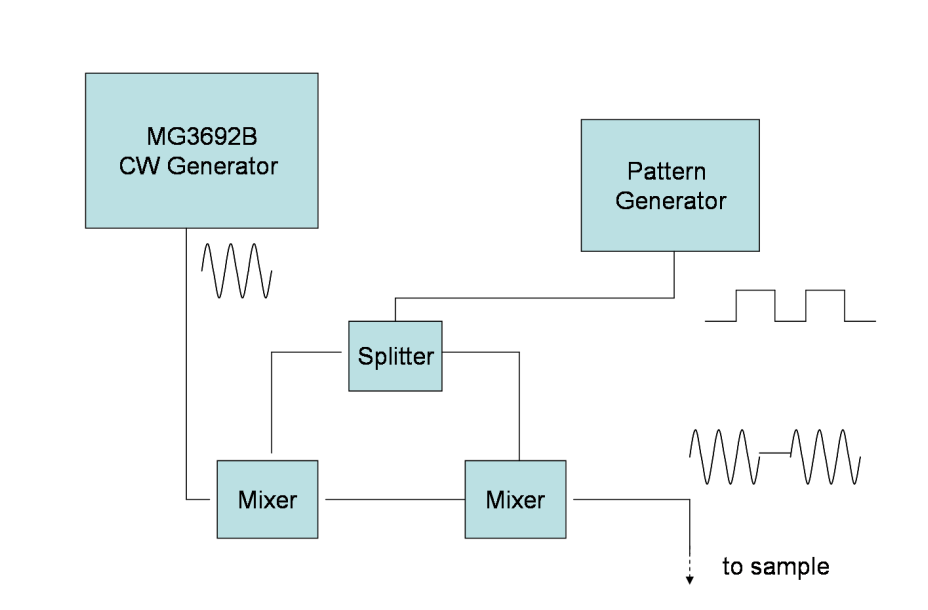


Figure 8.6: Setup used to generate RF pulses.

### 8.3 Magnetic Field

The magnetic field used to control the qubit was provided by a small superconducting coil placed below the copper box. This coil was connected and filtered as shown in Figure 8.1.

### 8.4 Secondary Sample

In some experiments a second sample was placed on the top of the mixing chamber. This sample was used to measure the Josephson and charging energy of junctions that were created at the same time as the main sample. This sample had its own set of wiring, consisting of unfiltered copper twisted pairs.

# Chapter 9

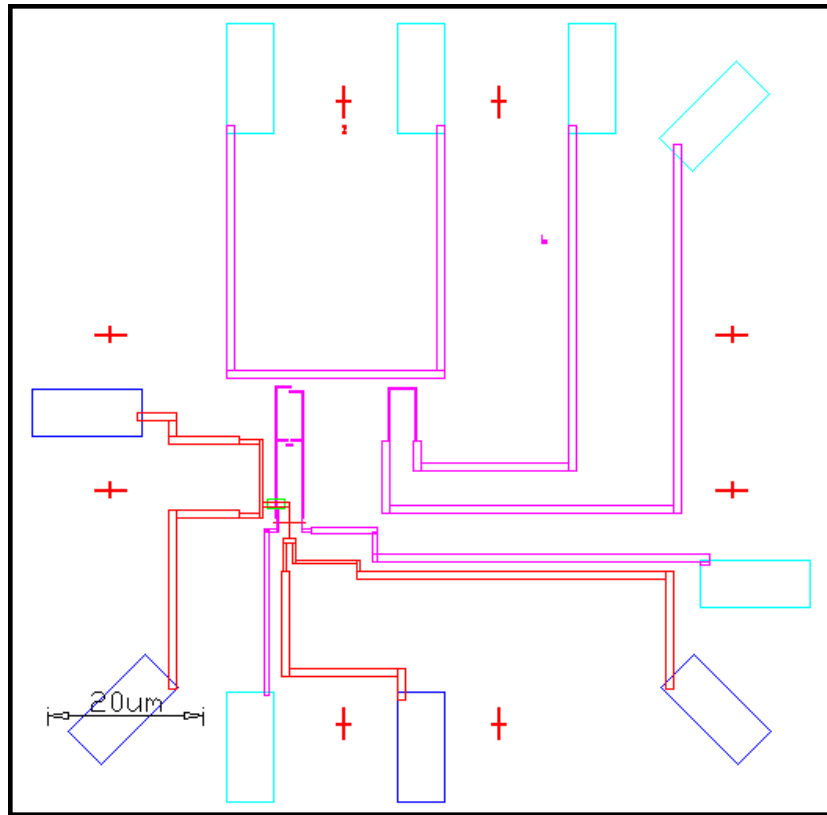
## Results and Discussion

This section discusses the experimental results obtained. Results come from samples created using the methods described in chapter 7. Samples were measured in a dilution refrigerator. The base temperature of the refrigerator was 20mK. The sample was the first sample to be created using the newly developed tri-layer resist system and also the first to include a capacitor to shunt high frequency noise.

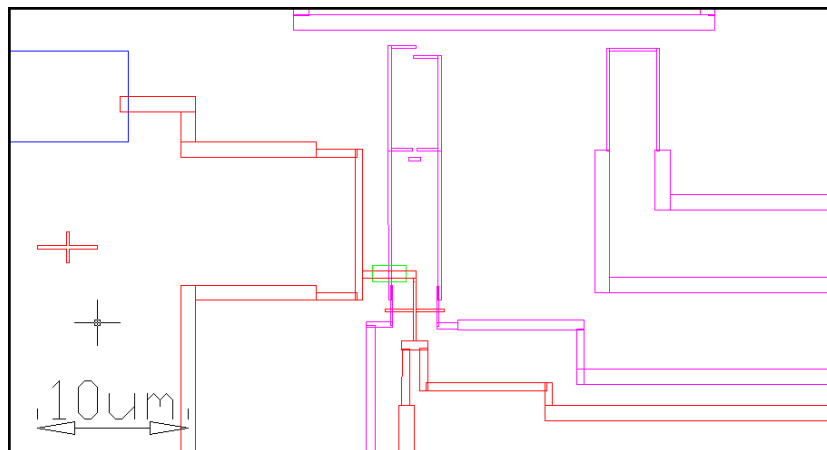
### 9.1 Overview

The sample in this experiment showed the resistance oscillations as a function of applied flux of the type observed in [5], as well as the first evidence of resonant excitation in the qubit, which before this point had not been observed in a flux qubit and Andreev interferometer combination. The sample also displayed a Pi-Shift in the resistance oscillations under high influence of a large amplitude radio frequency (RF) field.

The design of the sample is shown in Figure 9.1 and SEM images of the sample are shown in Figure 9.2. The sample consisted of a qubit interferometer combination with a ratio  $f = 1.5$ , an antenna connected to the RF line of the fridge and used to excite the qubit with microwave radiation, and a secondary antenna connected to the other RF line on the fridge and used to test the RF transmission of the system. In this sample a macroscopic 100pF capacitor was connected across the qubit and interferometer in an attempt to reduce the amount of high frequency noise.



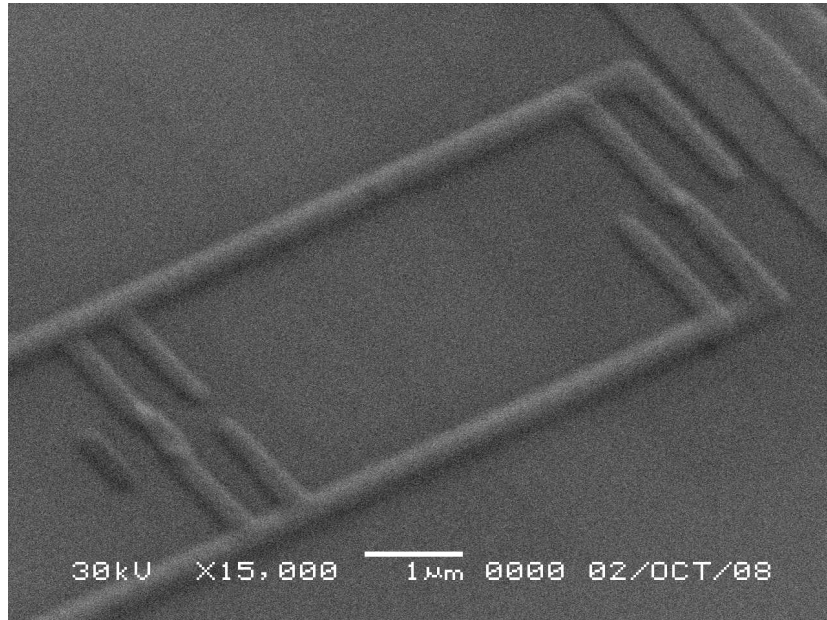
(a)



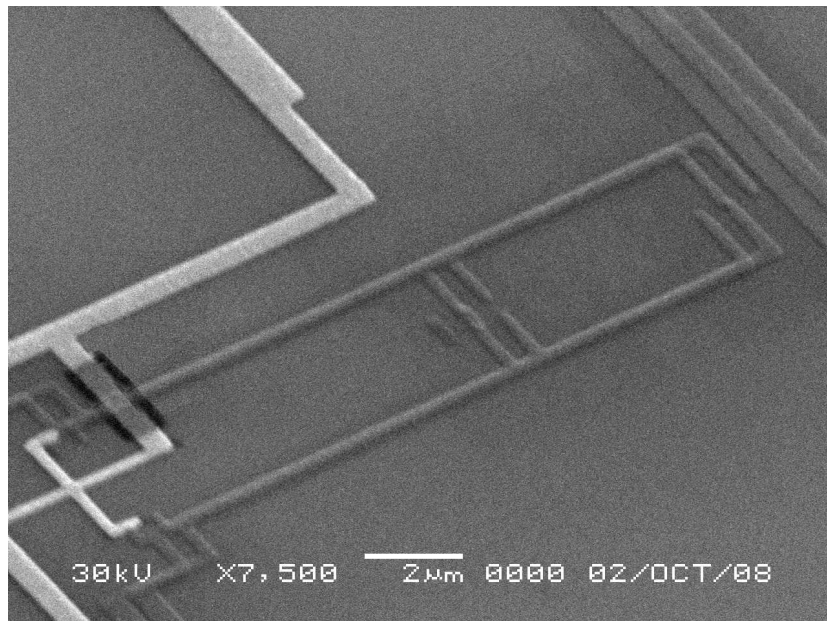
(b)

Figure 9.1: Diagram of the sample used in experiment. Diagram (a) shows the whole sample. The structures were fabricated on a silicon wafer in a  $80\mu\text{m}$  by  $80\mu\text{m}$  exposure area. On this sample are a qubit and interferometer (bottom-left), excitation antenna (top) and secondary test antenna (bottom-centre). Diagram (b) shows a close-up of the qubit and interferometer. The ratio  $f$  was designed to be 1.5. The length of the interferometer was  $3\mu\text{m}$ .





(a)



(b)

Figure 9.2: SEM images of the sample used in experiment 1. (a) Shows a close up of the qubit, while (b) shows the qubit and interferometer together.

## 9.2 Measurements on Qubit in the Ground State

For this experiment we first repeated the measurements of Marshall to characterize the sample by observing it in its ground state[3]. This was done by sweeping a control current through the magnet and continuously measuring the resistance  $R_m$  of the cross using a four point measurement.

As expected,  $R_m$  oscillated as a function of flux, with a sharp change in phase close to  $\Phi_e = n + \Phi_0/2$ . Figure 9.3 shows the oscillations observed for this qubit.

These oscillations were fitted to the theoretical model described in chapter 5 using a least squared fit method. The fitting parameters were the gap  $\Delta$ , the ratio of the measurement loop to the qubit area  $f$  and the screening parameter  $\alpha$  where

$$\alpha = LI_c/\Phi_0 \tag{9.1}$$

This fitting showed that the system was operating as it was designed to, with a value of  $f \approx 1.5$ , a very small screening current ( $\alpha < 0.05$ ). The gap energy for the system was estimated to be  $\Delta/(E_j/E_c) = 0.03 \pm 0.01$ GHz. Assuming  $E_j/E_c \approx 100$ , this gives an energy splitting of  $\Delta \approx 3 \pm 1$ GHz.

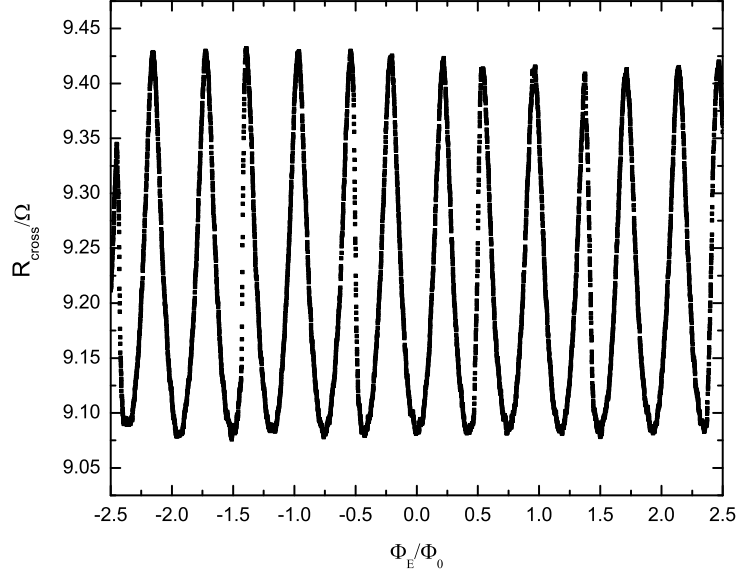
## 9.3 Temperature Measurements

The effect of temperature on the sample was tested. This was achieved by using a small heater on the mixing chamber of the dilution fridge to heat the environment. Using this method two effects were observed.

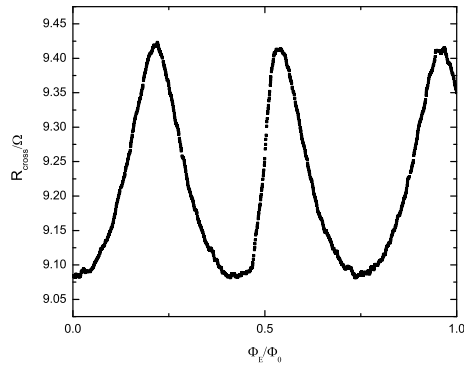
1. A decrease in the amplitude of the oscillations with increasing temperature.
2. A change in the shape of the degeneracy point with increasing temperature similar to that seen under the influence of RF.

### 9.3.1 The Effect of Temperature on Oscillation Amplitude

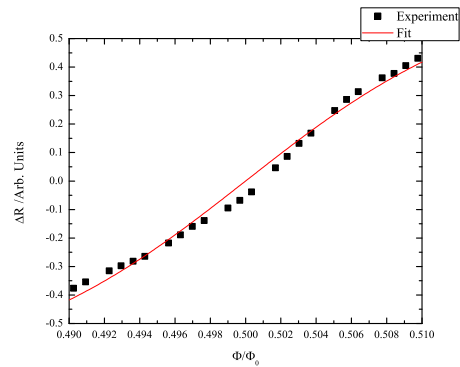
The most obvious effect of increasing the temperature of the system was a reduction in the amplitude of the oscillations, as shown in figures 9.4 and 9.5. This is because heating the system increases electron temperature, allowing the electrons to occupy higher energy states, reducing the number of available



(a)



(b)



(c)

Figure 9.3: The above graph shows the resistance of the interferometer oscillating as a function of external flux. Graph (a) shows the oscillations in a wide range. Sinusoidal oscillations occur due to the flux through the Andreev loop. Close to  $\Phi_e/\Phi_0 = n + 0.5$  the current in the qubit changes direction, causing a sudden change in phase and change in the oscillations that we refer to as the degeneracy point. Graph (b) shows a closer view of the resistance oscillations around the first degeneracy point. (c) Shows the experimental data fitted to the model described in chapter 5.1

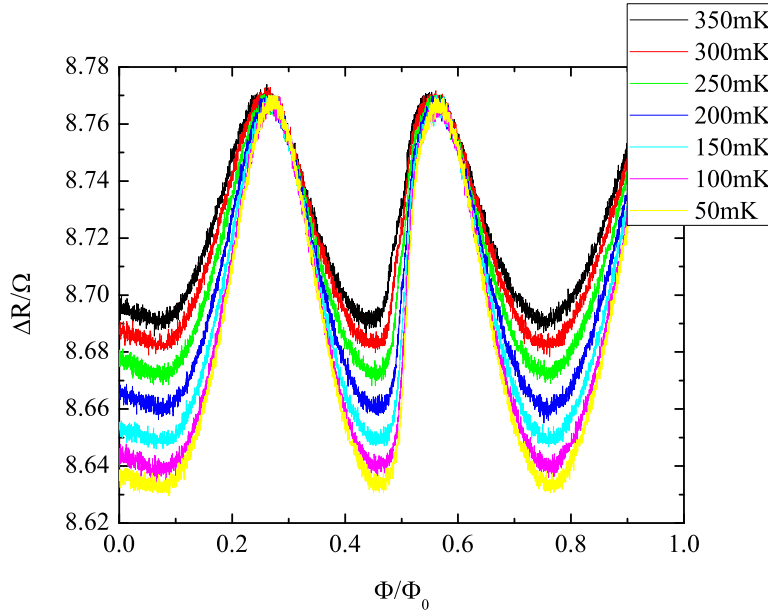


Figure 9.4: Resistance oscillations as a function of flux taken at mixing chamber temperatures between 50mK and 350mK. An increase in temperature leads to a decrease in oscillation amplitude due to the reduction in available Andreev bound states.

Andreev bound states and; therefore, reducing the effect of Andreev reflection on the system.

The reduction of an amplitude of the oscillations with temperature gives a simple way of calculating the heating effect of the RF field. By plotting the amplitude of the oscillations as a function of RF amplitude, we can estimate a conversion factor allowing the calculation of the temperature of the system at a given RF field. The effective heating of the system by RF is 5mK/mV.

### 9.3.2 Temperature Dependent Changes in the Shape of Resistance Curves Close to the Degeneracy Point

The shape of the resistance oscillations close to the degeneracy point was observed to change with temperature. This can be seen in Figure 9.6, which shows curves taken at temperatures between 50mK and 350mK.

There are two possible explanations for this behaviour, which are illus-

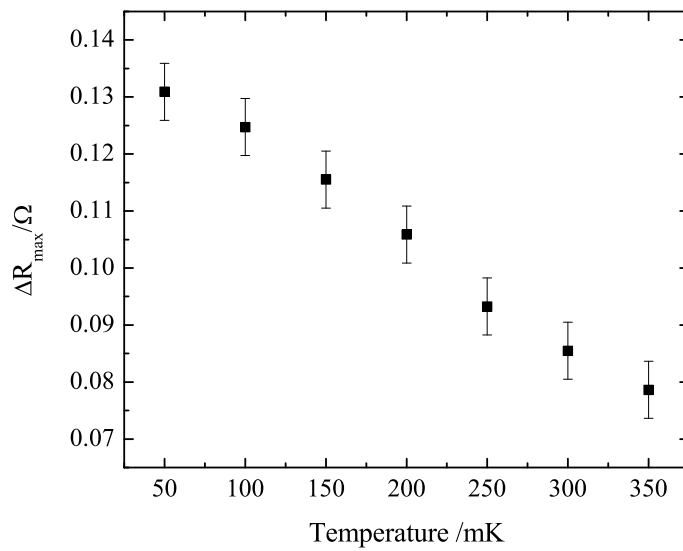
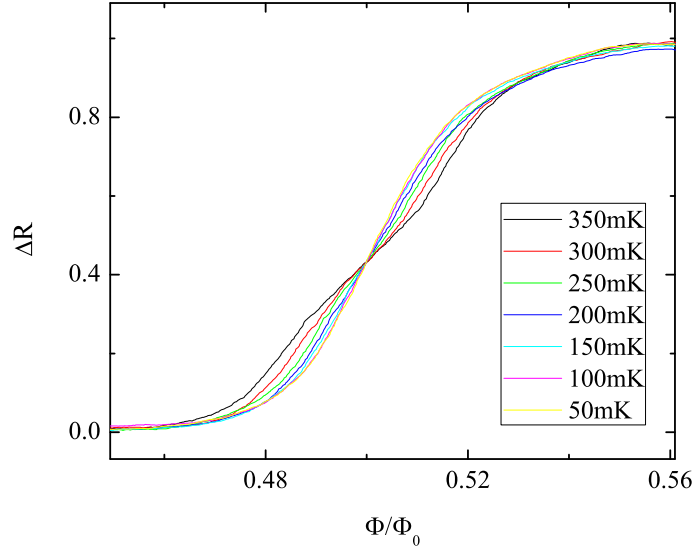
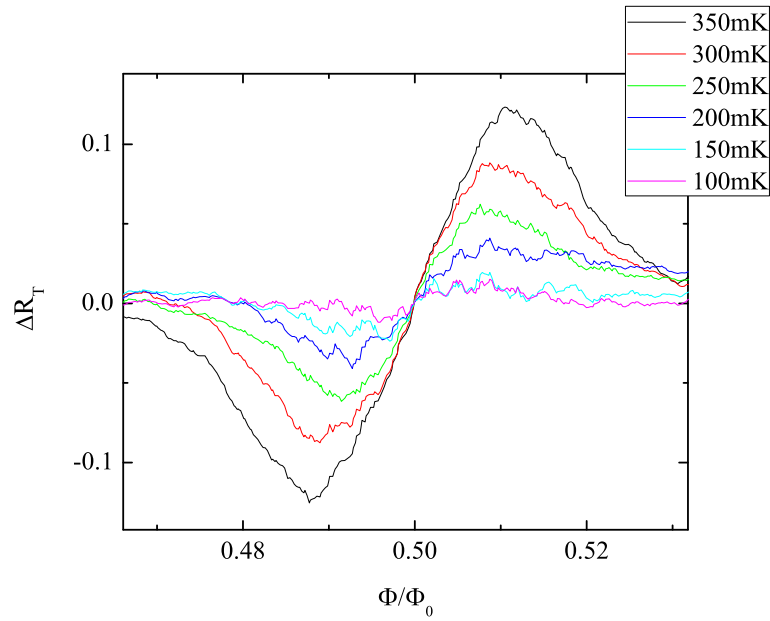


Figure 9.5: Oscillation amplitude plotted as a function of temperature. Increasing temperature leads to a linear decrease in amplitude between 50mk and 350mk.

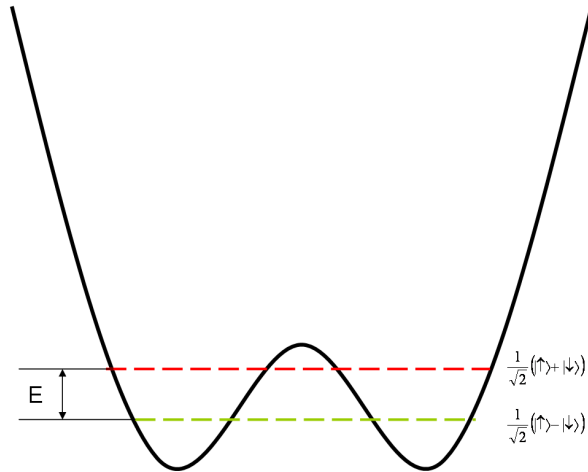


(a)

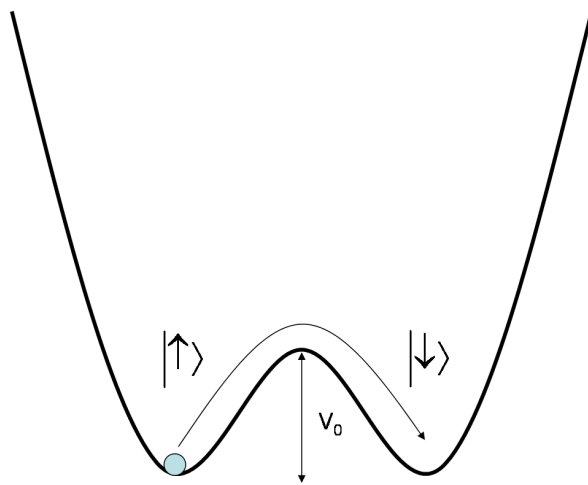


(b)

Figure 9.6: (a) Resistance oscillations close to  $\Phi_e = \Phi_0/2$  for temperatures between 50mK and 350mK. The oscillations have been normalized to account for the reduction in the oscillation amplitude due to heating. (b) Shows these resistance curves subtracted from the one taken at base temperature.

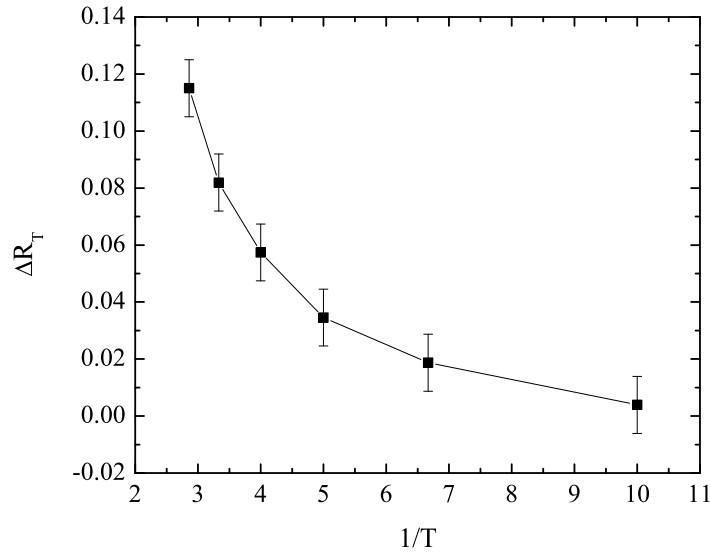


(a)

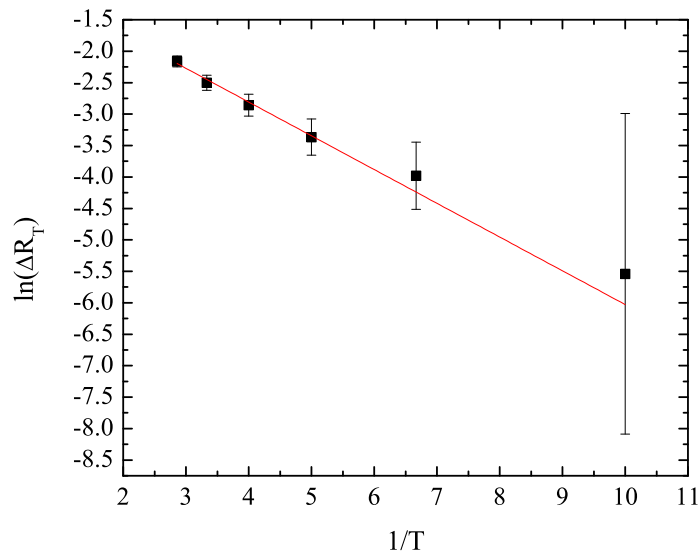


(b)

Figure 9.7: The above Figure illustrates two possible explanations for the temperature dependent behaviour of the qubit. In (a) there is tunnelling between the two potential wells and so the quantum behaves as a two state quantum system. Thermal excitation raises the qubit from the ground to the excited state. In (b) there is no tunnelling and so the system is trapped in either the left or the right well. Thermal energy allows the system to escape over the barrier  $V_0$  causing a change in current direction.



(a)



(b)

Figure 9.8: (a) The change in the resistance plotted as a function of  $1/T$  at a constant flux  $\Phi/\Phi_0 = 0.49$ . By taking the natural logarithm of the resistance and fitting a linear function the resulting data, as shown in (b), the energy splitting between the ground and excited state can be estimated.



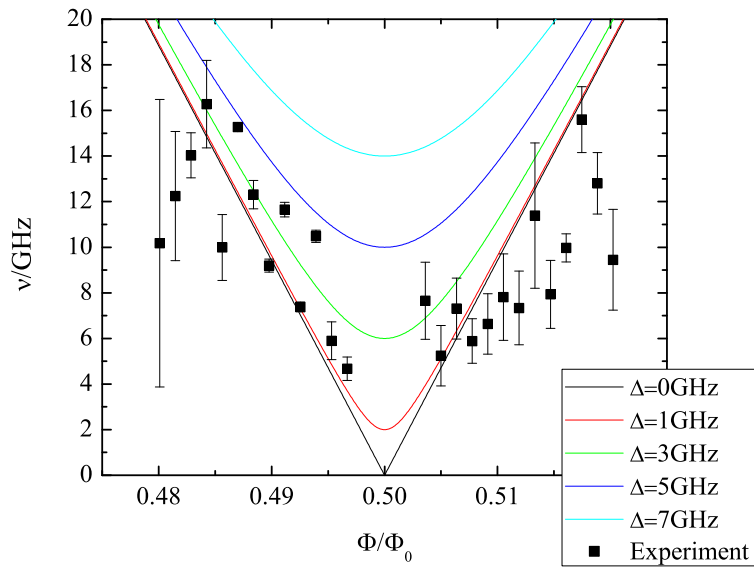


Figure 9.9: An energy spectrum for the qubit, derived by fitting the change in resistance as a function of temperature at many different fluxes. The solid lines shows the energy spectrum,  $E_1 - E_0$ , for values of  $\Delta$  between 0 and 7GHz with  $E_j/E_c = 200$ .

trated in Figure 9.7. The first assumes that in the system tunnelling is possible between the potential wells of the qubit, causing it to behave as a two state system. The change in the resistance curve is then caused by the qubit being thermally excited from the ground to the excited state. The probability of finding the qubit in the excited state is

$$P \propto e^{-E/kT} \quad (9.2)$$

where  $E$  is the energy separation between the ground and excited state.

The second explanation assumes that the system is behaving classically and there is no tunnelling between the potential wells of the system. The two wells represent the two different current directions in the loop, and thermal excitation causes the system to escape over the barrier separating the two wells, resulting in a change in current direction and, thus, a change in resistance. In this case the probability of exciting the system over the barrier would be

$$P \propto e^{-V_0/kT} \quad (9.3)$$

where  $V_0$  is the height of the barrier.

The experimental results seem to support the first of these two scenarios. If the system was behaving classically then the system would be expected to exhibit hysteric behaviour with respect to flux. In practice, no hysteresis was observed.

By plotting the natural logarithm of the change in resistance as a function of  $1/T$ , it is possible to estimate the exponent in 9.2, as shown in Figure 9.8. By repeating this process at many different fluxes, it is possible to plot the behaviour of the exponent as a function of flux, as shown in Figure 9.9. This behaviour is well matched to the energy separation of the two states in flux qubit, with a minimum at  $\Phi_0/2$ , growing larger as the flux moves away from this point.

## 9.4 Behaviour of System When Driven by a Continuous RF Field

In this section the results obtained from the system when it is driven by a continuous RF field are presented. The behaviour observed can be broken down into a number of different phenomenon, as listed below-

- A change in the shape of the resistance oscillations close to the degeneracy point was observed. This effect was dependent on both the

frequency and amplitude of the RF field, and it is believed that it represents the first spectroscopic measurements of a flux qubit using Andreev interferometer.

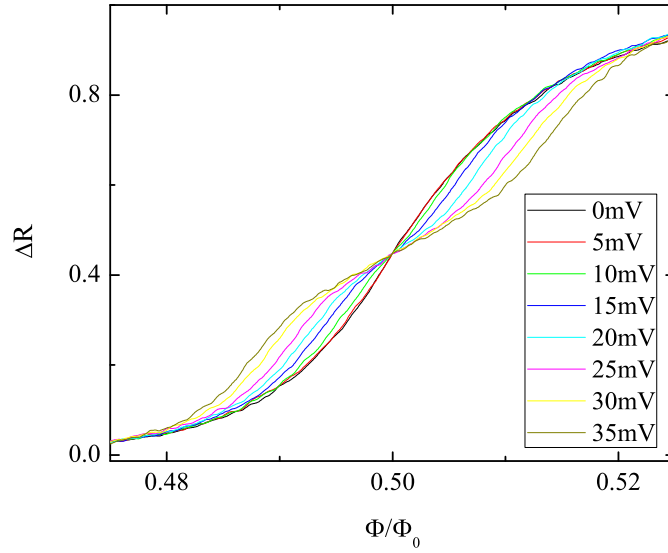
- A Pi shift in the phase of the oscillations was observed at strong RF fields. It is believed that this effect is due to the large modulation of the total magnetic field by the RF field.
- A decrease in the amplitude of the oscillations was observed with increasing amplitude of RF field. It is believed that this is due to the heating of the system as discussed in the previous section.

### 9.4.1 Dependence on RF Field Amplitude

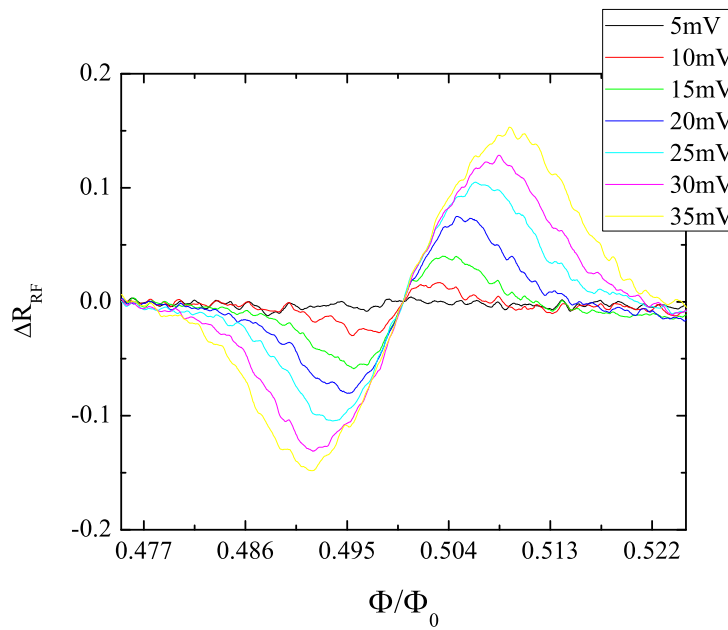
The shape of the resistance curves close to the degeneracy points changes when a RF field is applied to the sample. Plots showing these changes at different RF amplitudes are shown in Figure 9.10. The shape of these changes is consistent with the resonance peaks at high powers and extremely short dephasing times. The amplitude of, and position of, these resonances increases linearly with RF amplitude, as shown in Figure 9.11. This is in good agreement with the model described in chapter 5. By fitting the curves using this model it is possible to estimate the coherence times and  $W_{01}$  of the system, as shown in Figure 9.12. These fittings give a maximum coherence time for the system of  $200 \pm 50$ ps, which is in good agreement with the values calculated in chapter 5.

### 9.4.2 Dependence on RF Field Frequency

The shape of the resistance oscillations close to the degeneracy point was also observed to change with the frequency of the applied RF field. This behaviour is consistent with resonant excitation of the qubit. Curves taken at applied frequencies from 4GHz to 16GHz are shown in figures 9.13. Figure 9.14 shows the position and amplitude of these resonance peaks plotted as a function of frequency. This data was fitted to the model described in chapter 5. By fitting the position of the peaks to the energy spectrum described by 5.2 it was possible to estimate that for this qubit  $E_j/E_C = 200 \pm 100$  and  $\Delta = 3 \pm 1GHz$  (shown in figure 9.14). These means that  $\Delta/(E_j/E_C) = 0.02 \pm 0.01GHz$  which agrees well with the value estimated from the ground state and temperature measurements. We estimate that the coherence time of our system is  $\tau = 150 \pm 50$ ps. Using  $Q = \omega_{01}\tau$  at 10GHz this gives us a quality factor of  $Q = 9 \pm 3$ .

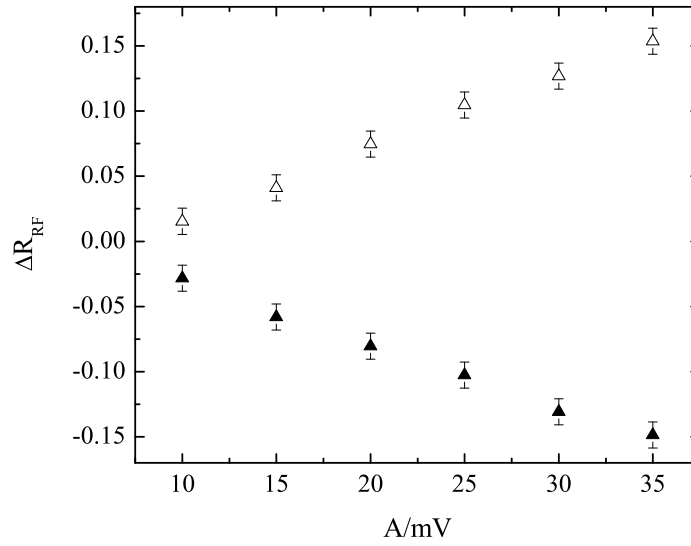


(a)

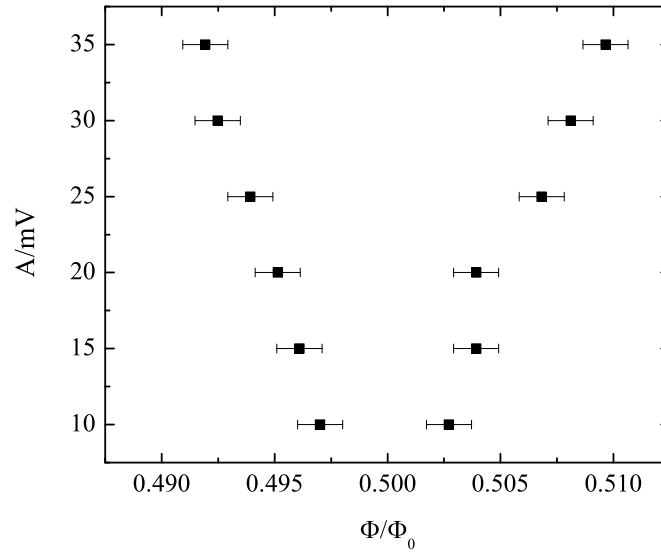


(b)

Figure 9.10: (a) Shows the resistance of the interferometer plotted as a function of magnetic flux at RF field amplitudes between 0 and 35mV. (b) Shows the the resistance at a function flux at RF amplitudes between 5mV and 35mV, subtracted from that taken at 0mV, giving the change in resistance due to RF field.



(a)



(b)

Figure 9.11: The above graphs show the behaviour of the resonance peaks seen in Figure 9.10. (a) Shows the amplitude of the peak as a function of RF amplitude, (b), the position of the peak as a function of RF amplitude.

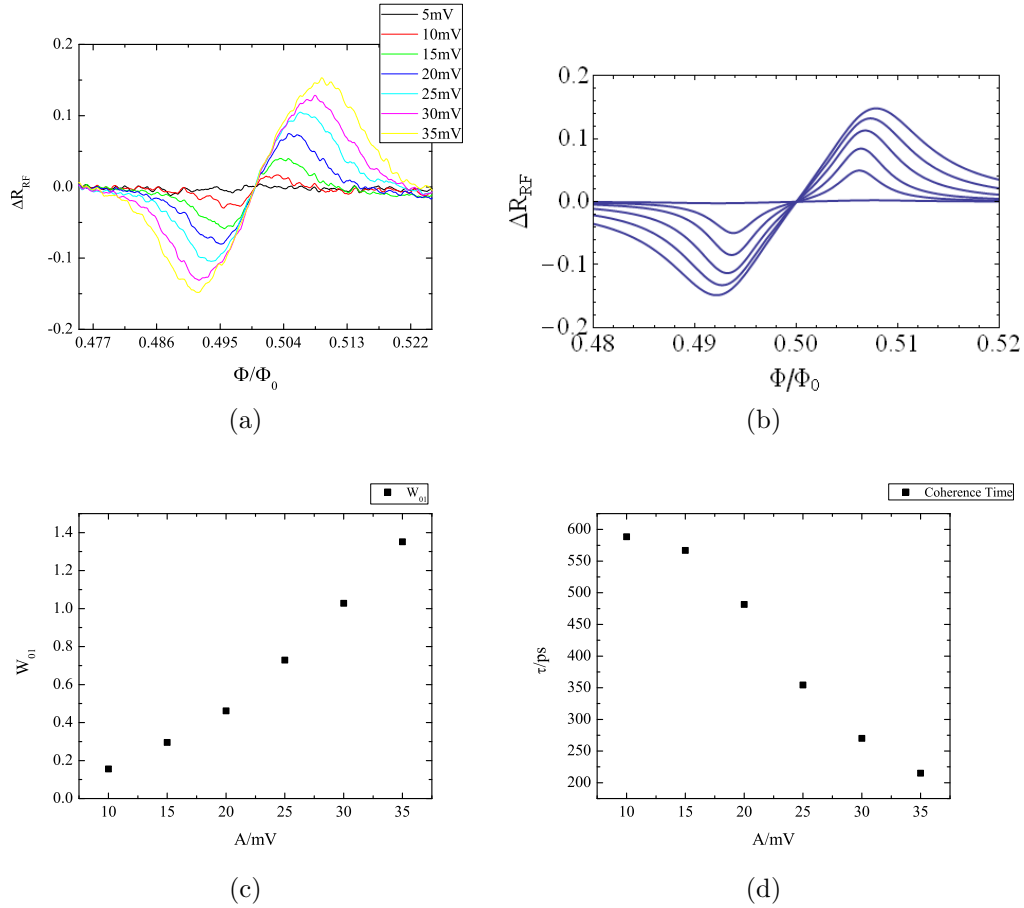
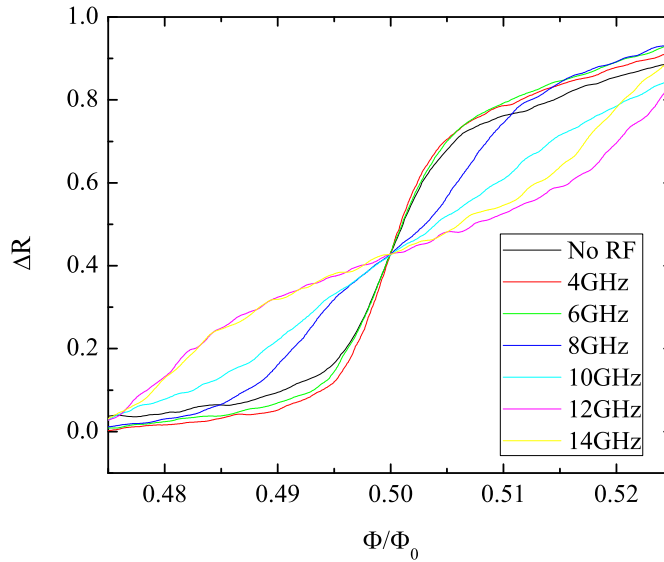
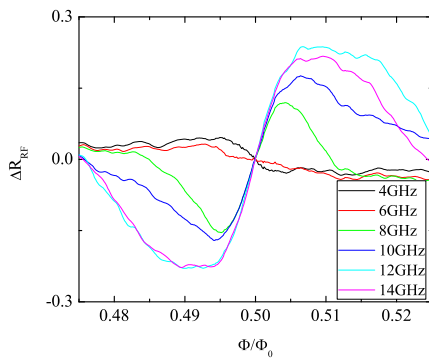


Figure 9.12: The above graphs show the data obtained by fitting the experimental data to the model described in chapter 5. (a) The experimental data and the computer simulation which were generated from it using the model described in 5.1. The fitting parameters were the decoherence rate  $\Gamma$  and the coupling  $W_{01}$ . (b) The decoherence times generated by this fitting process plotted as a function of RF amplitude. (c) The coupling parameter plotted as a function of RF amplitude.

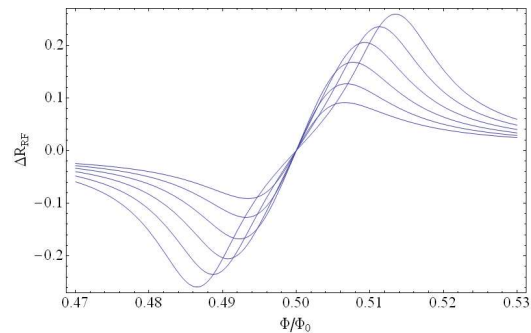
There is some discrepancy between the shape of resonances observed and those predicted by our model. This may be due to some of the assumptions that have been made in order to simplify the model. In the model we have assumed a constant decoherence rate independent of the RF frequency. In reality the coherence rate will depend on the flux bias of the system. We have also assumed that the RF amplitude is independent of the RF frequency. In practice resonances in the RF line means this is not the case.



(a)



(b)



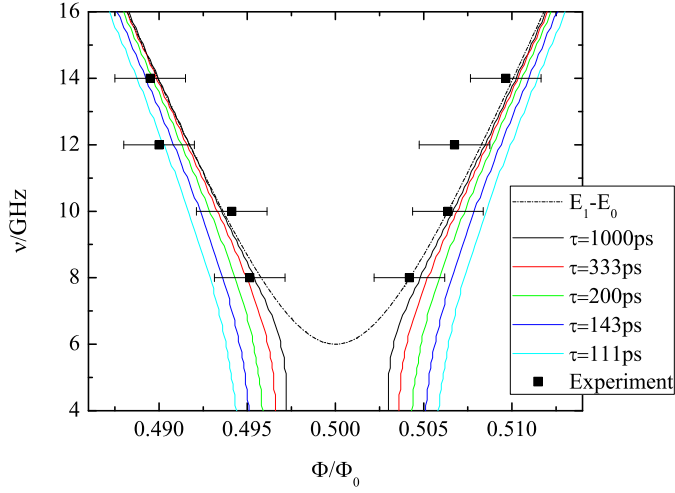
(c)

Shows the resistance of the inteferometer plotted as a function of magnetic flux at RF field frequencies between 4GHz and 14GHz. (b) Shows the resistance at a function flux at RF frequencies between 4GHz and 14GHz, subtracted from that taken at 0mV, giving the change in resistance due to RF field. (c) Shows the computer simulation of data shown in (b) based on the model described in 5.1

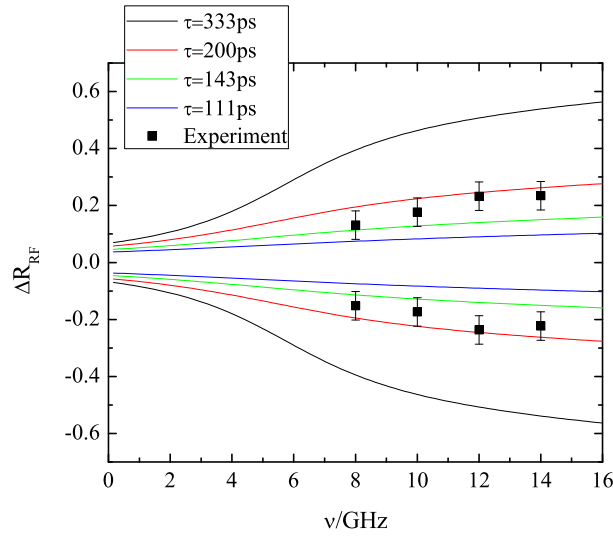
Figure 9.13: (a)

Shows the resistance of the inteferometer plotted as a function of magnetic flux at RF field frequencies between 4GHz and 14GHz. (b) Shows the resistance at a function flux at RF frequencies between 4GHz and 14GHz, subtracted from that taken at 0mV, giving the change in resistance due to RF field. (c) Shows the computer simulation of data shown in (b) based on the model described in 5.1





(a)



(b)

Figure 9.14: The above graphs show the behaviour of the resonance peaks seen in Figure 9.10. (a) Shows the position of the peak. The dashed line shows the energy spectrum ( $E_1 - E_0$ ) described by equation 5.2. The fitting parameters where  $\Delta = 3\text{GHz}$  and  $E_j/E_C = 200$ . The solid lines show the model behaviour of resonant peak position with coherence times between 111ps and 1000ps, as described in chapter 5. (b) Shows the amplitude of the peak as a function of RF frequency. The solid lines show the model behaviour of resonant peak amplitude with coherence times between 111ps and 333ps.

## 9.5 Andreev Interferometer's response to a strong RF field

We wished to investigate the influence of a strong RF field on an Andreev interferometer alone. To do this we used a different sample, which consisted of a silver cross connected to a plain loop of aluminium, as shown in Figure 9.15. As expected, the resistance of the cross oscillated as a function of the magnetic flux through the loop. When a strong RF field was applied the amplitude of the oscillations decreased with increasing RF amplitude, until at high RF amplitudes a  $\pi$  shift in the oscillations was observed, as shown in Figure 9.16.

This phenomenon is thought to be a consequence of the RF field adding a high frequency oscillating component to the flux threading the aluminium loop. This leads to a high frequency component of the phase so that the time dependant phase can be written as

$$\tilde{\phi} = \phi + \mu \sin\left(2\pi \frac{t}{\tau}\right) \quad (9.4)$$

where  $\phi$  is the phase across the interferometer due to the static magnetic field,  $\tau = 1/f$  is the frequency of the RF field,  $\mu$  is the amplitude of the RF field. The change in resistance can then be written as

$$\tilde{R} = R_N - \frac{1}{1 + a\mu^2} (1 + \cos(\tilde{\phi})) \quad (9.5)$$

In this equation  $a$  is a parameter which models the damping of the oscillations due to heating from the RF. This high frequency component is averaged by the measurement system leading to a observed change in resistance equal to

$$\Delta R = \frac{\int_{-\tau/2}^{\tau/2} (1 + \cos(\phi + \mu \sin(2\pi \frac{t}{\tau}))) dt}{(1 + a\mu^2)\tau} \quad (9.6)$$

The integral shown in 9.6 is a Bessel function, and so the measured resistance oscillates as a function of RF amplitude.

We measured the change in resistance as a function of RF amplitudes for a number of different values of  $\phi$ . These experimental results agree qualitatively with the model described above, as shown in Figure 9.17. In order to see this effect the interferometer must be operating in the adiabatic regime, in that the response time of the interferometer must be shorter than the period of the RF oscillations. This allows us to estimate an upper limit for the time of flight of the electrons in the interferometer of  $\tau_f < 50$ ps.

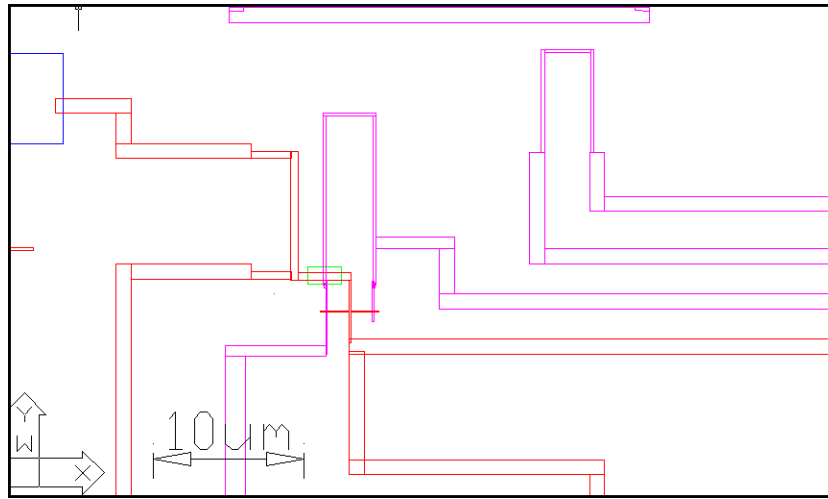


Figure 9.15: This Figure shows a diagram of the sample used to observe a  $\pi$  shift in the Andreev interferometer oscillations. It is the same design as the main sample used in experiment one, but with the qubit replaced with a plain loop of aluminium.

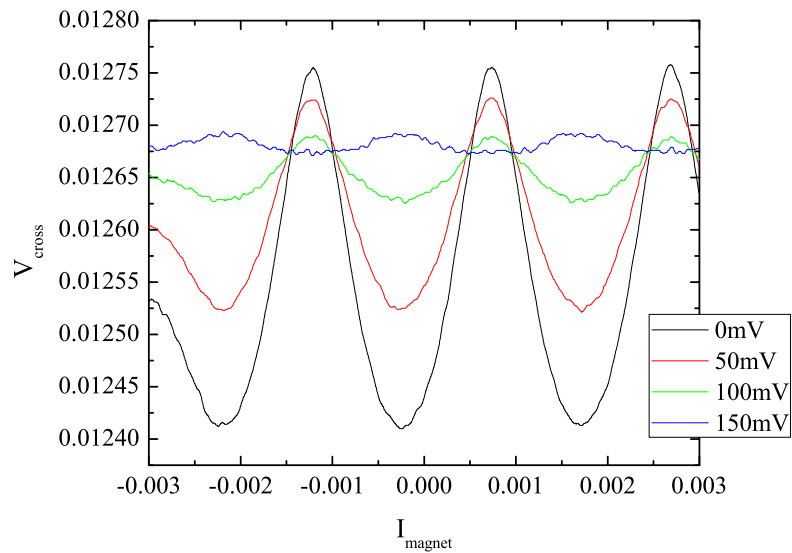
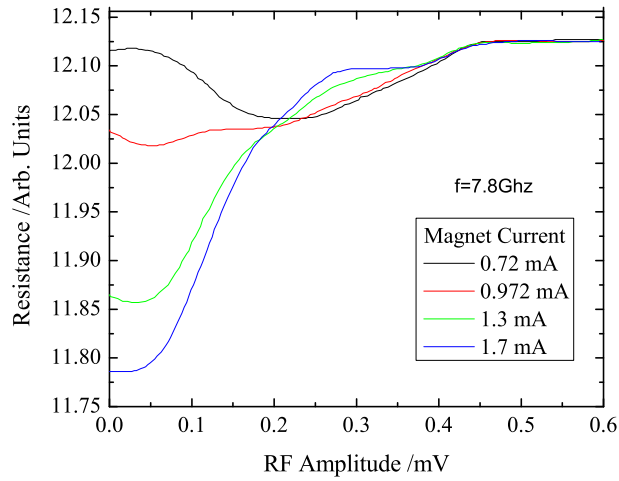
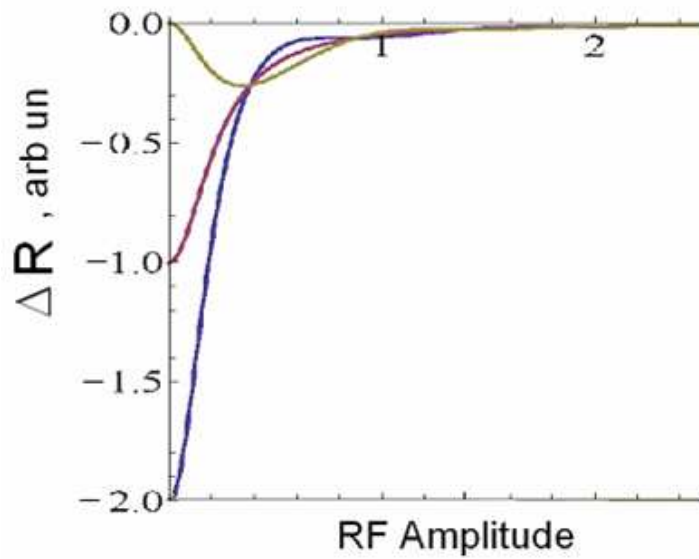


Figure 9.16: Resistance plotted against applied magnetic field for an interferometer under 7.6Ghz RF radiation with increasing power. As power is increased the oscillations amplitude decreases until a  $\pi$  shift is observed.



(a)



(b)

Figure 9.17: (a) Resistance plotted against RF power for a microwave frequency of 7.6GHz, at various applied magnetic fields. The oscillation in resistance can be seen superimposed onto the overall decrease in oscillation amplitude due to the heating of the sample. (b) Plot of the change in resistance as a function of RF amplitude modelled using equation 9.6

## 9.6 Summary and Conclusions

The main achievement of this project is to show that the back action of the Andreev probe on the attached flux qubit is low enough that an energy gap can be observed in the qubit.

This conclusion is based on the following evidence

- We observe a change in the qubit behaviour with temperature and flux that strongly suggests thermal excitation of the qubit into the excited state. Fitting of this data gives an energy gap  $\Delta = 3 \pm 1\text{GHz}$ . This value is in good agreement with those obtained from ground state observations of the qubit and from model calculations.
- The change in behaviour of the qubit under the influence of a RF field was consistent with the qubit undergoing resonant excitation. From this we were able to estimate an energy gap of  $\Delta = 3 \pm 1\text{GHz}$ . This is in good agreement with the observations made of the qubit in the ground state, temperature measurements and model calculations.
- The measurements of the coherence time estimated  $\tau = 150\text{ps}$ . Such a short coherence time can be explained as a consequence of the high dephasing rate caused by the strong coupling of the interferometer to the qubit, and of the high environmental noise.

We observe a  $\pi$  shift in the oscillations at high RF fields. This shift suggests a very short response time of the Andreev of  $10^{-10}\text{s}$ . These measurements at high RF field could be used to study the damping of coherent effects and their dependence on excitation frequency.

We have also developed a novel tri-layer resist system, discussed in chapter 7, that allow for the fabrication of high quality mesoscopic structures. The selective undercut used in this fabrication process allows for the creation of some unique structures and has many applications in other projects.

## 9.7 Future Work

In this project we have presented evidence that it is possible to observe resonant excitation in a flux qubit using an Andreev interferometer. However, the coherence times observed appear to be very short in comparison to those measured by other groups using more established methods. In order to carry out high quality spectroscopy and observe Rabi oscillations, and make the Andreev interferometer a viable alternative to other methods, future work will have to concentrate on increasing the coherence time of the qubit.

In chapter 5 we derived formulas to describe the relaxation and dephasing rates.

$$\Gamma_{ra} = \left( \frac{\Delta/\hbar}{\omega_{res}} \right) \frac{4I_p^2 M^2 I_c q^2}{\Phi_0^2 \hbar \omega_{res}} \cos^2(M_1 \phi_{int}) \frac{1}{\omega^2 C^2 R} \coth \left( \frac{\hbar \omega_{res}}{2k_B T} \right) \quad (9.7)$$

$$\Gamma_{\phi a} = \frac{\Gamma_{ra}}{2} + \left( \frac{\epsilon}{\hbar \omega} \right)^2 \frac{8\pi I_p^2 M^2}{\hbar} \left( \frac{I_{cq}}{I_{ca}} \right)^2 \frac{\cos^2(M_1 \phi_{int})}{\cos^2(M_2 \phi_{int})} \frac{1}{R} \frac{k_B T}{\hbar} \quad (9.8)$$

Considering these equations allow us to conceive of ways to improve the experiment. The following sections present two methods which could be used to increase the coherence time of the system. The first is a simple process of decreasing the coupling between qubit and interferometer to increase the coherence time, at the expense of decreasing the sensitivity of the system. The second method is more ambitious, exploiting the tuneable supercurrent in an Andreev interferometer to create a readout that can be quickly switched between ‘on’ and ‘off’ states.

### 9.7.1 Method 1

Examining 9.7 and 9.8, it is clear that one option for increasing the coherence time of the system would be to decrease  $M$ , the effective inductance between the qubit and interferometer. In the current design,  $M$  is extremely high because the qubit is directly connected to the interferometer. By disconnecting the qubit so that it is coupled inductively to the interferometer, it would be possible to decrease the  $M$  by several orders of magnitude. This would lead to a corresponding increase in the dephasing and relaxation times. This design is shown in Figure 9.18.

This increase in coherence would be at the cost of the sensitivity system. The resistance of the interferometer would be less sensitive to the changes in phase of the qubit. This decreased sensitivity would mean that the signal to noise ratio of readout would have to be higher than present in order to observe resonance peaks.

In summary, this method of increasing the coherence time would be easily achievable and quickly implementable using current fabrication technologies and measurement setup. It would, however lead to a permanent decrease in the sensitivity of the system.

### 9.7.2 Method 2

The second method for increasing the coherence time is more ambitious. It exploits the tenable supercurrent in an Andreev interferometer investigated

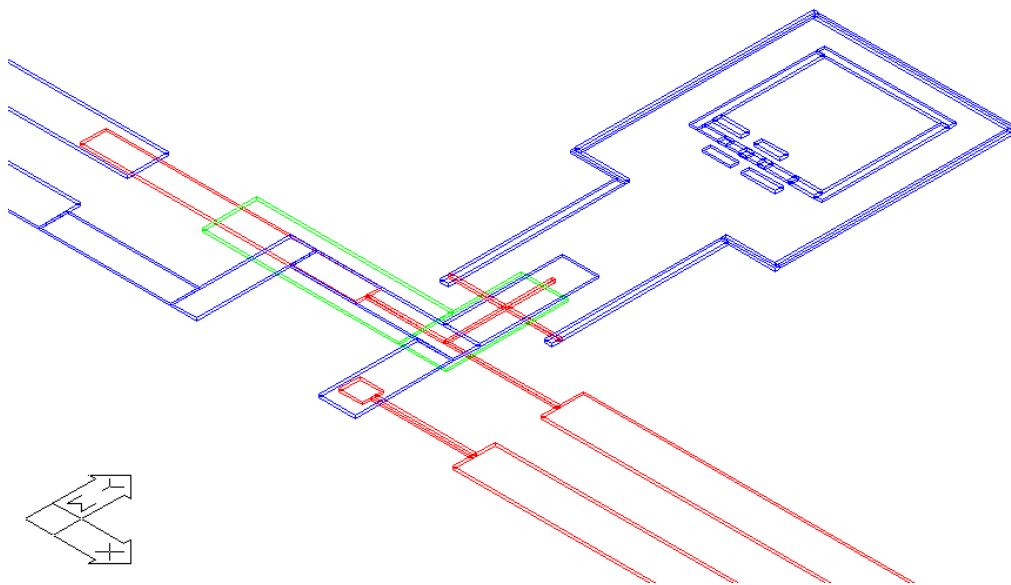


Figure 9.18: A concept drawing for an improved qubit and interferometer. Aluminium is shown in blue and silver in red. A silicon oxide spacer is shown in green. In this design the qubit is no longer directly connected to the interferometer, but is coupled by mutual inductance  $M$ . By fabricating the circuit so that  $M$  is low, the coherence time of the qubit can be increased. This design also includes a new method of fabricating the interferometer. In this method the current into the interferometer is injected by an aluminium wire which lies on top of the silver cross, separated by a silicon oxide spacer. This ensures that the current loop is in a plane perpendicular to plane of the qubit, minimising the flux coupling between the measurement current and the qubit

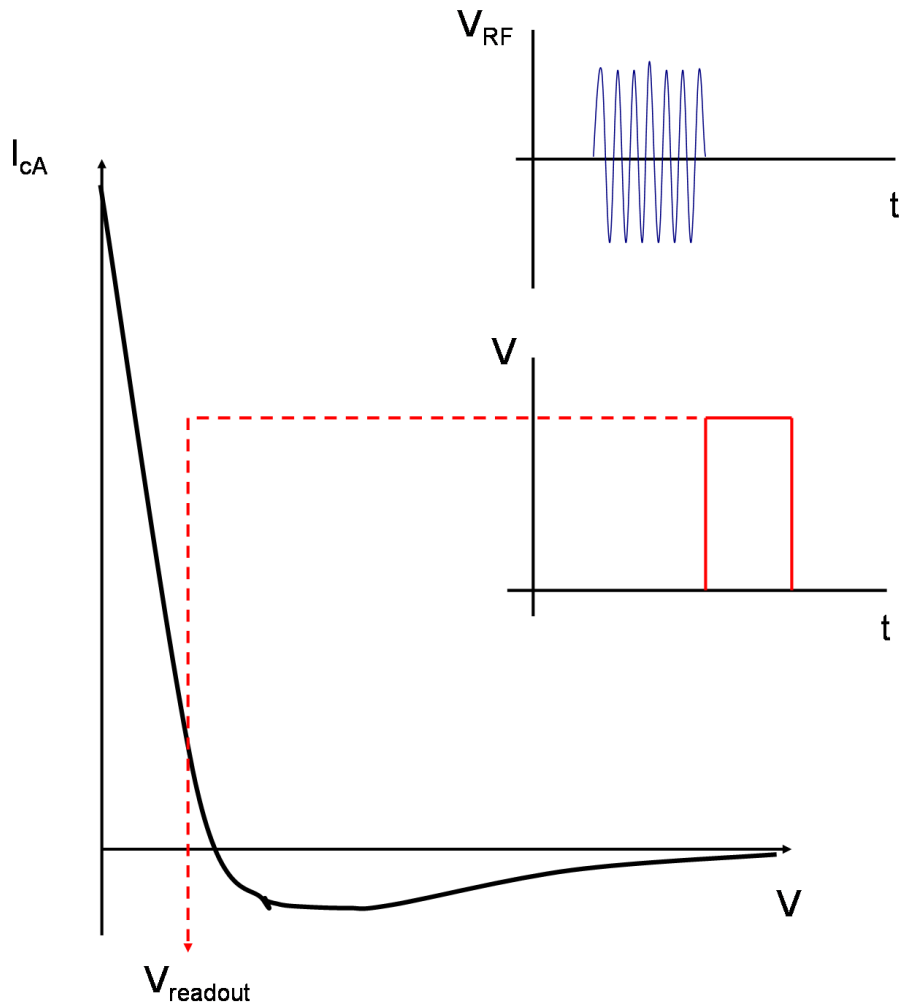


Figure 9.19: The critical current of the interferometer as a function of the control voltage  $V$ . During qubit manipulation the control voltage is zero and the critical current of the interferometer long, leading to long coherence times. When the qubit is probed, the voltage is increased to  $V_{readout}$ , leading to a smaller critical current and a strong coupling of the interferometer to the qubit.



by Morpurgo and others. 9.7 and 9.8 show that the relaxation and dephasing times are related to the ratio of the qubit critical current to the interferometer critical current,  $I_{cq}/I_{ca}$ . Morpurgo showed that the critical current of the interferometer can be controlled by the voltage across the perpendicular section [38], as shown in Figure 9.19. Using this it should be possible to create a readout which can be switched from an off state where there is no voltage, so the critical current is high and the coherence times long, to an on state where there is a voltage allowing the qubit state to be read out.

In this regime the external flux is positioned close to  $\Phi_0/2$  so that the excited state of the qubit becomes accessible. A pulse of RF is then applied so that the qubit resonates between the ground and excited state. The critical current of the Andreev interferometer is high at this time so the coherence time of the qubit is long. Some time after the pulse of RF, a pulse of current is passed through the interferometer. This decreases the critical current, coupling the interferometer to the qubit and allowing it to be read out.

The advantage of this method is that it allows for a flexible readout system that can be kept off to allow long coherence times, while still maintaining the high sensitivity of the Andreev interferometer readout, when it is turned on. This method, however is considerably more complex and would require a large amount of time spent on perfecting the readout method and redesigning the measurement setup to allow for pulsed measurements.

# Bibliography

- [1] Bertet, P., Chiorescu, I., Burkard, G., Semba, K., Harmans, C. J. P. M., DiVincenzo, D. P., and Mooij, J. E. *arXiv:cond-mat* (2004).
- [2] Il'ichev, E., Oukhanski, N., Izmalkov, A., Wagner, T., Grajcar, M., Meyer, H.-G., Smirnov, A. Y., Maassen van den Brink, A., Amin, M. H. S., and Zagoskin, A. M. *Phys. Rev. Lett.* **91**, 097906 Aug (2003).
- [3] Marshall, K. M. *An Andreev Probe of Superconducting Quantum Circuits*. PhD thesis, Royal Holloway College, University of London, (2007).
- [4] Chua, K. G. *Andreev Interferometry with Superconducting Persistent Current Qubits*. PhD thesis, Royal Holloway College, University of London, (2005).
- [5] Petrashov, V. T., Chua, K. G., Marshall, K. M., Shaikhaidarov, R. S., and Nicholls, J. T. *Physical Review Letters* **95**(14), 147001 (2005).
- [6] Feynman, R. *International Journal of Theoretical Physics* **21**(6&7), 467–488 (1982).
- [7] Shor, P. W. In *Proceedings of the 35th Annual Symposium on Foundations of Computer Science*, 124–134. Institute of Electrical and Electronic Engineers Computer Society Press, (1994).
- [8] DiVincenzo, D. F. *Fortschritte der Physik* **28771** (2000).
- [9] Cory, D. et al. *Fortschritte der Physik* **48**(9-11), 875–907 (2000).
- [10] Gershenfeld, N. A. and Chuang, I. L. *Science* **275**(5298), 350–356 (1997).
- [11] Cirac, J. I. and Zoller, P. *Phys. Rev. Lett.* **74**(20), 4091–4094 May (1995).

- [12] Monroe, C., Meekhof, D. M., King, B. E., Itano, W. M., and Wineland, D. J. *Phys. Rev. Lett.* **75**(25), 4714–4717 Dec (1995).
- [13] Pachos, J. and Walther, H. *Phys. Rev. Lett.* **89**(18), 187903 Oct (2002).
- [14] Kok, P., Munro, W. J., Nemoto, K., Ralph, T. C., Dowling, J. P., and Milburn, G. J. *Reviews of Modern Physics* **79**(1), 135 (2007).
- [15] Hughes, R. et al. *Advanced Research and Development Activity* (2004).
- [16] Orlando, T. *Physica C* **372-376**(194-200), 194–200 (2002).
- [17] Chiorescu, I., Nakamura, Y., Harmans, C. J. P. M., and Mooij, J. E. *Science* **299**(5614), 1869–1871 (2003).
- [18] Grajcar, M., Izmalkov, A., van der Ploeg, S. H. W., Linzen, S., Il'ichev, E., Wagner, T., Hubner, U., Meyer, H.-G., van den Brink, A. M., Uchaikin, S., and Zagoskin, A. M. *Physical Review B (Condensed Matter and Materials Physics)* **72**(2), 020503 (2005).
- [19] Likharev, K. K. *Dynamics of Josephson Junctions and Circuits*. Gordon and Breach Science Publishers, (1986).
- [20] Schn, G. and Zaikin, A. D. *Physics Reports* **198**(5-6), 237 – 412 (1990).
- [21] Rose-Innes, A. and Rhoderick, E. *Introduction to Superconductivity*. Pergamon Press, (1978).
- [22] Devoret, M. H., Martinis, J. M., Esteve, D., and Clarke, J. *Phys. Rev. Lett.* **53**(13), 1260–1263 Sep (1984).
- [23] Voss, R. F. and Webb, R. A. *Phys. Rev. Lett.* **47**(4), 265–268 Jul (1981).
- [24] Devoret, M. H., Martinis, J. M., and Clarke, J. *Phys. Rev. Lett.* **55**(18), 1908–1911 Oct (1985).
- [25] Majer, J. *Superconducting Quantum Circuits*. PhD thesis, Technische Universiteit Delft, (202).
- [26] Makhlin, Y., Schön, G., and Shnirman, A. *Rev. Mod. Phys.* **73**(2), 357–400 May (2001).
- [27] Pashkin, Y. A., Astafiev, O., Yamamoto, T., Nakamura, Y., and Tsai, J. S. *Quantum Information Processing* **8**(2-3), 55–80 Jun (2009).

- [28] Friedman, J., Patel, V., Chen, W., Tolpygo, S., and Lukens, J. *NATURE* **406**(6791), 43–46 JUL 6 (2000).
- [29] Orlando, T. P., Mooij, J. E., Tian, L., van der Wal, C. H., Levitov, L. S., Lloyd, S., and Mazo, J. J. *Phys. Rev. B* **60**(22), 15398–15413 Dec (1999).
- [30] Mooij, J. E., Orlando, T. P., Levitov, L., Tian, L., van der Wal, C. H., and Lloyd, S. *Science* **285**(5430), 1036–1039 (1999).
- [31] Leggett, A. J., Chakravarty, S., Dorsey, A. T., Fisher, M. P. A., Garg, A., and Zwerger, W. *Rev. Mod. Phys.* **59**(1), 1–85 Jan (1987).
- [32] Cohen-Tannoudji, C. *Quantum Mechanics Vol. 1*. Wiley, (1977).
- [33] Lisenfeld, J. *Experiments on Superconducting Josephson Phase Quantum Bits*. PhD thesis, Universitat Erlangen-Nurnberg, (2007).
- [34] Annett, J. F. *Superconductivity, Superfluids and Condensates*. Oxford University Press, (2004).
- [35] De Gennes, P. G. *Rev. Mod. Phys.* **36**(1), 225–237 Jan (1964).
- [36] Courtois, H., Gandit, P., Mailly, D., and Pannetier, B. *Phys. Rev. Lett.* **76**(1), 130–133 Jan (1996).
- [37] Morpurgo, A. F., Klapwijk, T. M., and van Wees, B. J. *Applied Physics Letters* **72**(8), 966–968 (1998).
- [38] Baselmans, J., Morpurgo, A., van Wees, B., and Klapwijk, T. *NATURE* **397**(6714), 43–45 JAN 7 (1999).
- [39] Andreev, A. F. *Sov. Phys. JETP* **19**, 1228 (1964).
- [40] Guéron, S., Pothier, H., Birge, N. O., Esteve, D., and Devoret, M. H. *Phys. Rev. Lett.* **77**(14), 3025–3028 Sep (1996).
- [41] Ostrovsky, P. M., Skvortsov, M. A., and Feigel'man, M. V. *Phys. Rev. Lett.* **87**(2), 027002 Jun (2001).
- [42] Petrashov, V. T., Antonov, V. N., Delsing, P., and Claeson, R. *Phys. Rev. Lett.* **70**(3), 347–350 Jan (1993).
- [43] Petrashov, V., Antonov, V., Delsing, P., and Claeson, R. *JETP Letters* **60**(8), 606–611 OCT 25 (1994).

- [44] De Vegvar, P. G. N., Fulton, T. A., Mallison, W. H., and Miller, R. E. *Phys. Rev. Lett.* **73**(10), 1416–1419 Sep (1994).
- [45] Petrashov, V. T., Antonov, V. N., Delsing, P., and Claeson, T. *Phys. Rev. Lett.* **74**(26), 5268–5271 Jun (1995).
- [46] Nazarov, Y. V. and Stoof, T. H. *Phys. Rev. Lett.* **76**(5), 823–826 Jan (1996).
- [47] Petrashov, V., Shaikhaidarov, R., and Sosnin, I. *JETP LETTERS* **64**(11), 839–844 DEC 10 (1996).
- [48] Volkov, A. F. and Takayanagi, H. *Phys. Rev. B* **56**(17), 11184–11194 Nov (1997).
- [49] Bertet, P., Chiorescu, I., Burkard, G., Semba, K., Harmans, C. J. P. M., DiVincenzo, D. P., and Mooij, J. E. *Physical Review Letters* **95**(25), 257002 (2005).
- [50] Majer, J. B., Paauw, F. G., ter Haar, A. C. J., Harmans, C. J. P. M., and Mooij, J. E. *Phys. Rev. Lett.* **94**(9), 090501 Mar (2005).
- [51] Plantenberg, J. H., de Groot, P. C., Harmans, C. J. P. M., and Mooij, J. E. *NATURE* **447**(7146), 836–839 JUN 14 (2007).
- [52] Il'ichev, E., Wagner, T., Fritzsche, L., Kunert, J., Schultze, V., May, T., Hoenig, H. E., Meyer, H. G., Grajcar, M., Born, D., Krech, W., Fistul, M. V., and Zagoskin, A. M. *Applied Physics Letters* **80**(22), 4184–4186 (2002).
- [53] Shevchenko, S. N., van der Ploeg, S. H. W., Grajcar, M., Il'ichev, E., Omelyanchouk, A. N., and Meyer, H. G. *Physical Review B* **78**(17) NOV (2008).
- [54] Lupaşcu, A., Verwijs, C. J. M., Schouten, R. N., Harmans, C. J. P. M., and Mooij, J. E. *Phys. Rev. Lett.* **93**(17), 177006 Oct (2004).
- [55] Lupaşcu, A., Driessen, E. F. C., Roschier, L., Harmans, C. J. P. M., and Mooij, J. E. *Physical Review Letters* **96**(12), 127003 (2006).
- [56] Lee, J. C., Oliver, W. D., Berggren, K. K., and Orlando, T. P. *Physical Review B (Condensed Matter and Materials Physics)* **75**(14), 144505 (2007).

- [57] Lupascu, A., Saito, S., Picot, T., De Groot, P. C., Harmans, C. J. P. M., and Mooij, J. E. *Nature Physics* **3**(2), 119–123 Feb (2007).
- [58] Inomata, K., Watanabe, M., Yamamoto, T., Matsuba, K., Nakamura, Y., and Tsai, J. S. *Journal of Physics: Conference Series* **150**(5), 052077 (4pp) (2009).
- [59] Burkard, L. *Advances in Physics* **57**, 225–285 (2008).
- [60] Kenyon, M., Lobb, C. J., and Wellstood, F. C. *Journal of Applied Physics* **88**(11), 6536–6540 (2000).
- [61] Van Harlingen, D. J., Robertson, T. L., Plourde, B. L. T., Reichardt, P. A., Crane, T. A., and Clarke, J. *Phys. Rev. B* **70**(6), 064517 Aug (2004).
- [62] Simmonds, R. W., Lang, K. M., Hite, D. A., Nam, S., Pappas, D. P., and Martinis, J. M. *Phys. Rev. Lett.* **93**(7), 077003 Aug (2004).
- [63] Grifoni, M., Paladino, E., and Weiss, U. *The European Physical Journal B* **10**(4), 719–729 (1999).
- [64] van der Wal, C. H. *Quantum Superpositions of Persistent Josephson Currents*. PhD thesis, Delft University of Technology, (2001).
- [65] Carlick, A. J. *A Controllable Pi-Junction in a Mesoscopic Superconducting System*. PhD thesis, University of Bristol, (2005).
- [66] Kyser, D. F. and Viswanathan, N. S. *J. Vac. Sci. Technol.* **12**(6), 1305–1308 (1975).
- [67] Burkard, G., DiVincenzo, D. P., Bertet, P., Chiorescu, I., and Mooij, J. E. *Physical Review B* **71**, 134504 (2005).
- [68] Henning, T. *Charging effects in niobium nanostructures*. PhD thesis, (1999).
- [69] Bladh, K., Gunnarsson, D., Hurfeld, E., Devi, S., Kristoffersson, C., Smalander, B., Pehrson, S., Claeson, T., Delsing, P., and Taslakov, M. *Review of Scientific Instruments* **74**(3), 1323–1327 (2003).
- [70] Spietz, L., Teufel, J., and Schoelkopf, R. J. (2006).